Dissertation
submitted to the
Combined Faculty of Mathematics, Engineering and
Natural Sciences
of Heidelberg University, Germany
for the degree of
Doctor of Natural Sciences

Put forward by

M.Sc. Aigars Znotins
born in Riga

Oral examination: 7st February 2024

Electron recombination of rotationally cold deuterated triatomic hydrogen ions at the Cryogenic Storage Ring

Referees:

PD Dr. Holger Kreckel
PD Dr. Zoltán Harman

Elektronenrekombinationsexperimente mit rotationsgekühlten, deuterierten dreiatomigen Wasserstoff–Molekülionen im kryogenen Speicherring CSR

Die vorliegende Arbeit zielt auf das Verständnis der Dissoziativen Rekombination von Elektronen mit deuterierten Isotopologen des dreiatomigen Wasserstoff-Kations H_2D^+ und D_2H^+ im kryogenen Speicherring CSR am Max-Planck-Institut für Kernphysik ab. Innerhalb des CSR wurden Elektronen– und Ionenstrahlen überlagert und somit Kollisionsexperimente zwischen Ionen und Elektronen untersucht.
Die Molekülionen wurden bis zu $1000\,s$ im CSR Strahlungsfeld bei Temperaturen $T < 10\,K$ gespeichert. In dieser Zeit kühlen gespeicherte Ionenstrahlen in ihren inneren Freiheitsgraden, so dass nur eine geringe Anzahl bekannter Rotationszustände verblieb. In dieser Arbeit wird ein Modell zur radiativen Kühlung der inneren Freiheitsgrade mithilfe von umfassenden Daten zu molekularen Energieniveaus erstellt. Darüber hinaus beschreibt das Modell Kühleffekte über inelastische Stöße mit Elektronen und durch selektive Entvölkerung von Zuständen durch Elektronenrekombination.
Der experimentelle Teil dieser Arbeit widmet sich der Untersuchung von Dissoziativer Rekombination von rotationsgekühlten H_2D^+ und D_2H^+ Ionen im Bereich relativer Kollisionsenergien von ≈ 0–$14\,eV$. Die Ergebnisse werden mit aktuellen theoretischen Berechnungen von rotationsabhängigen Wirkungsquerschnitten verglichen. Aus den experimentellen Ratenkoeffizienten der Reaktion werden Plasmaratenkoeffizienten berechnet und mit Schätzwerten verglichen, die in der Literatur für die Modellierung chemischer Reaktionen in interstellaren Molekülwolken verwendet wurden.

Electron recombination of rotationally cold deuterated triatomic hydrogen ions at the Cryogenic Storage Ring

The work presented in this dissertation describes the ongoing efforts aimed towards understanding the Dissociative Recombination by electrons of the deuterated isotopologues of the triatomic hydrogen cation – H_2D^+ and D_2H^+ – inside the Cryogenic Storage Ring (CSR), located at the Max Planck Institute for Nuclear Physics. The facility is equipped with a merged electron–ion beams setup, that permits the investigation of ion–electron collisions.
The molecular ions were stored for up to $1000\,s$ in the CSR environment at temperatures $T < 10\,K$. At such timescales, the rovibrational populations of the stored ion beams become confined to a small number of identifiable states, according to a radiative cooling model based on comprehensive line–lists. The thesis describes the construction of such radiative cooling models, which in addition to

radiative relaxation include the effects of inelastic electron collisions and selective depletion by electron recombination.
The experimental part of the present work consists of investigating the Dissociative Recombination reaction of rotationally cold H_2D^+ and D_2H^+ ions in the relative collision energy range of ≈ 0–$14\,eV$. Comparisons between experimental results and state-of-the-art theoretical calculations of the rotational state–specific cross sections are presented. The experimental rate coefficients are converted to plasma rate coefficients and compared against prior estimates that have been used in modelling of interstellar cloud chemistry.

Contents

List of Figures

List of Tables

Chapter 1

Introduction

The triatomic hydrogen ion H_3^+ was first identified by J. J. Thomson in 1911, during his research endeavors on "positive electricity" (Thomson 1911). Throughout the following decades, this molecule has been a target of extensive laboratory and theory studies unveiling various questions on the subject of astrophysics. This chapter provides an overview on the history of triatomic hydrogen and its role in astronomy with the purpose of establishing this dissertation within a broader perspective.

H_3^+ consists of three protons and two electrons, making it the simplest polyatomic molecular ion possible. After the initial evidence of a mass three signature in Thomson's experiments employing a hydrogen discharge, a quest to explain the production and molecular structure of such a system was initiated. First efforts of explaining the stability of triatomic hydrogen are credited to Bohr 1919, where he proposed an equidistant geometrical configuration of the subatomic constituents. In the paper (Bohr 1919), Bohr came to the conclusion that neutral H_3 should be stable, while deeming H_3^+ unstable. At that time such a description was regarded as a fundamental reconstruction of the contemporary Rutherford atom conceptions. Consequently, in 1935 Coulson (Coulson 1935) performed calculations based on molecular orbital theory that suggested an equilateral triangular shape of the H_3^+ molecule. However, it took until the 60s to firmly establish this view, when more powerful numerical computer calculation methods had become available (Christoffersen, Hagstrom, and Prosser 1964). Experimental confirmation of the triangular shape of H_3^+ was first demonstrated in (Gaillard, M. J. et al. 1978) by means of Coloumb explosion imaging.

During the 70s Carney and Porter published an ab initio potential energy sur-

face of H_3^+ (Carney and Porter 1974) followed by calculations of a rovibrational spectrum (Carney and Porter 1976, 1980). This development was instrumental for guiding the first laboratory spectroscopy measurements of H_3^+ performed by Oka (Oka 1980).

The first statement regarding the relevance of H_3^+ in astronomy can be found in the work of Martin, McDaniel, and Meeks 1961, emphasizing the efficiency of the reaction process:

$$H_2^+ + H_2 \rightarrow H_3^+ + H + 1.76\,eV. \tag{1.1}$$

This implies that H_3^+ is the dominant ion in certain cold hydrogen plasmas, such as the interstellar medium (ISM). Subsequently, models of interstellar cloud chemistry (Watson 1973, Herbst and Klemperer 1973) identified H_3^+ as one of the main drivers in an ion–neutral chemistry network, facilitating formation of larger molecules. Figure 1.1 illustrates an excerpt of this reaction network, signifying the importance of H_3^+.

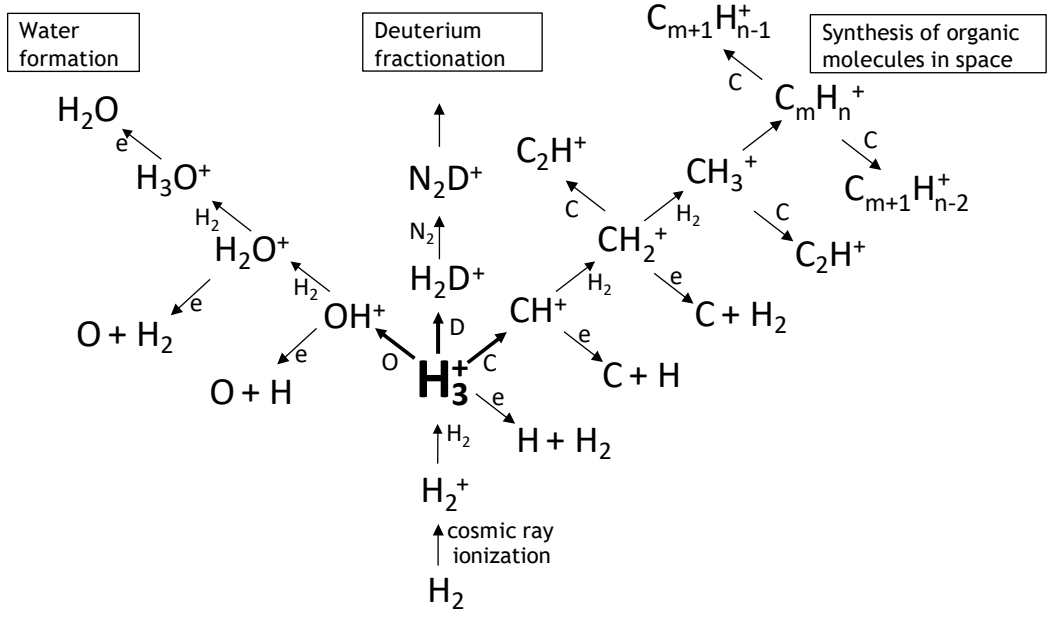

Figure 1.1: The role of the triatomic hydrogen ion in ion–neutral reactions that drive interstellar chemistry at low temperatures and densities. Figure adapted from McCall 2001.

After the initial detection of the infrared absorption spectrum in a laboratory setting, the search for interstellar H_3^+ was triggered. However, rotational

spectroscopy is inaccessible, as the symmetrical shape of the molecule is responsible for the absence of a permanent dipole moment. Furthermore, as no stable electronically excited states of H_3^+ are known, spectroscopy has to rely on vibrational transitions. Despite these limitations, the presence of H_3^+ was eventually confirmed in dense interstellar clouds by its absorption spectra in the infrared (Geballe and Oka 1996). Surprisingly, prior to the initial interstellar observation, H_3^+ was detected in Jupiter's atmosphere (Drossart et al. 1989) by emission lines in the 2 μm region. While initally unexpected, the discovery later became an important probe for monitoring conditions of planetary systems. Since then H_3^+ has been found in various environments, including diffuse interstellar clouds (McCall et al. 1998), planetary atmospheres (Geballe, Jagod, and Oka 1993 and Trafton et al. 1993), even in clouds close to the galactic center (Oka et al. 2019). For a comprehensive review of H_3^+ astronomy the reader is referred to (Miller et al. 2020).

Deuterium fractionation is yet another topic that warrants a mention of triatomic hydrogen and its isotopologues in the context of astrochemistry. The relative abundance of deuterium with respect to hydrogen in interstellar clouds is approximately $D/H = 1.5 \cdot 10^{-5}$, although this ratio exhibits significant variance throughout the Milky Way galaxy (Vastel, Phillips, and Yoshida 2004). In general, the dissimilar ground state energies among hydrogen containing molecules and deuterated ones lead to exothermic reactions, which are unlikely to occur in reverse under thermalized interstellar conditions of 10–50 K (Gerlich, Herbst, and Roueff 2002). As a consequence, the enhanced deuteration gets imbedded during the production of more complex molecules by protonation reactions (Millar, Bennett, and Herbst 1989). On the other hand, a decreased D/H ratio with respect to the primeval conditions indicates a region of stellar activity due to the lower temperature requirements of deuterium fusion compared to hydrogen, which leads to a depleted deuterium reservoir. Thus, deuterium fractionation can serve as a probe for determining the age of interstellar clouds (Brünken et al. 2014).

The destruction of triatomic ions in interstellar environments proceeds either via the aforementioned ion–neutral reactions or in a dissociative recombination (DR) process with free electrons:

$$H_3^+ \rightarrow \begin{array}{c} H + H + H \\ H_2 + H, \end{array} \tag{1.2}$$

where the molecule fragments in neutral atomic and molecular components. Note, that the present introduction pertaining to the significance of DR will be limited to the non–deuterated variant, however, the same main arguments also hold true

for the DR relevance of the isotopologues. A more detailed overview of the specific cases of dissociative recombination of H_2D^+ and D_2H^+ shall follow in the subsequent chapters. In brief, two examples of where destruction of $H_3{}^+$ plays an important role will be given.

In dense interstellar clouds the removal of $H_3{}^+$ is driven by DR with free electrons and ion–neutral reactions. Due to a larger fractional abundance of neutrals (in the gas phase) than free electrons (Herbst 2000), the latter process is considerably more dominant than the former, exemplified by the most prominent reaction:

$$H_3{}^+ + CO \rightarrow HCO^+ + H_2. \tag{1.3}$$

As the creation of $H_3{}^+$ is constricted by the availability of $H_2{}^+$, which in turn is dependant on the cosmic ray ionization rate ζ, one can relate the abundances n and reaction rates k of the involved processes assuming equilibrium conditions as:

$$\zeta n(H_2) \approx k_{CO} n(CO) n(H_3{}^+) k_{DR} n(e), \tag{1.4}$$

thus, emphasizing the role of triatomic hydrogen. In this particular example the contribution of dissociative recombination of $H_3{}^+$ does not assume a central role, however this changes when considering diffuse interstellar cloud environments.

Diffuse clouds feature a higher fractional ionization with respect to dense clouds owing to an increased metallicity (abundance of elements heavier than helium). Such conditions arise as a result of an increased influx of high energy particles with respect to the more opaque dense clouds, which leads to the ionization of the neutral medium and an increased abundance of free electrons (Black 2000). Consequently, in equilibrium, the abundance of $H_3{}^+$ and free electrons that destroy it is linked to the production reaction by:

$$\zeta n(H_2) \approx k_{DR} n(H_3{}^+) n(e), \tag{1.5}$$

further highlighting the role of DR in understanding the cosmic ray ionization rate ζ. In fact, measurements results of DR of $H_3{}^+$ have been directly used for derivation of the cosmic ray ionization rate, the various attempts are summarized in a review by (Oka et al. 2019).

Due to the central role of $H_3{}^+$ as a universal protonator in interstellar chemistry reactions, the dissociation mechanisms of this molecule have been intensively investigated. In most plasmas the destruction of $H_3{}^+$ is predominantly governed by dissociative recombination with free electrons. The rate coefficient of this process has historically been a controversial subject, involving many experiments that produced results differing by several orders of magnitude. A major contributor of

such a large discrepancy is believed to arise from the internal excitations of the molecule. To eliminate unwanted influence on the DR reaction, molecules must be characterized by a well–defined internal energy distribution, ideally enabling state specific recombination measurements. One way this can be achieved is by cooling the target system to the lowest rovibrational levels by means of electron cooling or, if the molecules possesses a dipole moment, radiative relaxation.

The advent of ion storage rings has paved the road for increasingly intricate atomic and molecular physics studies. Among the first heavy–ion storage rings to be developed was the Test Storage Ring (TSR) located at the Max Planck institute for Nuclear physics (MPIK) in Heidelberg (Baumann et al. 1988). Although the TSR was initially designed for research with charged atomic systems, first experiments on molecular physics were already realized in the early nineties (Forck et al. 1993). The inclusion of a low energy electron cooler allowed for experiments on recombination and detachment processes with a degree of precision over the collisional energy on the order of a few mili–electronvolts. Various atomic and molecular systems have been investigated during the operational life–span of the TSR, including a series of measurement campaigns on H_3^+. A few TSR studies in particular stand out in the context of the history of H_3^+ (Kreckel et al. 2005; Kreckel et al. 2010), where the measured DR rate coefficient between H_3^+ and free electrons was found to be in good agreement with previous experiments performed at the CRYRING ion storage ring in Stockholm (McCall et al. 2004). This milestone is considered to finally settle the debate of the reaction rate on the absolute scale.

Almost all prior published work on DR of triatomic hydrogen ions have been performed in room temperature storage rings. It has been showed that vibrationally cold H_3^+ ions can be obtained by radiative relaxation alone after approximately two seconds of storage (Kreckel et al. 2002), therefore the inital temperature of the produced ions is irrelevant, at least in terms of the remaining vibrational excitation. However, H_3^+ features metastable rotational states with lifetimes exceeding time scales of weeks and months. Therefore, due to unresolved questions regarding the stored ion temperature (Kreckel et al. 2010, Petrignani et al. 2011) and by extent the degree of influence of rotational excitation on the measured DR rates, the ultimate challenge – state specific dissociation measurements of H_3^+ – has not been achieved to date. More details regarding the role of the internal exciation of ions during DR measurements are given in sections 2.6 and 3.1.

In recent decades, the storage ring community has moved from magnetic storage devices to electrostatic ones, with one of the advantages being mass–independent storage of ions at a given kinetic energy. Furthermore, a few of the electrostatic

storage rings have been designed to achieve cryogenic temperatures of around $\sim 10\,K$, enabling storage of rovibrationally cold ions in an effectively collision–free environment. Three prime examples of such cryogenic electrostatic devices are DESIREE in Sweden (Thomas et al. 2011), RICE in Japan (Nakano et al. 2017), and CSR in Germany (von Hahn et al. 2016). The Cryogenic Storage Ring (CSR) is equipped with an electron cooler, thus experiments probing electron–ion interactions are possible. Recent examples showcasing the capabilities of CSR on the subject of ion–electron collisions for astrophysically relevant diatomic systems can be found here (CH^+: Paul 2021, OH^+: Kálosi et al. 2021, HeH^+: Novotný et al. 2019). The case of HeH^+ is particularly notable, as the obtained state–specific electron recombination rate coefficients suggest an enhanced abundance of HeH^+ in the early universe.

The research in this dissertation is dedicated towards extending the state-selective DR measurements from diatomic molecules to the simplest polyatomic molecule, the triatomic hydrogen ion, while retaining the same quality of control over the internal excitations as demonstrated for diatomic systems. This work describes DR measurements of rovibrationally cold H_2D^+ and D_2H^+ ions carried out at the CSR. The ions were stored up to $1000\,s$ in a cryogenic environment with temperatures of $T < 10\,K$, leaving only three rovibrational levels significantly populated in the case of H_2D^+ and seven for D_2H^+. Additionally, the storage time dependence of the observed DR rates permits the possibility to discern the contribution of individual rotational states on the overall reaction rate.

The preceding brief introduction shall be followed by an overview of the theoretical background of $H_3{}^+$ and its isotopologues, with the emphasis on the dissociative recombination process. The chapter concludes with open questions regarding the subject and evaluates to what degree said questions can be addressed in the present work. Chapter 3 outlines simulation efforts of H_2D^+ and D_2H^+ internal state evolution during storage in the CSR and provides an estimate of the expected population distribution of the molecular ensemble during the DR experiment. Chapter 4 examines the details of the experimental setup and measurement procedure employed in present work, followed by Chapter 5, in which the measurement results are discussed and a comparison to prior work is given. The thesis concludes with an outlook, reflecting on the outcome and describing the future prospects.

Chapter 2

Theoretical background of the triatomic hydrogen cation

The purpose of the following chapter is to establish the main properties of the investigated molecular systems in question. An overview of basic parameters that describe the characteristics of the molecules shall be given followed by a brief summary of theoretical approaches, derived from first principles, that aim to explain the molecular structure. Subsequently, the various possible interaction processes between molecular ions and electrons will be discussed with particular emphasis on dissociative recombination and its astrophysical significance in the case of H_2D^+ and D_2H^+.

2.1 Production and destruction of H_3^+, H_2D^+ and D_2H^+

The reaction that represents the creation of triatomic hydrogen cations in an interstellar setting was already denoted in equation 1.1. However, an important precursor reaction is the ionization of molecular hydrogen

$$H_2 + \zeta \rightarrow H_2^+ + e^- \tag{2.1}$$

followed by

$$H_2^+ + H_2 \rightarrow H_3^+ + H + 1.76\,eV \tag{2.2}$$

that ties the cosmic ray ionization rate ζ together with abundances of H_2^+, H_2 and H_3^+ under astrophysical conditions. The exothermic production reaction of H_3^+ is very efficient and predominantly limited by the availability of H_2^+. Thus, knowledge regarding the creation and destruction rates of these molecules and their abundances are intertwined and a crucial part of understanding the role of hydrogen in astrophysics.

Due to the low proton affinity of H_2 ($\approx 4.4\ eV$), the triatomic hydrogen ion is often referred to as a universal protonator marking one of the molecule's fundamental roles in astrochemistry, where it serves as a gateway to creation of more complex systems. The proton transfer reactions can be summarized in the following equation:

$$H_3^+ + X \rightarrow XH^+ + H_2 + \Delta E \tag{2.3}$$

After formation of H_3^+, the creation of its isotopologues are driven via three key reactions:

$$H_3^+ + HD \rightleftarrows +H_2D^+ + H_2 + \Delta E \tag{2.4}$$

$$H_2D^+ + HD \rightleftarrows D_2H^+ + H_2 + \Delta E \tag{2.5}$$

$$D_2H^+ + HD \rightleftarrows D_3^+ + H_2 + \Delta E \tag{2.6}$$

with the exothermicity of the reactions governed by a ΔE of ≈ 232, 187 and 234 K, respectively. Eventually, H_3^+ and its isotopologues initiate ion–neutral reactions (equation 2.3), paving the road for formation of more complicated molecules or are destroyed by dissociative recombination processes in collisions with free electrons.

2.2 Molecular structure

2.2.1 Basic considerations

The Schrödinger equation and Born–Oppenheimer approximation serve as key pillars of quantum chemistry. The former governs the evolution of the wave function Ψ of a quantum mechanical system while the latter states that due to the mass difference between nuclei and electrons, the electrons immediately adapt to changes in a given nuclear configuration. As a consequence, the nuclear and

electron motion can be viewed as decoupled. The time independent variant of the Schrödinger equation can be expressed as:

$$H\Psi(\vec{R}_k, \vec{r}_i) = E\Psi(\vec{R}_k, \vec{r}_i), \tag{2.7}$$

where R_k and r_i represent the nuclear and electron coordinates, respectively. The Hamilton operator:

$$H = -\sum_k \frac{\hbar^2}{2M_k}\Delta_k - \sum_i \frac{\hbar^2}{2m_\mathrm{e}}\Delta_i + \frac{e^2}{4\pi\varepsilon_0}\left(\sum_{k,l<k}\frac{Z_k Z_l}{\left|\vec{R}_k - \vec{R}_l\right|} + \sum_{i,j<i}\frac{1}{\left|\vec{r}_i - \vec{r}_j\right|} - \sum_{i,k}\frac{Z_k}{\left|\vec{r}_i - \vec{R}_k\right|}\right) \tag{2.8}$$

consists of kinetic energy terms of all involved particles and their respective Coulomb interactions, where M_k, m_e corresponds to the mass of the nuclei and electron, while $Z_{k,l}$ denotes the nuclear charge states of the individual particles.

According to the Born–Oppenheimer approximation the wave function can be separated as:

$$\Psi(\vec{R}_k, \vec{r}_i) = \Psi_\mathrm{nu}(\vec{R}_k)\Psi_\mathrm{el}(\vec{R}_k, \vec{r}_i) \tag{2.9}$$

and the energy eigenvalues of the Hamiltonian in the case of a molecule can be written as:

$$E(\vec{R}_k) = U_n(\vec{R}_k) + E_\mathrm{vib}(v) + E_\mathrm{rot}(J) \tag{2.10}$$

where the total energy dependence can be separated into electronic, vibrational and rotational contributions. A typical approach to derive properties of the molecular structure starts by solving the electronic Schrödinger equation for a set of nuclear coordinates R_k. The outcome can be approximated by a function that yields a potential energy surface (PES) that corresponds to $U_n(\vec{R}_k)$. Subsequently, to account for molecular vibration and rotation the eigenfunctions that satisfy the nuclear Schrödinger equation must be found:

$$H_{nu}\Psi_{nu} = E\Psi_{nu}, \qquad \Psi_{nu} = \Psi_{nu}(\vec{R_k}) \tag{2.11}$$

Due to the high degree of complexity that arises from interactions among electrons and nuclei, only the simplest cases of molecular structure calculations feature analytical solutions. A variety of approximate methods have been developed to address the problem numerically, such as the Hartree–Fock method, density functional theory, variational methods to name a few.

2.2.2 Geometry and potential surfaces

Regarded as the simplest polyatomic molecular ion, H_3^+ takes the shape of an equilateral triangle in its ground state, while the deuterated isotopologues H_2D^+ and D_2H^+ represent the shape of isosceles triangles as depicted in figure 2.1 (Kozin, Roberts, and Tennyson 2000).

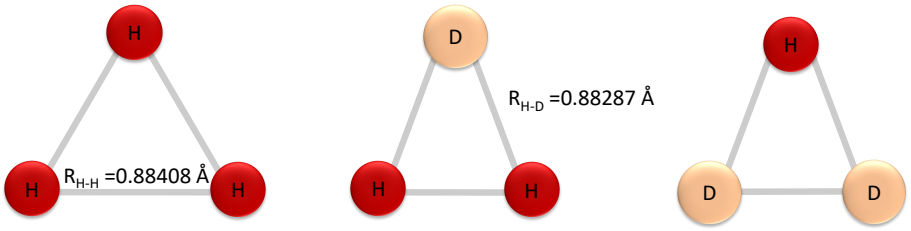

Figure 2.1: Schematic representation of H_3^+, H_2D^+ and D_2H^+ ground state geometry. Bond lengths take from Dalgarno et al. 1973

No stable electronically excited states have been observed for H_3^+ and its isotopologues, therefore the following description is only concerned with the ground state potential energy surfaces. The potential energy surfaces of H_3^+, H_2D^+ and D_2H^+ are essentially identical within the Born–Oppenheimer approximation. The most advanced theoretical approaches begin with *ab initio* calculations of the non–deuterated variant, thereafter including corrections to the PES associated to the deuteron. Ultimately, to refine the assignment of rovibrational states, various other corrections are employed (adiabatic, relativistic, QED) to the Born–Oppenheimer approximation and the final fit of the PES is compared to spectroscopically accurate measurements.

One of most impactful *ab initio* PES for triatomic hydrogen and its isotopologues was calculated by W. Meyer, Botschwina, and Burton 1986. This global PES has served as the basis of many modern calculations. Thereafter, Neale, Miller, and Tennyson 1996 expanded upon previous work by computing a more extensive line–list that consisted of $\approx 3{\cdot}10^6$ states. The fitted PES included states up to $15000\,cm^{-1}$ and was able to reproduce experimentally determined energy levels with a standard deviation on the order of $\approx 0.01\,cm^{-1}$. Such accuracy was attained due to the simultaneous fit of all three isotopologues, which incoporated the *ab initio* asymmetric adiabatic surfaces of H_2D^+ and D_2H^+ (Polyansky et al. 1995). The aforementioned line–list is considered reliable until energies of $\approx 10000\,cm^{-1}$, in part due to the absence of spectroscopically accurate data (at that time) to benchmark the results, and the linearity problem. It is interesting to note, that around energies of $\approx 10000\,cm^{-1}$ the molecule can sample linear

geometries via the vibrational movement, for which the theoretical basis sets that are adapted for the ground triangular geometries are ill suited. Although spectroscopic data above the so called barrier to linearity is available (Kreckel et al. 2008), not even half of the energetical landscape has been experimentally investigated, hindering the reliability of any available line–list at high excitation energies. However, inaccuracies of highly excited triatomic hydrogen level energies are inconsequential to current experiment, as the molecular ensemble in question occupies only the lowest rotational states. The present work employs results from the most recent calculation of the H_2D^+ and D_2H^+ PES that include intricate corrections to the Born–Oppenheimer approximation (Bowesman et al. 2023). A full account of theoretical efforts goes beyond the scope of present work, a review of the experimentally confirmed line positions is available in (Furtenbacher et al. 2013).

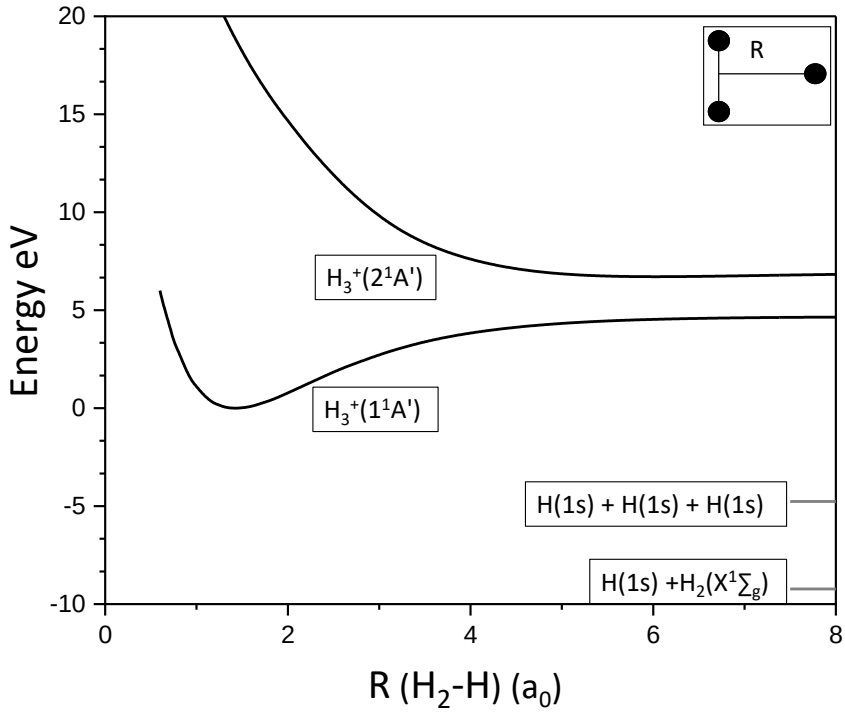

Figure 2.2: Potential energy curves of H_3^+ and the relevant energies of the two and three body dissociation channels. The PEC are depicted in Jacobi coordinates, as illustrated in the inset of the figure. The zero point energy is set to be at the bottom of the ground PEC of H_3^+. PEC taken from Urbain et al. 2019.

For simplicity, only the properties of the H_3^+ PES shall be briefly outlined,

while the nuances regarding the isotopologues will be addressed in the subsequent chapters. Figure 2.2 illustrates molecular potentials of the lowest $1^1\mathrm{A}'$ electronic state of H_3^+ and the repulsive $2^1\mathrm{A}'$ state in Jacobi coordinates, as indicated in the inset of the figure. The relevant dissociation channels in a DR reaction for the particular case of H_3^+ are:

$$\mathrm{H_3}^+ \rightarrow \begin{array}{c} \mathrm{H}(1s) + \mathrm{H}(1s) + \mathrm{H}(1s) \\ \mathrm{H_2}(v', J') + \mathrm{H}(1s), \end{array} \tag{2.12}$$

where the three–body channel kinetic energy (KER) release corresponds to $4.76\,eV$. The maximum KER of the two body break–up channel amounts to $9.23\,eV$ and is, in principle, dependant on the vibrational excitation on the $\mathrm{H_2}(v', J')$ product.

As a benchmark system for polyatomic calculations, the triatomic hydrogen ion and its isotopologues have received a lot of attention. Therefore, molecular potentials that guide the present experiment are considered to be highly accurate. The difficulty of understanding the dissociative dynamics stem from the inclusion of Rydberg states, as will be described in the subsequent paragraphs.

2.2.3 Wave function separation

The derivation of quantum numbers and selection rules provided in the following paragraph stems from the general assumption that the total wavefunction Ψ_{tot} that describes the properties of the molecular system is separable into four parts:

$$\Psi_{tot} = \Psi_{el}\Psi_{vib}\Psi_{rot}\Psi_{ns}, \tag{2.13}$$

where Ψ_{el} represents the electronic part of the total wave function, while Ψ_{vib} and Ψ_{rot} detail the behaviour of vibrational and rotational nuclear motion, and Ψ_{ns} denotes the nuclear spin wave function. The considerations that allow for separation of the total wavefunction are outlined in the following paragraphs.

The description of selection rules for transitions among internal states of any molecular system begins by finding good quantum numbers that arise from operations in a given point group framework. Two rigorous quantum numbers that hold true for any molecule are the total angular quantum momentum number F and parity $\mathrm{P} = \pm$ (Corney 2006). These quantum numbers are always considered to be well–defined while they do not arise from molecular properties, but rather from the Hamiltonians invariance in respect to inversion and rotation in space, or in other words due to isotropy and inversion symmetry of space itself. Dipole transitions obey selection rules described by quantum numbers F and P :

$$\Delta \mathrm{F} = 0, \pm 1 \quad (\mathrm{F} = 0 \nleftrightarrow \mathrm{F} = 0), \tag{2.14}$$

$$\Delta \mathrm{P} \neq 0 \quad (\pm \leftrightarrow \pm), \tag{2.15}$$

The quantum number F can be separated as:

$$\mathrm{F} = \mathrm{J} + \mathrm{I}, \tag{2.16}$$

where is J is referred to as the motional angular momentum and I is known as the nuclear spin angular quantum number. This sum is valid while the coupling among both motions is negligible. To a very good approximation the selection rules of dipole transitions for J and I are:

$$\Delta \mathrm{J} = 0, \pm 1 \quad (\mathrm{J} = 0 \nleftrightarrow J = 0), \tag{2.17}$$

$$\Delta \mathrm{I} = 0. \tag{2.18}$$

To summarize I, J and P are the only truly good quantum numbers at arbitrary energies for describing H_3^+, H_2D^+ and D_2H^+ molecular ions, while further selection rules are derived from symmetry considerations.

2.2.4 Group theory elements

H_2D^+ and D_2H^+ ions fall in the category of asymmetric–top molecules. The point group that represents such systems, and produces selection rules among molecular states defined by quantum numbers that are derived from symmetry properties, is called the C_{2v} point group. Classification of a molecule in a certain symmetry group allows for useful assessments of molecular properties (e.g. presence of dipole moment, overlap of dipole momentum integrals, etc.) that can be derived from symmetry operations without performing complicated numerical calculations. The present summary of group theory elements follows the definitions and nomenclature as found in (Inui, Tanabe, and Onodera 2012).

The basic symmetry operations are defined as rotation, reflection and inversion around either a point, line or plane. A common point group is identified if at least one common point remains unchanged after performing the five basic symmetry operations:

- Identity or unity operation E – trivial transformation, system remains unchanged,
- N–fold rotation by an angle of $360°/n$,

- Reflection in a mirror plane σ, which contains the principle molecular axis or in a plane perpendicular to it,
- Inversion through a symmetry centre according to a coordinate transformation of (x,y,z) $\rightarrow$ (-x,-y,-z),
- Inproper N–fold transformation S_n – a N–fold rotation transformation, followed by a reflection transformation through a plane that is perpendicular in respect to the rotational axis.

The relevant symmetry operations for H_2D^+, which are identical for D_2H^+, are reflected in figure 2.3. In order to define vibrational and rotational movement of molecules via symmetry operations, it is useful to summarize the transformations in multiplication and character tables, as seen in table 2.1. The multiplication table outlines the products of symmetry operations that are defined as consecutive transformations. It is clear that the noted four operators govern all symmetry transformations and thus they build the C_{2v} group with group of order four. The character table consists of the irreducible representations denoted by Mulliken symbols Γ: A_1, A_2, B_1 and B_2. The C_{2v} group features four classes or symmetry species that denote each of the one–dimensional (singly degenerate) irreducible representations, the purpose of which are to summarize symmetry properties of the system.

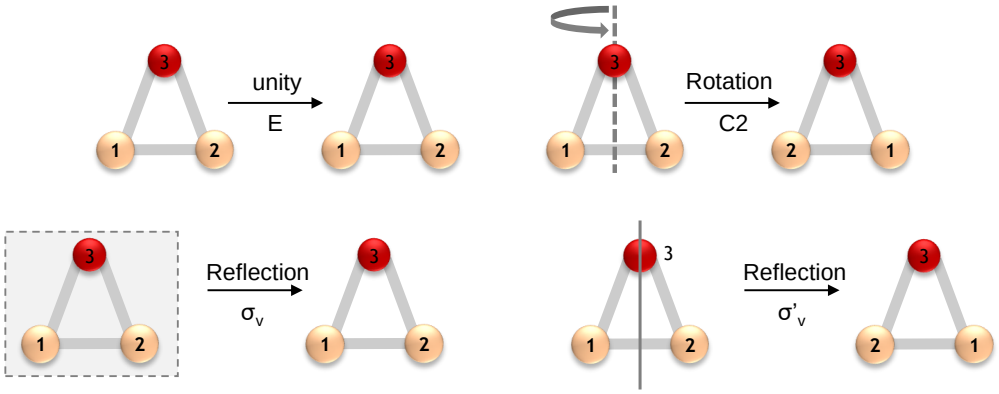

Figure 2.3: Symetry operations of the C_{2v} point group.

The so called characters ($\pm$ 1 in this case) indicate whether the rotational or reflection transformations are symmetric or antisymmetric, which further notes the change in sign of the system's wave function. In principle, the Mulliken symbols hold analogue information as the diatomic molecular state labels Σ, Π, Δ etc, but for polyatomic systems.

Table 2.1: Multiplication and character tables of the C_{2v} point group.

	E	C_2	σ_v	$\sigma_v^{'}$
E	E	C_2	σ_v	$\sigma_v^{'}$
C_2	C_2	E	$\sigma_v^{'}$	σ_v
σ_v	σ_v	$\sigma_v^{'}$	E	C_2
$\sigma_v^{'}$	$\sigma_v^{'}$	σ_v	C_2	E

C_{2v}	E	C_2	σ_v	$\sigma_v^{'}$
A_1	+1	+1	+1	+1
A_2	+1	+1	-1	-1
B_1	+1	-1	+1	-1
B_2	+1	-1	-1	+1

2.2.5 Vibrational modes

To describe the motion of an N nuclei molecule requires 3N coordinates. Three of them define the centre of mass position in respect to a chosen reference frame, while an additional three coordinates are necessary to describe rotation of the molecule's frame of reference in respect to the chosen laboratory frame. Therefore, 3N–6 coordinates remain to characterize the vibrational motion, which for the case H_2D^+ and D_2H^+ with N=3, leaves three internal coordinates.

In principle, the nuclear coordinates meant to describe vibrations of the molecule can be chosen arbitrarly, but in practice it is convenient to define them as linear combinations of the internuclear distances. For C_{2v} point group systems that represent the geometry of triangular configurations such internal coordinates transform according to their irreducible representation symmetry operations, which results in three decoupled vibrations, referred to as normal modes. Conventionally, the three modes are labelled with their respective vibrational quantum numbers as follows: symmetric stretch (breathing) mode v_1, bending mode v_2 and asymmetric stretch mode v_3 as depicted in figure 2.4. It can be shown that the total displacement of the three elements is characterized by the irreducible decomposition:

$$\Gamma_{tot} = \Gamma_{trans} + \Gamma_{vib} + \Gamma_{rot}, \tag{2.19}$$

where the motion that is associated with translations, vibrations and rotations can be expressed by:

$$\Gamma_{tot} = (A_1 + B_1 + B_2) + (2A_1 + B_1) + (A_1 + B_1 + B_2). \tag{2.20}$$

All displacement patterns that represent the normal mode vibrational motion can be achieved as linear combinations of their respective irreducible representations as depicted in the character table 2.2.

Table 2.2: Character table describing normal modes of the C_{2v} point group

	E	C_2	σ_v	σ_v'	Γ
v_1	+1	+1	+1	+1	$= A_1$
v_2	+1	+1	+1	+1	$= A_1$
v_3	+1	-1	-1	+1	$= B_2$

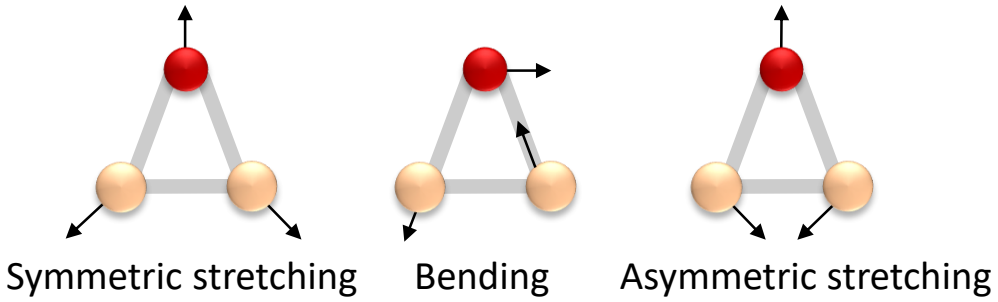

Figure 2.4: Normal modes of D_2H^+.

2.2.6 Rotations

To simplify the description of rotational motion, it shall initially be considered as decoupled from vibrations. According to the C_{2v} point group, all displacement associated with molecular rotation (labelled as R_x, R_y, R_z) can be expressed by the irreducible representations A_1, B_1 and B_2, as seen in table 2.3. The corresponding quantum numbers for the asymmetric top case of H_2D^+ and D_2H^+ are denoted as K_a and K_c, which arise as projections of J on to the principal molecular C_2 axis and the axis orthogonal to it in the plane that contains the nuclei, as illustrated in figure 2.5. The total motional quantum number J together with its projections, K_a and K_c are therefore sufficient to label the rotational transitions within H_2D^+ and D_2H^+. Additionally, the rotational angular quantum number K_c can be used to determine the total parity sign, which is given by $(-1)^{K_c}$. Further details of molecular rotational motion in the framework of the C_{2v} point group can be found in (Bowesman et al. 2023).

2.2.7 Nuclear spin

The nuclei that make up the molecular system are characterized by their individual momentum which can couple together to produce a total nuclear spin. The corresponding wavefunction Ψ_{ns} features permutation symmetry that constricts the amount of possible energy levels with their respective rovibrational

Table 2.3: Character table describing rotational motion of the C_{2v} point group

	E	C_2	σ_v	σ_v'	Γ
R_x (yz)	+1	-1	-1	+1	$= B_2$
R_y (xz)	+1	-1	+1	-1	$= B_1$
R_z (xy)	+1	+1	-1	-1	$= A_2$

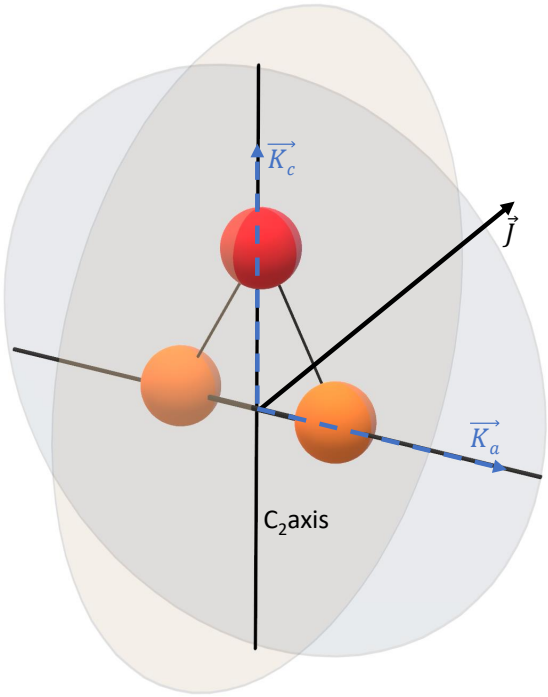

Figure 2.5: Motional angular momentum $\vec{J}$ and its projections $\vec{K_a}$, $\vec{K_c}$.

state labels. Only certain nuclear spin symmetries (modifications) are allowed, which are commonly referred to as para, meta and ortho. For the case of H_2D^+ and D_2H^+ the molecular constituents are protons with a spin of $I = 1/2$ and deuterons with $I = 1$. The projection of the elementary spin I on a reference axis represents the corresponding magnetic momentum, which can take on the values of $-I, -I+1...I$. Therefore, the nuclear spin I describes a $2I+1$ number of degenerate states. The symmetry transformation associated with nuclear spin modifications corresponds to coordinate inversion, which are described by the irreducible representations Γ: A_1, A_2, B_1, B_2. Table 2.4 illustrates a summary of the irreducible representations in the case of H_2D^+ and D_2H^+ and their correlation

to nuclear spin manifolds.

The total degeneracy g_{tot} of a rovibrational state for H_2D^+ and D_2H^+ described in C_{2v} point group symmetry consists of :

$$g_{tot} = g_J g_I, \tag{2.21}$$

where g_J denotes the rotational degeneracy due to projections of angular momentum J as described in the previous paragraph

$$g_J = 2J + 1 \tag{2.22}$$

and g_I expresses the splitting of rotational levels due to either para or ortho nuclear spin modification. In a general case, the total nuclear spin degeneracy of a molecule consisting of n nuclei with corresponding elementary spins I_i can be calculated according to:

$$g_n = \prod_i^n (2I_i + 1). \tag{2.23}$$

For H_2D^+ this results in 12 possible degeneracies from which $g_I = 3$ are of para nuclear spin modification and $g_I = 9$ of ortho, while in the case of D_2H^+ the total degeneracy count is 18 with $g_I = 6$ para and g_I= 12 nuclear spin modifications respectively. Additionally, it is important to note that due to the selection rule $\Delta I = 0$, transitions among nuclear spin isomers are forbidden. In summary, the

Table 2.4: Possible nuclear spin modifications of H_2D^+ and D_2H^+.

	H_2D^+		D_2H^+	
Γ	Isomer	g_I	Isomer	g_I
A_1, A_2	p	3	o	12
B_1, B_2	o	9	p	6

C_{2v} point group framework is used to characterize the vibrational modes and rotational states of H_2D^+ and D_2H^+(Bowesman et al. 2023). Therefore, all transitions of both molecules are described by the same set of quantum numbers and state labels: $v_1, v_2, v_3, J, K_a, K_c, p/o, +/-, g_{tot}, \Gamma$. The vibrational quantum numbers v_1, v_2, v_3 represent their respective vibrational modes: symmetric stretching, bending and antisymmetric stretching. The angular momentum quantum number J and its projections K_a, K_c, identify rotational states, while the para and ortho nuclear spin modifications identify the appropriate symmetry group denoted by Γ.

2.3 Molecular cation reactions with electrons

In the general case of an abstract triatomic molecular ion $ABC^+(n,v,J)$ that occupies a certain electronic (n), vibrational (v) and rotational (J) state, the relevant reactions in the context of the present work are:

- Dissociative recombination:

$$ABC^+(n,v,J) + e(E_{kin}) \rightarrow ABC^{**} \rightarrow A(n') + B(n'') + C(n''') + E_{KER}$$

- Dissociative excitation:

$$ABC^+(n,v,J) + e(E_{kin}) \rightarrow ABC^{**} \rightarrow A^+(n') + B+(n'') + C+(n''') + e'(E_{kin})$$

- Elastic collision:

$$ABC^+(n,v,J) + e(E_{kin}) \rightarrow ABC^{**} \rightarrow ABC^+(n,v,J) + e'(E_{kin})$$

- Inelastic collision:

$$ABC^+(n,v,J) + e(E_{kin}) \rightarrow ABC^{**} \rightarrow ABC^+(n',v',J') + e'(E_{kin})$$

where $e(E_{kin})$ denotes an electron with a certain kinetic energy. Note, that this list does not fully represent all of the possible break up channels of the DR and DE reactions for triatomic systems. A comprehensive description pertaining to the particular case of H_2D^+ and D_2H^+ shall be given in the following paragraphs. In all of the presented examples, the highly excited molecular neutral ABC^{**} is expected to autoionize on timescales from pico to femto seconds.

An elastic collision does not significantly influence the momentum of the ion, while the trajectory of the outgoing electron can be drastically changed due to the large mass difference among the collisional partners. Furthermore, the internal state of ions remains unchanged.

On the contrary, the inelastic collisions may lead to excitation or de–excitation of the molecule and although this process is not the main driving force of interstellar chemistry, it can certainly influence the internal energy distribution of molecules. According to theoretical calculations (see figure 3.3), the cross-sections of this process typically peak below few tens of mili–electronvolts in relative collision energy, therefore the changes within population occur among rotational states of the molecules. As present work strives to achieve results that can be described on the basis of individually populated quantum states, the inelastic collision process must be considered. Further discussion regarding this topic is available in chapter 3.

The main reactions of interest when considering the astrophysical relevance of H_2D^+ and D_2H^+ molecular ion lie within the dissociative processes, with particular emphasis on DR, which serves as the defining process at low collisional energies. During DR the incident electron recombines with the molecular ion and the resulting neutral breaks up with the excess kinetic energy being redistributed among the reaction fragments, denoted by the term E_{KER}. A comprehensive overview of this particular reaction will follow in the next paragraph.

A similar, yet clearly distinct process that competes with DR is dissociative excitation, with the key difference emphasized by the reaction fragments. In DE, the kinetic energy of the electron goes towards excitation of an unstable electronic state of the molecular ion prior to dissociation into charged and neutral fragments. Typically, such electronic states are located at least several electronvolts above the ground molecular state, hence the signal that originates from DE does not overlap with DR at small collisional energies. Furthermore, DE is very unlikely to occur in low density and temperature environments, therefore it is not particularly important for astrochemistry of the ISM.

2.4 Dissociative recombination

The subject of electron–ion interactions has been pursued for more than 70 years, with the initial focus directed towards examining the relevance of such reactions in atmospheric processes. The first mention of dissociative recombination in literature can be found in the work of Bates 1950, where prior experiments of microwave excited plasma (Biondi and Brown 1949) and the role of DR of molecular ions therein is discussed. Bates already notes that: "... accurate computations for any specific ions would be extremely difficult to perform". Decades after this prediction merely a small number of molecular systems can be regarded as fully investigated and understood, most of them being diatomics. The principle complication to acquiring reliable DR cross sections for both theory and experiment stems from the large number of electronical and rovibrational states involved and their mutual interactions. This problem is further exacerbated by going from a diatomic to triatomic molecule. Therefore, it is beneficial for both experiment and theory, to reduce the number of occupied molecular states of the investigated system as much as possible. The present experiment aims to extend the thorough work performed for understanding DR of diatomic molecular ions to the isotopologues of the simplest triatomic ion – H_2D^+ and D_2H^+. In the particular case of

DR of H_2D^+ and D_2H^+, the reaction channels are:

$$\begin{array}{lcllcllcl} H_2D^+(v,J)+e^- & \rightarrow & H_2D^{**}(v'J') & \rightarrow & H & + & H & +D & 4.67\,eV \\ & & & & HD & + & H & & 9.18\,eV \\ & & & & H_2 & + & D & & 9.15\,eV \end{array}$$

$$\begin{array}{lcllcllcl} D_2H^+(v,J)+e^- & \rightarrow & D_2H^{**}(v'J') & \rightarrow & H & + & D & +D & 4.72\,eV \\ & & & & HD & + & D & & 9.23\,eV \\ & & & & D_2 & + & H & & 9.28\,eV \end{array}$$

with a two–to–three body dissociation channel branching ratio of roughly 1:3 (**D**atz 1995). Dissociation energies taken from Strasser et al. 2004 and Sprecher et al. 2010.

2.4.1 Direct and Indirect DR processes

Dissociative recombination can occur via two fundamentally distinct transition pathways denoted as the direct and indirect processes. The principle reactions are illustrated in figure 2.6, which outlines the key differences among both of the mechanisms. To simplify, the processes are explained by potential energy curve examples of diatomic systems.

The DR reaction is initiated from a certain electronic and rovibrational state which lies somewhere on the PEC of the molecular ion AB^+. In the case of the direct process, the electron directly undergoes a transition from the ground electronic state into the dissociative state AB^{**} (figure 2.6 left), which eventually leads to fragmentation, accompanied by some kinetic energy release distributed among the neutrals. In the triatomic hydrogen ion and its isotopologues, the dissociative state is energetically located relative to the ionic ground state such that a direct transition occurs after exceeding collisional energies of $\sim$ 3–4 eV. As the dissociative state does not have any discrete energy levels, the rate coefficient for direct DR is expected to be free of sharp resonances.

The indirect process, which dominates the rate coefficient at low collisional energies $<$ 1 eV for the particular cases of H_2D^+ and D_2H^+, is characterized by an additional transition step not present in direct DR. As seen in figure 2.6 (right), indirect DR proceeds via the incident electron capture into a neutral Rydberg state AB_R. In principle, there exists an infinite series of Rydberg states

that converge towards the ground state of the molecular ion, which are located energetically below it. If the PEC of the dissociative state crosses a Rydberg state, the molecule can undergo dissociation by coupling from AB_R to AB^{**} states. The indirect DR typically occurs when the collisional energy matches the energy difference between the Rydberg and ion rovibrational states, manifesting as sharp resonances in the rate coefficient or as a stark decrease in the observed rate due to interference among the direct and indirect channels.

The first attempt of theoretical calculations to comprehensively explain the DR process were performed for the case of H_2^+ collisions with electrons (Giusti-Suzor, Bardsley, and Derkits 1983). One of the key conclusions of the aforementioned study was the prediction that the electron capture cross section σ process follows an $\sim 1/E$ collisional energy dependence and by extent a $\alpha \sim 1/\sqrt{(E)}$ or $\alpha \sim 1/\sqrt{(T)}$ dependence on the rate coefficient. It is to be noted, that this is usually only visible in the direct DR process.

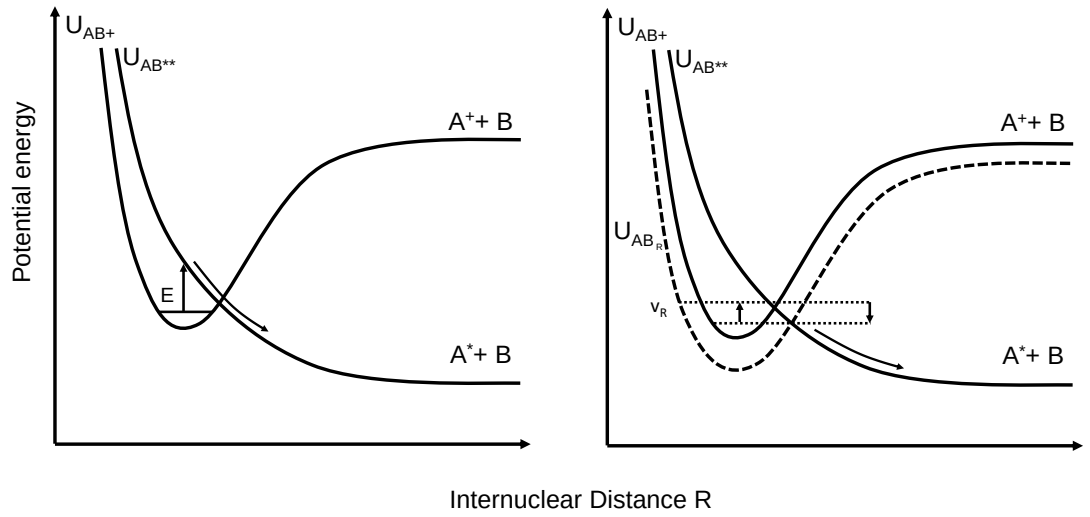

Figure 2.6: Sketch of the direct (left) and indirect (right) DR processes. The indirect DR is illustrated to procced via a vibrational Rydberg transition.

2.5 Recent theory

2.5.1 MQDT

The following paragraph shall outline the principles of Multichannel Quantum Defect Theory (MQDT) and its application for cross section calculations in the context of the present work. MQDT is a well–established approach for calculating cross sections of collisional processes. The current summary of main principles is based upon a review article by (Ross 1991), while specifics pertaining to MQDT used in dissociative recombination calculations follows notation as described in (Giusti 1980) and (Florescu-Mitchell and Mitchell 2006). The most recent theoretical treatment of the DR process of H_2D^+ and D_2H^+ can be found in the work of (Kokoouline and Greene 2005a).

In the framework of MQDT, the DR process is described as a collision between a positive ion in its rovibronic state of energy E_{v^+} and an electron with energy ϵ. Therefore, the total energy of such system can be expressed as:

$$E_{v^+} + \epsilon = E, \tag{2.24}$$

where the reaction ends in dissociation, with the total energy of the system being conserved as

$$E = E_{diss} + E_{kin}, \tag{2.25}$$

where E_{kin} is the kinetic energy of the fragments, while E_{diss} denotes the energy of the dissociative state.

Alternative to DR, the molecule can also autoionize during an elastic or inelastic collision process, where the ion captures the scattering electron:

$$E = E_{v^{+\prime}} + \epsilon^{'} \tag{2.26}$$

As stated before, the DR can proceed via the direct or indirect channels (figure 2.6) with the latter associated by transitions via Rydberg states. The largest hurdle in any calculation that tries to reproduce accurate DR cross sections lies within the inclusion of such Rydberg states, the number of which can in principle be infinite. MQDT tackles this issue by combining all of the Rydberg series into a singular channel that is thereafter treated as a quasi quantum state characterized by an Rydberg electron with an orbital angular quantum momentum $\vec{l}$ that features projections onto the internuclear axis Λ. Such assumptions reduce the problem of infinite Rydberg states to a finite representation. A given Rydberg series features N_v number of dissociation limits related to vibrational energies v of the ion, which are described by the following notation:

- $\vec{q}^{+}$, $\vec{r}$, $\vec{R}$: coordinates of the bound electrons, coordinates of the scattering electron, internuclear distance in a molecule–fixed system,
- l, $\tilde{l}$: diabatic and adiabatic approximate quantum numbers of the angular momentum $\vec{l}$ of the scattering electron
- $\vec{J} = \vec{N}^{+} + \vec{l}$, where $\vec{N}^{+}$ denotes the the angular momentum of nuclear rotation of the ion

MQDT is implemented by defining a number of PES $U_{n,l}(R)$ of their respective Rydberg states that deviate from the ground ionic potential $U_{\text{ion}}(R)$ by a dimensionless quantity denoted as the quantum defect $\mu_{l,\Lambda}$. The effective quantum number n^* of a Rydberg state is defined as:

$$n^* = n - \mu_{l,\Lambda} \tag{2.27}$$

and thus the resulting PES of a Rydberg state is expressed by a modified Rydberg series formula:

$$U_{n,l}(R) - U_{\text{ion}}(R) = -\frac{1}{2(n - \mu_{l,\Lambda}(R))^2} \tag{2.28}$$

In order to comprehensively describe the DR process, the reaction is divided into two collisional regions, depending on the scattering electrons vicinity to the nucleus:

- Inner reaction zone: $r < r_0$; $R < R_0$. R_0 and r_0 are critical values (on the order of few tens of a.u.) that vary depending on systems in question, where all electrons, including the impinging one are affected by the same short range, many body interactions and therefore the Born–Oppenheimer approximation is valid when considering the molecular wavefunctions.
- Outer reaction (asymptotic) zone: $r > r_0$; $R > R_0$, where only the long–range Coulomb interaction impacts the impinging electron. The angular momentum of the ion and electron are fully decoupled. Both, ionization and dissociation channels are well-defined.

Literature often includes a third reaction region referred to as the intermediate zone $r > r_0$; $R < R_0$, where the nuclei and electrons of the ion still interact with the scattering electron, but the Born-Oppenheimer approximation already breaks down due to the coupling among angular motion of the electron and the nuclear rotation.

Thereafter, wavefunctions corresponding to each of the interaction zones are constructed to eventually compose a total wavefunction of the system $\Psi(\vec{q}^{+}, \vec{r}, \vec{R})$.

One of the main ideas in MQDT is the notion to describe the DR prosses in terms of a number of dissociation channels $N = N_v + N_d$ (N_v – auto ionization channels, N_d – dissociation channels) each corresponding to their respective interaction region. This is typically done in the formalism of scattering theory, where a plane wave e^{ikr} representing the impinging electron scatters on the ion. The scattered wave that describes the ionization into a certain channel holds information imparted by the field that was experienced by the electron, which together with the scattering matrix S entails all information regarding the nature of the collision.

As an example, a partial DR cross section that occurs through a dissociation channel d_i described by a partial wave l that scatters of the ion located in an vibrational level v_0^+ can be expressed as:

$$\sigma_{v_0^+} = \frac{\pi}{2k^2}\rho\left|S^l_{d_i,v_0^+}\right|^2 \tag{2.29}$$

where ρ represents the multiplicity ratio among the final neutral electronic state and the initial ionic electronic state. A total cross section can thereafter be obtained as a sum of the partial ones. Therefore, a key aspect of a successful MQDT calculation lies within obtaining the scattering matrix S elements, which are determined via different matrices and their transformations whose eigenvectors may be used for building the S matrix. The correlation between the scattering matrix S and the typically utilized K, T, X matrices shall be omitted as it involves a mathematically heavy procedure.

In summary, for MQDT to produce accurate results, the necessary inputs are:

- A precise electronic ground state potential $U_{ion}(R)$ with a number of reliably determined vibrational states N_v
- A number of well defined potentials $U_{d_i}(R)$ of the dissociative states N_d
- Good estimates for the quantum defect values $\mu_{l,\Lambda}(R)$ for the states of interest
- Clearly defined couplings among the interacting elements in their respective interaction zones

For further discussion of MQDT implementation and the mathematical apparatus that it necessitates, the reader is referred to (Florescu-Mitchell and Mitchell 2006) and (Kokoouline and Greene 2005a).

2.5.2 Electron impact excitation and de–excitation

As discussed in section 2.3, the internal state of molecular ions can be changed due to inelastic collisions with electrons. Therefore, it is crucial to determine the associated cross sections in order to infer its influence on the molecular ensemble.

The most recent theoretical studies (Hamilton, Faure, and Tennyson 2015) devoted to calculations of electron impact rotational excitation cross sections of astrophysically relevant diatomic cations emphasize the fundamental role of this reaction within the ISM. Similar calculations have been performed for the case of triatomic hydrogen (Faure and Tennyson 2003), however no published data pertaining to the specific case of the deuterated variants can be found as of yet. Computation of inelastic collision cross sections for the systems of interest as described within the formalism of (Hamilton, Faure, and Tennyson 2015) are currently under way (Faure and Tennyson 2023) and the preliminary results are included in present work. The following outline reiterates the main principles of electron impact rotational excitation calculations, while a comprehensive explanation can be found in (Lique and Faure 2019).

Typically, molecular ions that feature a large dipole moment are expected to have considerable rotational excitation cross sections with the magnitude scaling approximately to the square of the dipole moment (e.g. HCO^+ with $\mu = 4D$, (Faure and Tennyson 2001)). Although the molecular ions of interest in this work are characterized by smaller dipole moments, the inelastic collision process is expected to influence the evolution of the population distribution. The benchmark method for calculating electron impact excitation cross sections is based on the Coulomb–Born (CB) approximation (Boikova and Ob'edkov 1968; Chu 1975; Faure and Tennyson 2002; Neufeld and Dalgarno 1989). A simplified expression of the interaction process can be written as:

$$\mathrm{Ion}(J, K) + e^-(k) \rightarrow \mathrm{Ion}(J', K') + e^-(k'), \tag{2.30}$$

where J and K are the angular momentum and rotational quantum numbers that characterize a given molecular state, while k and k' denotes the initial and final momenta of the incident electron. k and k' are related by:

$$k'^2 = k^2 + 2(E(J, K) - E(J', K')), \tag{2.31}$$

where $E(J, K)$ is the energy of the molecular state.

The central assumption of the Coulomb–Born approximation states that collision excitation cross sections between incident electrons and target particles are defined by long–range interactions (analogue to the outer reaction zone in MQDT

as described in previous section). This in turn leads to the following cross sections for rotational excitation in a molecular system:

$$\sigma^{CB}_{J\to J+1} = \frac{4\pi^2 a_0^2}{3\sqrt{3}} \frac{E_0}{\Delta E} \left(\frac{\mu_D}{e a_0}\right)^2 \frac{(J+1)}{(2J+1)} \frac{\Delta E}{E} g_{ff}(w,e), \tag{2.32}$$

where E denotes the energy of the incoming electron that contributes ΔE excitation energy. The atomic unit of energy E_0 and Bohr radius a_0 are constants that account for appropriate dimensions of the expression, while $g_{ff}(w,e)$ corresponds to the Gaunt factor, which represents integration over wave functions of the long-range Coulomb interaction. The dominant term of equation 2.32 is proportional to the square of the dipole moment μ_D^2 and contains a selection rule that allows for the change of only one rotational or vibrational quanta for polar molecular systems (Lique and Faure 2019). However, further advances in electron impact excitation calculations in the form of R–matrix studies have demonstrated strong dependence of short–range effects that result in non–negligible rates for transitions with $\Delta J > 1$ (Faure and Tennyson 2003), while the standard CB theory becomes reliable for molecular ions with dipole momentum larger than approximately 2 D. The foreseen discrepancies expected to arise from the shortcomings of the CB approximation related to the inner interaction region have been addressed in recent calculations by (Faure and Tennyson 2023).

To account for the interactions in the inner region, the theoretical treatment relies on the adiabatic nuclei rotation (ANR) approximation (Chang and Fano 1972). ANR estimates nuclear motion to that of a rigid rotor, which allows for electron impact excitation cross sections to be calculated by the use of a frame transformation, which produces a common, fixed body reference frame wherein the angular momenta of the incoming electron and the rotational motion of the nucleus can be coupled. The resulting cross section can be expressed as a sum of T matrix elements :

$$\sigma^T = \frac{\pi}{(2j+1)k_i^2} \sum_{J,l,l'} (2J+1) \left| T^J_{j'l',jl} \right|, \tag{2.33}$$

where j' and l' denotes the approximate angular quantum number momentum of the nuclei and electrons in the fixed body frame.

The full electron impact excitation cross section is acquired by:

$$\sigma_{(J\to J+1)} = \sigma^T_{(J\to J+1)} + [\sigma^{CB}_{(J\to J+1)} - \sigma^{PCB}_{(J\to J+1)}]. \tag{2.34}$$

At the complete level of theory the total cross section $\sigma_{J\to J+1}$ calculations consist of low partial waves (l_{max}=4) within the fixed nuclei approximation accompanied by Coulomb–Born calculations for high partial waves ($l > 4$). The term σ^{PCB} is

referred to as "Born completion" and represents high partial wave values of $l > l_{max}$.

2.6 Open questions

The preceding chapter has outlined the history of triatomic hydrogen and the effort and progress from both, theoretical and experimental perspectives. However, there are several lingering questions surrounding H_3^+ and its isotopologues, some of which stem from the dissociative recombination process.

Any laboratory measurements of the dissociative recombination reaction are associated with difficulties that arise from the production and storage of molecules. Typically, ion sources produce molecular ions that are characterized by an initial temperature of several thousand kelvin, which are stored in room temperature environments. None of these aspects help to reproduce the conditions of the cold and diffuse interstellar medium where the DR reactions matter the most. Room temperature storage rings and traps equipped with electron coolers have addressed the issue by providing storage conditions such that the influence of vibrational excitation can be separated from the measured DR rate. Thereafter, cryogenic rings and traps have paved the road to achieve DR rates for molecules which are barely rotationally excited. However, outside of special cases, it is experimentally extremely difficult to address the DR reaction on the basis of individual quantum states. Therefore, the question: "to what degree does the inevitably remaining internal excitation contribute to the observed rate?" is almost always relevant.

The present work strives to address this issue by utilizing one of the most advanced cryogenic storage rings – the CSR in tandem with its low temperature electron cooler, in order to investigate the DR reactions with molecular ensembles of H_2D^+ and D_2H^+ that occupy only a handful of rotational states, thus advancing towards the goal of state selective dissociative recombination measurements of the triatomic hydrogen ion.

Another long standing question regarding DR of H_3^+ and its isotopologues relates to the contributions of the ortho and para manifolds to the measured rate at low temperatures. Although concrete conclusions regarding this issue can not be derived from present results, meaningful insights can still be gained at the level of internal state definition achieved in present work.

A significant amount of prior experimental results where obtained in relative measurements. Therefore, it is important to emphasize that the cross sections and

rate coefficients presented here are given as absolute values with a rather small overall uncertainty of around 22 % – a value that can be further improved upon.

Due to the availability of a low energy electron cooler which provides the possibility to reliably measure reactions with collision energies as low as $2\,meV$, the experimental rate coefficient can be obtained for the astrophysically relevant collisional range below $10\,meV$.

Lastly, there are no real benchmarks for the state-of-the-art theory calculations of the state–specific DR rates of the triatomic hydrogen ion. The obtained rate coefficients in present work represent the best currently available experimental results in terms of internal state definition to test said calculations.

Chapter 3

Simulations of H_2D^+ and D_2H^+ internal state dynamics during storage

In this chapter a description of a radiative relaxation model of H_2D^+ and D_2H^+ ions is presented with the purpose to asses the expected population distribution of the stored ion ensemble inside the Cryogenic Storage Ring (CSR). An overview of considerations regarding the production and initial conditions of the ion ensemble shall be outlined. The model calculations depict the radiative cooling process with the inclusion of ion–electron interaction effects, namely inelastic collisions and state selective depletion by dissociative recombination (DR). Information given by the time evolution of the internal excitations is a crucial aspect for preparation of the experimental DR measurement scheme and beneficial for the interpretation of the observed rate coefficients.

3.1 Basic considerations and previous findings

The production of triatomic hydrogen cations is typically achieved by ionizing a sample of H_2 gas, which creates an environment where the reaction among H_2 and H_2^+ can occur (equation 2.2) forming H_3^+. To produce H_2D^+ and D_2H^+ the target gas is changed to HD. The resulting plasma that contains the ions of interest is

characterized by a Boltzmann distribution with temperatures of several thousand kelvin. The ion source employed in the present work was a duoplasmatron ion source, which is described in more details in chapters 4.2 and 4.7.

One of the approaches to achieve a rovibrationally relaxed ion ensemble, is to store the ions in a storage medium that permits relaxation by radiative cooling. Under ideal conditions, the ions will equilibrate to a temperature governed by the storage medium. This strategy of course necessitates that the target systems feature an electric dipole moment or, at least, a transition dipole moment associated with rovibrational transitions. Therefore, radiative cooling alone is not sufficient to achieve a molecular ensemble that occupies only the ground molecular rotational states for the case of H_3^+ due to the absence of a permanent electric dipole moment and the large number of metastable rotational states. H_2D^+ and D_2H^+ however, feature a small yet significant dipole moment of 0.6 and 0.48 debye, respectively. This allows for the molecules to radiatively relax into their lowest rotational states on timescales on the order of a few thousands of seconds, as will be demonstrated in the following paragraphs.

To facilitate the storage of molecular ions on timescales that would fully take advantage of the radiative relaxation process requires a storage medium that offers cryogenic conditions and low residual gas pressures. Therefore, the CSR is an ideal instrument in which to store H_2D^+ and D_2H^+ ions to prepare them for the desired DR experiment. The experimental vacuum chambers of the CSR can reach temperatures lower than 10 K with residual gas particle density on the order of $\approx 1000\,cm^{-3}$, thus providing conditions where H_2D^+ and D_2H^+ will radiatevly cool to a small number of rotationally excited states. Such ion ensembles closely represent the minimal internal excitation of molecules located in interstellar conditions. A more detailed description of the CSR will follow in chapter 4.1.

As the ions were produced in a duoplasmatron ion source, a Boltzmann distribution of $3000\,K$ was assumed as the initial condition. Although this is a rough estimate of the ion temperature at production, the choice of the exact initial temperature is inconsequential as even the symmetric variant of the triatomic ion is shown to radiatively cool most of its internal energy in a few seconds while stored in a room temperature environment (Kreckel et al. 2004). Additionally, the same publication demonstrates that the stored ions couple to the ambient $300\,K$ radiation very weakly, which is corroborated by experimental evidence (Lammich et al. 2005).

Ion storage rings are one of the most powerful tools for studies of dissociative recombination. As such, they have been used in determining the DR rates in collisions with low energy electrons for H_3^+ and its isotopologues. The most re-

cent experiments that investigate the DR reaction have been performed in room temperature ion storage rings (H_2D^+: Datz et al. 1995, H_3^+: Lammich et al. 2003, D_2H^+: Zhaunerchyk et al. 2008), where for the case of D_2H^+ a sub–thermal molecular ensemble has been demonstrated. However, all of the aforementioned experiments have measured DR rates with rotationally hot ions. Present work strives to improve upon this issue by obtaining DR rates with rotationally cold ions for H_2D^+ and D_2H^+.

3.2 H_2D^+ and D_2H^+ line-list

The construction of a model that describes the development of population distribution among molecular levels as a function of time requires input from a comprehensive line–list that features sufficiently precise transition strengths between all of the involved states. In particular, radiative transitions are the most important ingredients in such a model, as radiative relaxation is the dominant mechanism for population transfer, as will be demonstrated shortly. Therefore, the simulations are based on the most recent, spectroscopically accurate line–lists calculated by (Bowesman et al. 2023) and co–workers in the frame work of the ExoMol project (Tennyson and Yurchenko 2012).

The complete H_2D^+ line–list is comprised of close to 33 thousand states connected by over 22 million rovibrational transitions that cover level energies up to $18500\,\mathrm{cm}^{-1}$, with total angular momentum quantum number J values ranging from 0–20, while the uncut version of the D_2H^+ line-list spans J values between 0–25 and consists of nearly 370 thousand states and 2.29 billion transitions that extend to state energies of nearly $35000\,\mathrm{cm}^{-1}$. In both cases the energy range and state density of the line–lists well exceeds the requirements to construct a model that simulates population distribution developement of cold molecular ions in a cryogenic environment. In its core, the line–lists were calculated within the formalism of triatomic discrete variable representation (DVR), which is a well–established approach for computing the rovibrational Hamiltonian of triatomic molecules (Szalay and Nemes 1994, Light and Carrington Jr. 2000). Initial energy levels and wave functions are obtained by the nuclear motion code DVR3D developed by (Tennyson et al. 2004). It should be noted that the DV3RD code is capable of producing highly accurate results as shown in the case of the non–deuterated triatomic hydrogen ion (Mizus et al. 2017, Furtenbacher et al. 2013), where the average standard deviation between experimentally determined and

theoretically calculated level energies was found to be $< 0.2\,\mathrm{cm}^{-1}$. The analysis of (Furtenbacher et al. 2013) that aimed to verify the accuracy of the line list, covers molecular states with frequencies up to $\sim 16500\,\mathrm{cm}^{-1}$ and reveals the majority of the low energy region ($< 2000\,\mathrm{cm}^{-1}$), relevant for the context of this work, is characterized by significantly smaller deviations – on the order of $\sim 0.05\,\mathrm{cm}^{-1}$. This comparison was obtained utilizing the MARVEL (measured active rotational–vibrational energy levels) protocol (Furtenbacher and Császár 2012; Furtenbacher, Császár, and Tennyson 2007), where empirical energy levels are constructed on the basis of high resolution assigned spectra with the purpose to increase the accuracy of transition frequency predictions. To refine the precision and extend rovibrational state labels, the final ExoMol line–list incorporates molecular levels acquired by the MARVEL procedure.

The H_2D^+ and D_2H^+ line–lists come in the form of two files titled – (states) and (transitions) respectively. These files detail the molecular levels with state specific information and assignments of quantum numbers, and provide transition strengths among them. In particular, the states files features the nomenclature that describes a molecular state, in essence consisting of one entry per state. The transitions file however, features the entire network of interactions consisting of tens of millions (up to several billion) of data entries, formated as three columns. The first two denote the numbering of the transition states, while the third column describes the Einstein A coefficient, which indicates the transition strength. An excerpt of the states and transition files can be seen in tables 3.1 and 3.2. Further details regarding the line–lists and their use in practical applications can be found in (Bowesman et al. 2023).

Table 3.1: Excerpt of ten lowest rovibrational states of H_2D^+ states file (Bowesman et al. 2023) following the nomenclature as established in Tennyson et al. 2004.

i	$\bar{E}$	g_{tot}	J	unc	τ	$+/-$	Γ_{rve}	$No.$	iso	ν_1	ν_2	ν_3	K_a	K_a	$Sourcetag$
1	0.00000	3	0	0.000E+0	inf	+	A1	1	p	0	0	0	0	0	Ma
267	45.70111	9	1	0.000E+0	2.475E+2	-	A2	1	p	0	0	0	0	1	Ma
449	60.02985	27	1	1.000E-5	inf	-	B1	1	o	0	0	0	1	1	Ma
632	72.45249	27	1	1.000E-5	8.197E+3	+	B2	1	o	0	0	0	1	0	Ma
733	131.65246	15	2	3.300E-5	3.300E+1	+	A1	1	p	0	0	0	0	2	Ma
1358	138.85912	45	2	2.100E-5	5.319E+1	+	B2	1	o	0	0	0	1	2	Ma
1186	175.93503	45	2	2.100E-5	2.300E+1	-	B1	1	o	0	0	0	1	1	Ma
1012	218.65452	15	2	3.606E-3	3.058E+2	-	A2	1	p	0	0	0	2	1	Ma
734	223.85769	15	2	3.606E-3	6.020E+1	+	A1	2	p	0	0	0	2	0	Ma
1849	251.41464	21	3	2.000E-3	1.172E+1	-	A2	1	p	0	0	0	0	3	Ma

Notes :
i: State counting number;
$\bar{E}$: Term value (cm^{-1});
g_{tot}: Total state degeneracy;
J: Total angular momentum quantum number;
unc: Estimated uncertainty of energy level (cm^{-1});
τ: Radiative lifetime (s);
$+/-$: Total parity;
Γ_{rve}: C_{2v} symmetry group;
$No.$: Symmetry group block counting number;
$isomer$: Nuclear spin isomer;
ν_1: Symmetric stretching quantum number;
ν_2: Bending quantum number;
ν_3: Asymmetrical stretching quantum number;
K_a: Rotational angular momentum quantum number;
K_c: Rotational angular momentum quantum number;
$SourceTag$: The method used to generate the term value; "Ma" for marvelized energies, "EH" for energies from effective Hamiltonian calculations and "Ca" for energies calculated using DVR3D.

Table 3.2: Excerpt from H_2D^+ transitions file (Bowesman et al. 2023) that lists transition strengths among molecular states.

f	i	A_{fi} s^{-1}
26031	27863	4.10E-2
5849	5203	4.24E-1
4726	2819	7.31E-1
17763	15841	5.13E-1
11357	9505	9.37E-2
16005	17469	3.50E-2
5429	3953	2.92E-1
6629	7838	1.17E-1
6843	6102	3.81E-1

f: The upper state counting number from the corresponding states file;
i: The lower state counting number from the corresponding states file;
A_{fi} s^{-1}: The Einstein A coefficient.

3.3 Modelling of the rovibrational cooling

The goal of the rovibrational relaxation model is to derive realistic, state–specific populations that depict the development of the molecular state ensemble as function of storage time within the CSR, while considering all relevant processes that might influence said population distribution. In order to achieve this objective, the following series of ordinary differential equations (ODE) has to be solved:

$$\frac{dP_i(t)}{dt} = -\frac{1}{\tau_i}P_i(t) - \sum_k P_i(t)B_{ik}\rho(\nu_{ik}) + \sum_k P_k(t)A_{ki} + \sum_j P_j(t)B_{ji}\rho(\nu_{ji}), \quad (3.1)$$

where P_i expresses the population of a certain state i at a particular time $P_i(t)$. Index i iterates over all of the molecular states within the model, index k energetically above state i and index j connects to levels below i.

The terms $\frac{1}{\tau_i}P_i(t)$ and $\sum_k P_k(t)A_{ki}$ account for population transfer due to spontaneous decay governed by the finite lifetime τ of rovibrational states given by:

$$\tau_i = \frac{1}{\sum_k A_{ik}}, \quad (3.2)$$

where the Einstein A_{ik} coefficients describing spontaneous emission are extracted from the line–lists explained in the previous paragraph.

The remaining terms $\sum_k P_i(t)B_{ik}\rho(\nu_{ik})$ and $\sum_j P_j(t)B_{ji}\rho(\nu_{ji})$ of equation 3.1 introduce interactions that represent excitation or de–excitation processes, such as coupling to an ambient radiation field or inelastic collisions between the stored ions and electrons. $\rho(\nu_{ik})$ defines the spectral energy density for a given transition frequency, while the induced absorption Einstein coefficients B_{ji} can be obtained by the relation:

$$B_{12} = \frac{2J_2 + 1}{2J_1 + 1} \frac{c^3}{8\pi h \nu_{12}^3} A_{21}. \tag{3.3}$$

A python script that predominantly relies on the SciPy module (Virtanen et al. 2020) for solving the coupled ODE system was developed. To numerically solve ODE problems with initial value conditions, the SciPy package employs the LSODE (Livermore Solver for Ordinary Differential equations) differential equation solver(Hindmarsh 1983; Hindmarsh 2019).

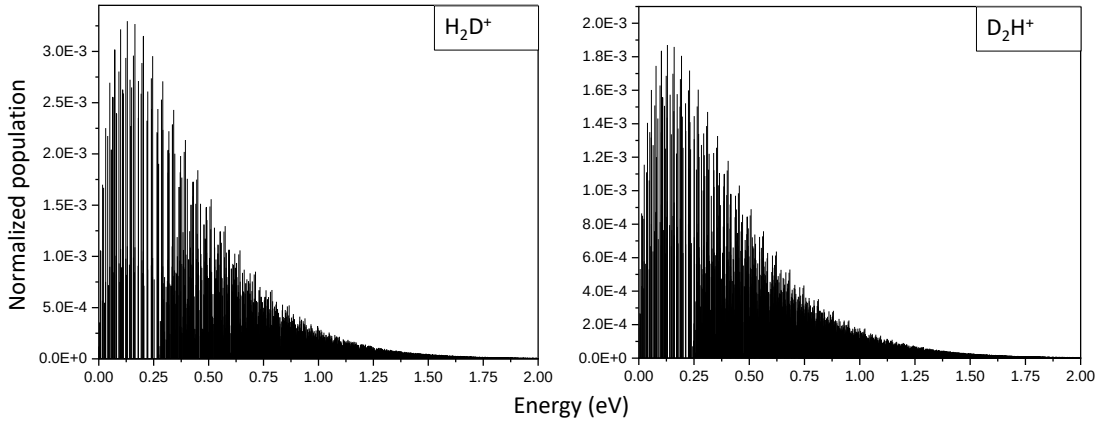

Figure 3.1: Stick diagram of initial conditions employed in the simulations. A Boltzmann distribution of $3000\,K$ is assumed as the start temperature of the molecular ensemble, resulting in a thermal population of thousands of rovibrational states.

A Boltzmann distribution of $3000\,K$ was assumed as an initial condition for $P_i(t = 0)$, determined by equation:

$$P_i(t = 0) = N_0(2J_1 + 1)g_i e^{-E_i/kT}, \tag{3.4}$$

with N_0 satisfying the normalization condition:

$$\sum_i P_i(t) = 1 \tag{3.5}$$

Figure 3.1 illustrates a stick diagram of the population distribution at initial conditions, depicting the large amount of rovibrational states occupied by a molecular ensemble that is characterized by a Boltzmann distribution of $3000\,K$. To fully account for transitions among all involved molecular states requires the input from a comprehensive line–list. In the context of present work, the D_2H^+ model is comprised of the first 50 thousand rovibrational states accompanied by a network of 59 million interactions, while the H_2D^+ line–list is included in its entirety with 33 thousand states and 22 million transitions among them. A typical simulation requires a run time of around 48 hours up to several weeks on a dedicated node of the MPIK computer cluster, depending on the maximum simulated storage time and the fineness of the assigned time bins. The limiting factor being the large memory requirements necessary to accommodate all of the transition network.

3.3.1 Radiative cooling

Initially, the simplest form of the model was constructed with the aim to simulate radiative relaxation from an initial population distribution, while neglecting any other effects. Thereafter, each subsequent effect is implemented in a step–wise manner to gain understanding of the degree of influence and relevance. Such an approach is beneficial for managing expectations and requirements of an upcoming experiment, and crucial for interpretation of acquired results.

Figure 3.2 ilustrates simulations of radiative cooling of H_2D^+ and D_2H^+ (solid lines) in an interaction free scenario, indicating the necessary time scales required for the rovibrational population to accumulate within a very limited number of states. H_2D^+ possess a slightly larger dipole moment compared to D_2H^+ ($0.6\,D$ for H_2D^+ and $0.48\,D$ for D_2H^+) and is characterized by fewer rotational states with lifetimes above $100\,s$, therefore H_2D^+ exhibits a faster cooling behaviour. Notably, the model calculations suggest that in the case of H_2D^+ the vast majority of population will be accumulated in only three rotational states after approximately 1000 seconds, enabling the prospect of state–specific measurements. It is important to note that the ortho and para nuclear spin states do not mix due to selection rule of $\Delta I = 0$. Therefore, the best attainable state definition without manipulating the ortho–para ratio of the system consists of two rotational states. As the first excited rotational ortho state of H_2D^+ is characterized by a lifetime that exceeds $8000\,s$, it is extremely unlikely to attain a better state definition than in present experiment.

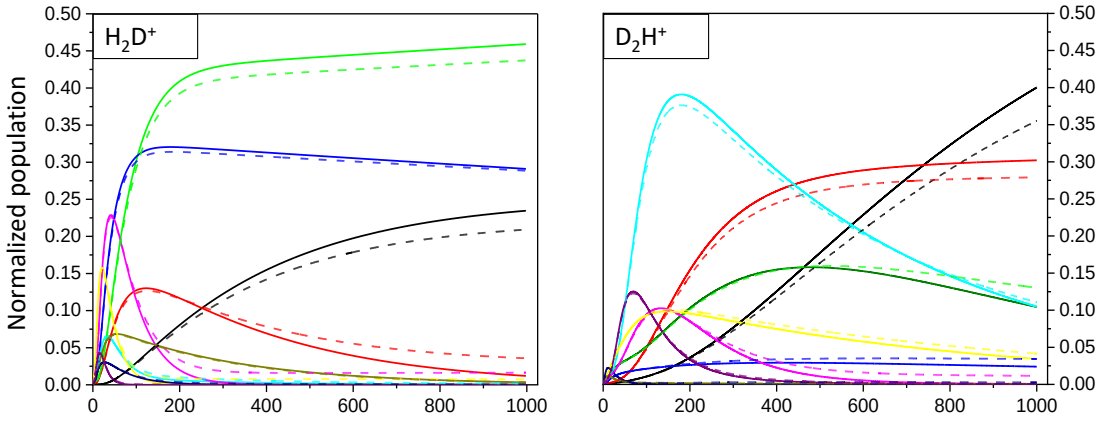

Nr	Energy (meV)	Lifetime (s)	J	K_a	K_c	o/p
1	0.00	Inf	0	0	0	p
2	5.67	247.52	1	0	1	p
3	7.44	Inf	1	1	1	o
4	8.98	8196.70	1	1	0	o
5	16.32	33.00	2	0	2	p
6	17.22	53.19	2	1	2	o
7	21.81	23.00	2	1	1	o

Nr	Energy (meV)	Lifetime (s)	J	K_a	K_c	o/p
1	0	Inf	0	0	0	o
2	4.33	Inf	1	0	1	p
3	6.11	302.90	1	1	1	o
4	7.19	1965.20	1	1	0	p
5	12.61	483.31	2	0	2	o
6	13.67	94.41	2	1	2	p
7	16.91	770.15	2	1	1	o

Figure 3.2: Simulated population distribution as a function of storage time. Solid lines represent a simulation scenario of rovibrational relaxation in a collisionless environment, while the dashed lines depict results which additionally incorporate radiative heating due to a two component black body radiation field ($99\,\%\ 6\,K + 1\,\%\ 300\,K$) that represents the experimental vacuum environment of the CSR.

3.3.2 Radiative heating

Although the CSR is a cryogenic ion storage ring, exposure to some ambient radiation inevitably remains. The main heating effects arise from the room temperature radiation field entering the CSR via sapphire viewports, meant for incoupling of laser light, and stray photons emitted by hot filament ion pressure gauges. Therefore, in the next step the model calculations incorporate coupling to a black body radiation (BBR) field to account for the heating processes.

The spectral density of a BBR field is calculated according to Planck's radiation law:

$$\rho(\nu) = \frac{8\pi\nu^2}{c^3}\frac{h\nu}{e^{h\nu/kT}-1}, \tag{3.6}$$

which together with the Einstein B coefficients from equation 3.3 embeds radiative absorption for each possible transition within the model. To best reflect realistic experimental conditions, the ambient radiation field consists of two components: A 99% 6 K part that represents the temperature of the experimental vacuum chamber with an additional 1% of a 300 K temperature field to account for radiation leaks into the CSR. Similar estimates have proven to be reliable in reproducing measured population distributions of rotationally cold ions in CSR experiments (Kálosi et al. 2021, 2022). Figure 3.2 portrays the impact of radiative heating (dashed lines) on the rovibrational population distribution compared to field–free (solid lines) simulations. A slight increase of internal excitations can be observed indicated by population transfer between the absolute ground and rotationally excited states.

3.3.3 Inelastic electron collisions

To account for changes in population distribution due to electron impact reactions, the next step includes recent cross sections from R–matrix calculations (Faure and Tennyson 2023), the main principles of which where already outlined in section 2.5.2. Cross sections for electron impact excitation as a function of collision energy can be viewed in figure 3.3, which are characterized by a maximum value when the collisional energy approaches $E = 0$ and decrease approximately to $1/E$ with increasing energy. As the initial simulation results of the radiative relaxation model indicate that the population distribution is mostly confined to less than ten molecular states already after $\sim$ 200 s, it is sufficient to include the inelastic collision process contribution among only the few relevant states in question. This constitutes the first lowest four states in the case of H_2D^+ and the lowest ten states for D_2H^+.

Full incorporation of the inelastic collision process within the population evolution model requires not only excitation, but also de–excitation cross sections $\sigma_{J+1\to J}$, which can be calculated by detailed balance:

$$g(J+1)E\sigma_{(J+1\to J)} = g(J)(E+\Delta E)\sigma_{(J\to J+1)}(E+\Delta E), \tag{3.7}$$

where $g(J)$ and $g(J+1)$ are the statistical weights of the lower and upper molecular levels, respectively.

The energy dependant theoretical cross sections $\sigma(E)$ cannot be directly incorporated into the model calculations. The experimentally relevant quantity is the merged–beams rate coefficient, which represents a rate coefficient obtained from collisions with electrons that are characterized by a certain collisional energy distribution, determined by the electron cooler. Therefore, to acquire a rate

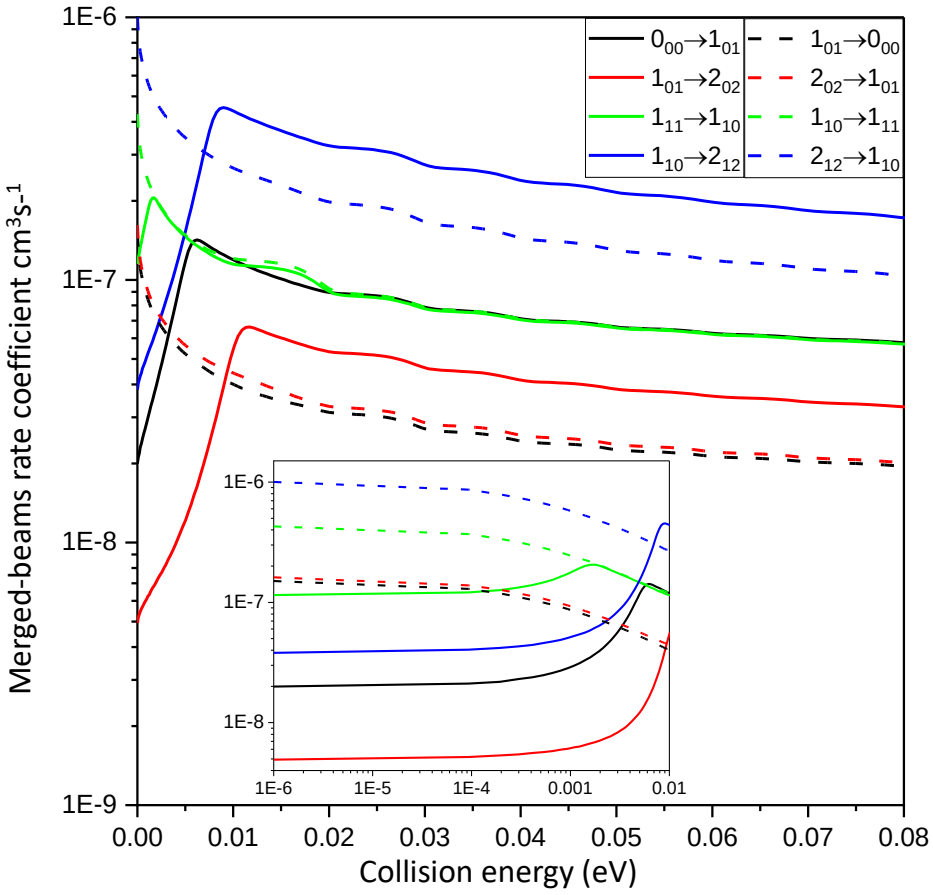

Figure 3.3: Electron impact excitation (solid lines) and de–excitation (dashed lines) merged–beams rate coefficients among the lowest rotational states for the case of H_2D^+. The MBRC of D_2H^+ are on the same order of magnitude and exhibit identical threshold character.

coefficient for transitions among molecular states that can be used in the model calculation, the cross section must be convolved with the collisional energy distribution function $f(E)$ to obtain merged–beams rate coefficients. Such a convolution is described by the following equation:

$$\alpha^{mb} = \sqrt{\frac{2}{m}} \int_0^\infty f(E)\sqrt{E}\sigma(E)dE, \tag{3.8}$$

where m is the mass of the electron and $f(E)$ is the energy distribution function given by the electron cooler (the derivation of the function $f(E)$ is described in chapter 4.9). The state–specific merged–beams rates at a given energy $\alpha^{mb}(J_{i\to j})$ corresponds to the rate of population transfer due to excitation or deexcitation

among the involved states and are incorporated in equation 3.1 to simulate the inelastic ion–electron collision process.

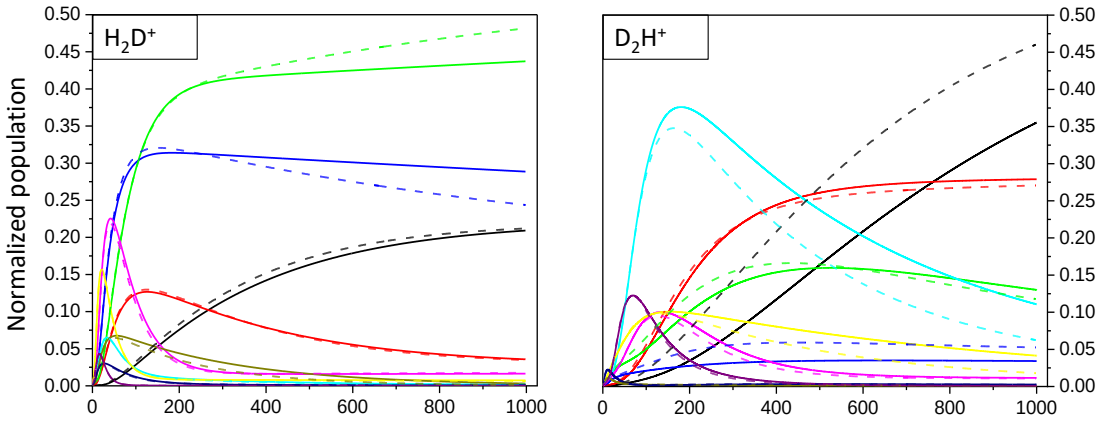

Nr	Energy (meV)	Lifetime (s)	J	K_a	K_c	o/p
1	0.00	Inf	0	0	0	p
2	5.67	247.52	1	0	1	p
3	7.44	Inf	1	1	1	o
4	8.98	8196.70	1	1	0	o
5	16.32	33.00	2	0	2	p
6	17.22	53.19	2	1	2	o
7	21.81	23.00	2	1	1	o

Nr	Energy (meV)	Lifetime (s)	J	K_a	K_c	o/p
1	0	Inf	0	0	0	o
2	4.33	Inf	1	0	1	p
3	6.11	302.90	1	1	1	o
4	7.19	1965.20	1	1	0	p
5	12.61	483.31	2	0	2	o
6	13.67	94.41	2	1	2	p
7	16.91	770.15	2	1	1	o

Figure 3.4: Simulated population distribution as a function of storage time. Solid lines represent a simulation scenario of rovibrational relaxation including radiative heating due to a BBR field, while the results indicated by dashed lines additionally incorporate electron impact excitation and de–excitation rates among the lowest molecular states that hold most of the population density.

The influence of the inelastic collision process can be gauged by performing some numerical estimates for the case of H_2D^+. If one assumes a typical electron density of $n_e = 1 \cdot 10^5\, cm^{-3}$ employed in present experiment and multiplies it by a theoretical rate coefficient for an excitation transition among the two lowest rotational states $\alpha^{mb}(0_{0,0} \rightarrow 1_{0,1}) = 1.42 \cdot 10^{-7}\, cm^3 s^{-1}$, the resulting number $R = n_e \cdot \alpha^{mb}(0_{0,0} \rightarrow 1_{0,1}) = 1.42 \cdot 10^{-2}\, s^{-1}$ represents the rate of ion transfer per second among the two molecular states. This comparison calculation considers the collision energy to be at the peak of the cross section (the full model calculations incorporate the MBRC value at $E_d = 1 \cdot 10^{-6}$). To account for the geometrical overlap of the ion and electron beams, R is multiplied by a factor l_0/C_0, where $l_0 = 0.721\, m$ is the merged–beams overlap length throughout the

CSR circumference $C_0 = 35.12\,m$, which results in the effective reaction rate of $R_{eff} = R \cdot (l_0/C_0) = 2.9 \cdot 10^{-4}\,s^{-1}$. The Einstein A coefficient that describes radiative relaxation for the same transition is $A = 4.0 \cdot 10^{-3}\,s^{-1}$. Therefore, for this particular example, it is evident that radiative relaxation occurs faster by more than an order of magnitude. In more general terms, the radiative cooling Einstein A coefficients of the highly excited molecular states are on the order of $A \approx 1 - 750\,s^{-1}$, thus overwhelming the inelastic excitation process. Therefore, electron impact excitation rates of the highly excited states are neglected in present model calculations.

The resulting contribution of inelastic collision interactions on the modelled population distribution compared to a scenario where this effect is omitted can be seen in figure 3.4, that indicates an overall de–excitation trend reflected by a slight population decrease in the excited states, which is transferred to energetically lower states.

3.3.4 State selective depletion by electron recombination

The most advanced theoretical work on dissociative recombination of H_2D^+ and D_2H^+ predict significant differences among the cross sections of the lowest rotational states (Kokoouline and Greene 2005b), which in turn translates into depletion of molecular state population at various rates during the DR process. The inital model calculations suggest a population distribution that predominantly occupies only the lowest approximately 3–10 rotational states. As the goal of the present effort is to achieve the best possible theoretical prediction of the stored molecular ion ensemble population distribution, it is prudent to include the theoretical DR rates of individual states in the model calculations. To account for the state–selective depletion, an additional term is introduced to equation 3.1 that governs the loss rate of specific states $R(J_i)$ due to DR:

$$R(J_i) = \eta_\perp (l_0/C_0) n_e \alpha(J_i), \tag{3.9}$$

where $\eta_\perp = 1$ is the transverse overlap fraction between the electron–ion beams, $l_0 = 0.721\,m$ is the effective merged–beams overlap length throughout the CSR circumference $C_0 = 35.12\,m$, n_e denotes the electron density and $\alpha(J_i)$ corresponds to the theoretical DR rate of a specific rotational state at $\Delta E = 0$ collision energy. The simulations consider the depletion of the lowest four or nine rotational states in the case of H_2D^+ and D_2H^+ respectively.

These DR rates were calculated by Viatcheslav Kokoouline and Chris Greene (Kokoouline and Greene 2023) combining a number of different techniques, namely: multichannel quantum defect theory (MQDT), adiabatic hyperspherical approach

and Siegert pseudostates. An in–depth description of the theoretical methodology is available in (Kokoouline and Greene 2003, 2004, 2005b) and outlined in chapter 2.5.1. The key emphasis of the theoretical approach is geared towards treating rotational excitation of the ion while considering symmetry restrictions that arise from rotational, vibrational and nuclear spin degrees of freedom. It is to be noted, that it might appear contradictory to include the DR theory rates in the model at the present point, as the results of the model calculations will be later used to weigh the individual contributions of each rotational state in order to reproduce the experimentally observed DR rate. However, input from theory must be implored to account for the state–selective depletion and the most reliable theoretical predictions of the electron recombination process of H_2D^+ and D_2H^+ are the ones employed in present work.

A summary of the theoretical calculations can be seen in figure 3.5, which illustrates the state–specific merged–beams rate coefficients as a function of collisional energy. It is notable that the state–specific rate coefficients differ by more than order of magnitude in the low energy part, signifying the importance of individual state contribution to the overall observed DR rate.

Similar estimates regarding the influence of depletion on the population distribution can be performed as in the case for inelastic collisions (for the case of H_2D^+). By plugging in the following numeric values into equation 3.9: $\eta_\perp = 1$, $l_0 = 0.721\,m$, $C_0 = 35.12\,m$, $n_e = 1 \cdot 10^5\,cm^{-3}$ and the rate coefficient for the depletion of the lowest rotational state $\alpha^{mb}(0_{0,0}) = 1.17 \cdot 10^{-7}\,cm^3 s^{-1}$, one arrives at a depletion rate value of $R_{dep} = 2.40 \cdot 10^{-4}\,s^{-1}$. This implies that the state selective depletion has approximately the same influence on the internal population distribution as the inelastic collision process. However, it is important to note that this assessment might not always hold true as theory predicts that some states feature significantly higher (more than an order of magnitude) depletion rates than others.

The inclusion of state–specific depletion completes the model that is used as the main instrument for evaluating the time evolution of the internal population distribution of H_2D^+ and D_2H^+ molecular ions. This model serves as the basis to justify practical decisions regarding the experimental setup (e.g. the measurement scheme) and guides the interpretation of obtained DR rates.

To summarize, the complete model simulates an ion ensemble undergoing radiative relaxation from a set initial Boltzmann distribution in an environment that represents the CSR, while incorporating the following effects: Radiative heating, electron impact inelastic collision process and state-selective DR (of the lowest rotational states), the dominant effect being radiative relaxation. Figure 3.6 visualizes the final iteration of the model calculations including state–selective de-

pletion (dashed lines) compared to a scenario where this effect is excluded (solid lines).

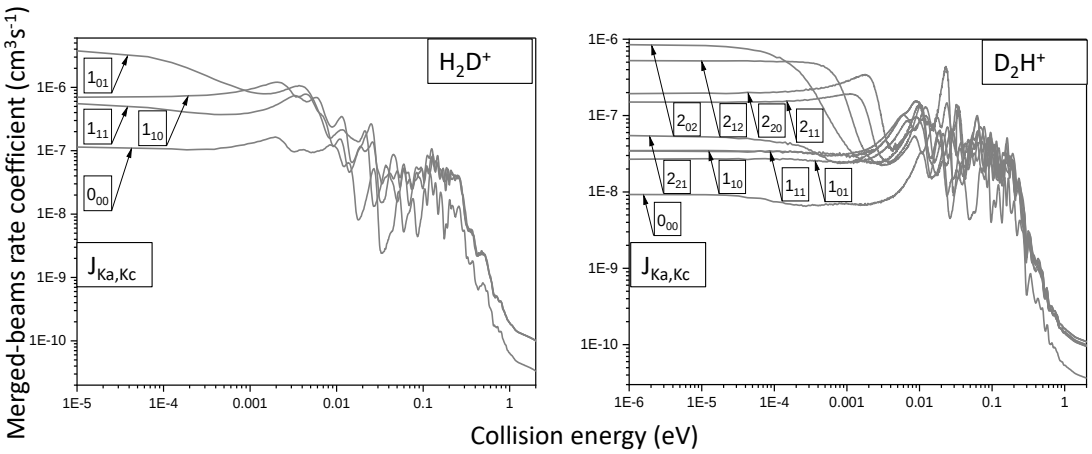

Energy (meV)	Lifetime (s)	J	K_a	K_c	o/p
0.00	Inf	0	0	0	p
5.67	247.52	1	0	1	p
7.44	Inf	1	1	1	o
8.98	8196.70	1	1	0	o
16.32	33.00	2	0	2	p
17.22	53.19	2	1	2	o
21.81	23.00	2	1	1	o

Energy (meV)	Lifetime (s)	J	K_a	K_c	o/p
0	Inf	0	0	0	o
4.33	Inf	1	0	1	p
6.11	302.90	1	1	1	o
7.19	1965.20	1	1	0	p
12.61	483.31	2	0	2	o
13.67	94.41	2	1	2	p
16.91	770.15	2	1	1	o

Figure 3.5: Theoretical DR merged–beams rate coefficients derived by R–matrix calculations for the lowest molecular states of H_2D^+ and D_2H^+ (Kokoouline and Greene 2023). The depicted merged–beams rate coefficients are obtained from calculated cross sections by convolution with the finite collisional energy distribution function of the electron cooler.

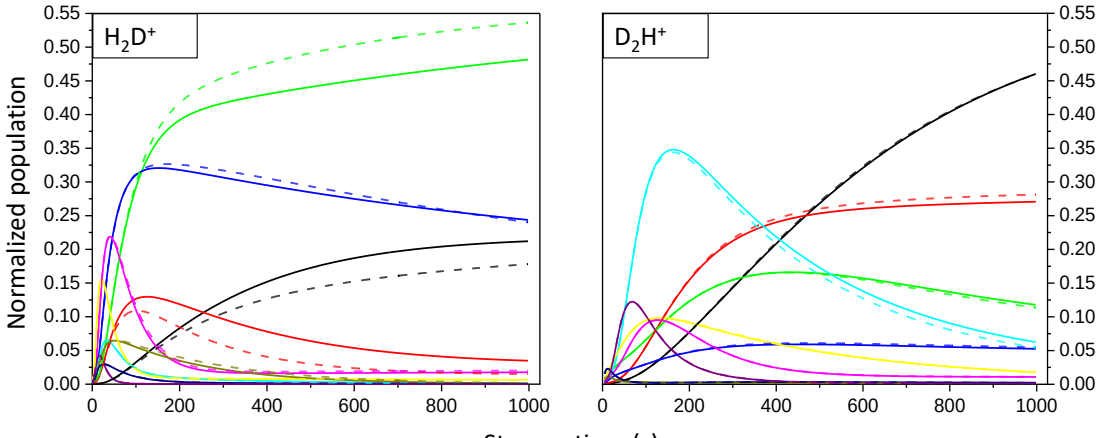

Nr	Energy (meV)	Lifetime (s)	J	K_a	K_c	o/p
1	0.00	Inf	0	0	0	p
2	5.67	247.52	1	0	1	p
3	7.44	Inf	1	1	1	o
4	8.98	8196.70	1	1	0	o
5	16.32	33.00	2	0	2	p
6	17.22	53.19	2	1	2	o
7	21.81	23.00	2	1	1	o

Nr	Energy (meV)	Lifetime (s)	J	K_a	K_c	o/p
1	0	Inf	0	0	0	o
2	4.33	Inf	1	0	1	p
3	6.11	302.90	1	1	1	o
4	7.19	1965.20	1	1	0	p
5	12.61	483.31	2	0	2	o
6	13.67	94.41	2	1	2	p
7	16.91	770.15	2	1	1	o

Figure 3.6: Simulated population distribution as a function of storage time. Solid lines represent a simulation scenario of rovibrational relaxation including radiative heating due to a BBR field and the electron impact excitation and de–excitation rates, while the results indicated by dashed lines incorporate all of the aforementioned effects in addition to state selective population depletion, and thus represent the most comprehensive model of present simulation results.

3.3.5 Internal energy distribution

An alternative manner to present the results of the simulations is illustrated in figure 3.7, which depicts the evolution of the average internal energy of H_2D^+ and D_2H^+ as a function time. As shown in previous plots, the reduction in internal excitation occurs faster for H_2D^+ than D_2H^+ owing to the larger dipole moment and smaller amount of long–lived states with lifetimes $> 100\,s$. Curiously, however, after a simulated storage time of $1000\,s$ D_2H^+ retains a smaller average internal energy, despite the higher number of excited rotational states. The reason for the decreased final internal energy value of D_2H^+ is explained due to the on average slightly smaller rotational spacing among the remaining occupied states. Additionally, the first and following rotational states for D_2H^+ are energetically lower with respect to the absolute ground state than that of the H_2D^+ case. As a consequense, a normalized internal energy distribution follows the behaviour as seen in figure 3.7. The simulation results after $1000\,s$ of storage time represents an ion ensamble that in terms of average internal energy approches conditions of interstellar molecular clouds.

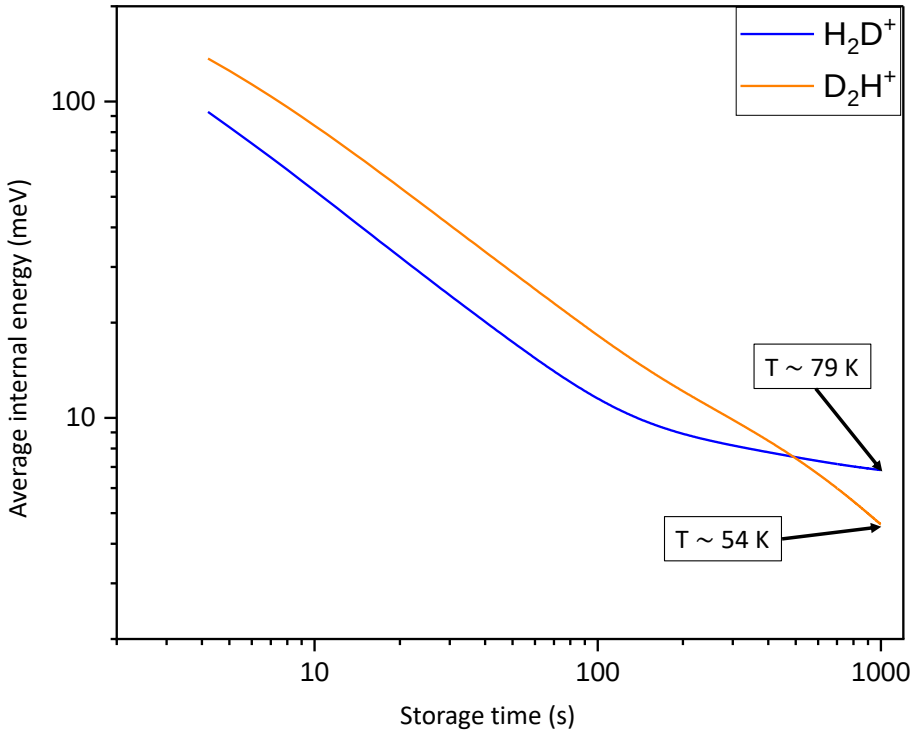

Figure 3.7: Average internal energy of simulated population distribution as a function of storage time.

3.3.6 Extremely long storage times

For completion the simulations where extended to timescales up to 10000 s in order to draw conclusions regarding the equilibrium population distribution and gain insight for future experimental prospects. It is evident that both molecular systems would benefit from extended storage times in terms of achieving a better state definition, see figure 3.8. This statement is especially relevant for D_2H^+, where going from a storage time of 1000 s to 2000 s reduces the relevant number of involved states from $\sim$ six to three. At the time of preparing and performing the DR experiment a D_2H^+ line–list of equivalent quality as in the case of H_2D^+ was not yet available. Therefore, in the present work, the experimentally obtained DR data for both molecules extends up to 1000 s of storage time, with the state definition deemed sufficient based on simulation results for H_2D^+. Beam storage times within the CSR on the order of 1000 s already pose practical difficulties associated with various experimental aspects, which are further exacerbated by time constraints related to the slow data acquisition, necessary to acquire statistically significant results. Detailed explanation of considerations and reasoning regarding the choice of the measurement setup can be found in chapter 4.6.3.

The simulation results described in this chapter demonstrate that storage of H_2D^+ and D_2H^+ molecular ions in the CSR results in a very narrow population distribution after timescales on the order of 1000 s. This in turn paves the road to investigate these systems on the basis of populated quantum states with unprecedented state definition. Future experiments meant to probe the characteristics of individual rotational states, while excluding the influence from the remaining populated molecular levels, necessitates experimental diagnostics that are capable of determining and manipulating the population distribution of the stored molecular ion beam. Theoretical work on such an approach has already been performed (Znotins et al. 2021).

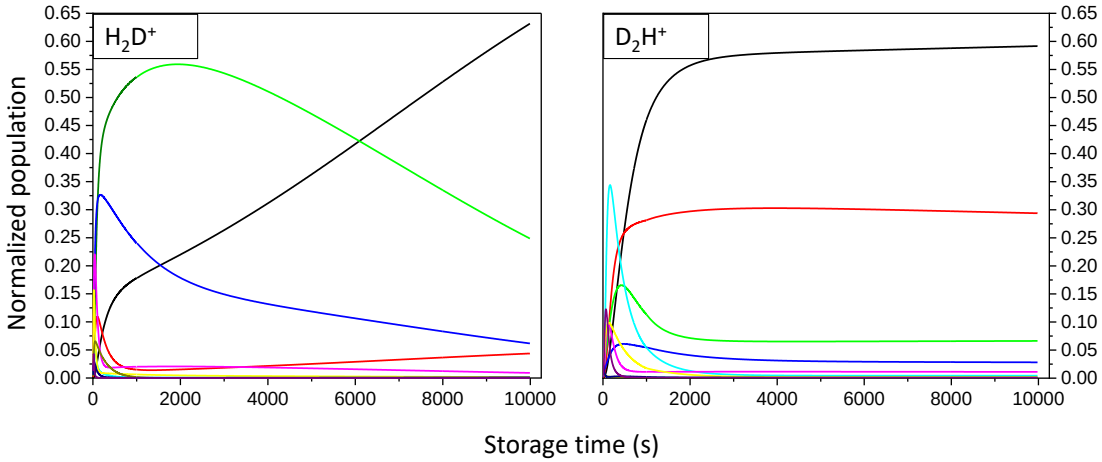

Nr	Energy (meV)	Lifetime (s)	J	K_a	K_c	o/p
1	0.00	Inf	0	0	0	p
2	5.67	247.52	1	0	1	p
3	7.44	Inf	1	1	1	o
4	8.98	8196.70	1	1	0	o
5	16.32	33.00	2	0	2	p
6	17.22	53.19	2	1	2	o
7	21.81	23.00	2	1	1	o

Nr	Energy (meV)	Lifetime (s)	J	K_a	K_c	o/p
1	0	Inf	0	0	0	o
2	4.33	Inf	1	0	1	p
3	6.11	302.90	1	1	1	o
4	7.19	1965.20	1	1	0	p
5	12.61	483.31	2	0	2	o
6	13.67	94.41	2	1	2	p
7	16.91	770.15	2	1	1	o

Figure 3.8: Simulated population distribution as a function of storage time. Solid lines represent a rovibrational relaxation simulation scenario including all of the aforementioned effects as described in figures 3.2, 3.4, 3.6. extended up to a simulated storage time of 10000 s.

Chapter 4

Experimental setup and measurement procedure

4.1 The Cryogenic Storage Ring

The experimental work presented in this thesis was conducted at the Cryogenic Storage Ring (CSR) facility, located at the Max Planck Institute for Nuclear Physics in Heidelberg. Commissioned in 2014, after more than a decade of planning and construction, the CSR represents one of the most successful examples of current generation storage ring devices of its type. The following paragraph will provide a brief overview of basic parameters and capabilities of the storage ring, while an extensive review of the facility's functionality and infrastructure can be found in (von Hahn et al. 2016).

As mentioned in the previous chapter, the CSR relies exclusively on electrostatic ion optics to achieve stable storage of negative or positive ions. This approach avoids restrictions imposed by the use of magnetic bending and focusing elements for beam guiding, permitting storage of charged particles independent of the mass at a given kinetic energy and charge. The CSR was designed to store beams of ions with kinetic energies ranging from 20 to 300 keV per unit charge. Even though electrostatic optics offer a reduced beam energy range compared to magnetic storage rings, they are simpler to use, have smaller fringe fields and any magnetic hysteresis effects are absent.

Figure 4.1: Photograph (by Christian Föhr 2013) of the Cryogenic Storage Ring (CSR) in its assembly phase. The outer walls of the cryostat are yet to be mounted offering a view of the inner experimental vacuum chambers.

A photograph of the CSR in shown in figure 4.1, illustrating the scale of the experiment. With a circumference of 35.12 m, the CSR features a nested structure comprised of an inner vacuum chamber (otherwise denoted as the experimental vacuum chamber), encompassed by the isolation vacuum chamber. A closed–cycle liquid helium system is used to cool down the storage ring to cryogenic temperatures. A commercial cryostat (Linde) delivers liquid helium to the CSR where it is circulated through the cooling circuits. There are four cooling cycles characterized by the nominal temperature of the circulating helium named – 2 K, 5 K, 40 K and 80 K lines respectively. The two colder 2 K and 5 K lines contact the experimental vacuum chamber and internal components via copper blocks and copper stripes. The inner vacuum chambers are surrounded by an aluminium shield, which is referred to as the 40 K shield, followed by another aluminium shield wrapped in superinsulation foil, denoted as the 80 K shield. Both of these insulation layers are attached to their dedicated helium lines. This approach allows for the experimental vacuum chambers to be cooled down to around 4 K and prevents interactions with 300 K black body radiation. Conveniently, at cryogenic

temperatures, the vacuum chambers serve as a large cryopump, enabling residual gas densities of $\leq 10^4\,cm^{-3}$ or $<10^{-13}\,mbar$ room temperature equivalent. These low temperatures and pressures allow for very long particle storage times, up to several thousand seconds. On these timescales, molecules with a permanent dipole moment can radiatively cool down to their absolute rovibrational ground states (Paul 2021, C. Meyer et al. 2017).

In summary, the CSR presents novel prospects for optical and collisional studies with internally cold ions, molecules and even clusters.

4.2 Molecular ion beam production

Various types of ion sources can be utilized to generate beams of either positive or negative ions. For this purpose, the CSR facility is equipped with two different high–voltage platforms capable of housing multiple ion sources. The platforms are referred to by their upper voltage limits – $60\,kV$ and $300\,kV$ respectively. H_2D^+ and D_2H^+ ions employed in the experiments described in this work, were produced by a duoplasmatron ion source mounted at the $300\,kV$ high voltage platform. A target gas is introduced in the ion source volume, where it is ionized by bombardment of electrons emitted by a cathode filament, creating a high–density plasma. Subsequently, the plasma is accelerated towards the exit aperture, becoming an ion beam. In this particular case a mixture of H_2 and HD gas was used to generate the desired beams of H_2D^+ and D_2H^+ ions. The selected kinetic energy of $250\,keV$ was chosen to simplify the electron cooling process, which is further described in section 4.6.2.

After acceleration, the ions are guided towards the CSR via the transfer beamline, a schematic is shown in figure 4.2.

The $300\,kV$ beamline part consists of two 45–degree bending dipole magnets and two electric quadrupole triplets. Together with other beam diagnostics elements, the ion beam can be shaped and monitored, ensuring optimal quality before entering the CSR. The transfer beam line is equipped with parallel plate deflectors (choppers) installed close to the source platform, which are used to define the time structure of the ion beams. This is achieved by fast switching ($\sim$100 ns) of the parallel plate deflector voltages, enabling ions to pass through the beamline only at desired times. For a detailed description of the transfer beam line and ion sources the reader is referred to (Grussie 2016).

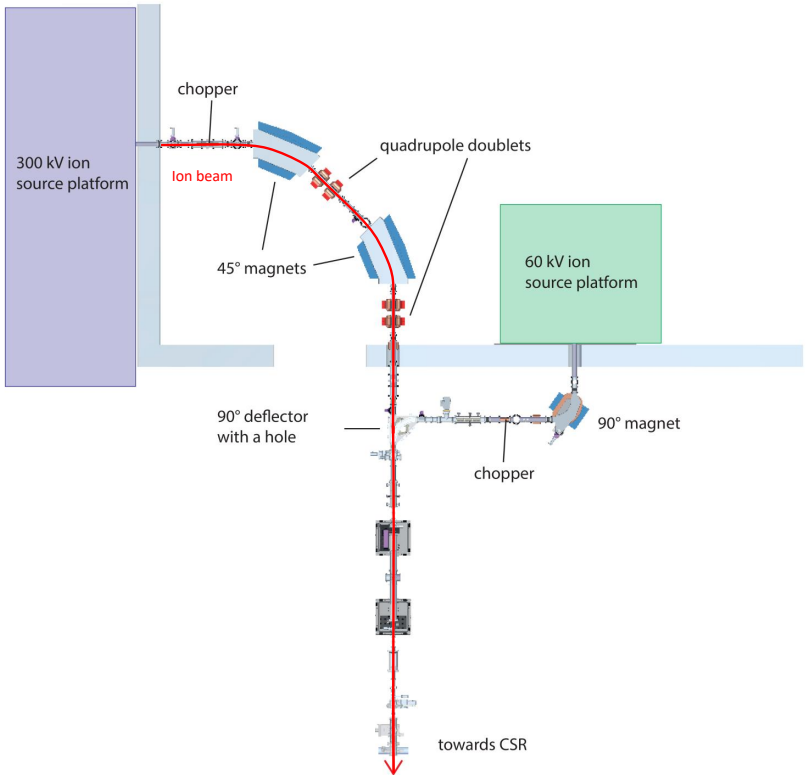

Figure 4.2: Overview of the transfer beamline used to guide the ion beams from the source platforms to the CSR (adapted from Grussie 2016). The schematic outlines the path of the ion beam towards CSR and marks the main beamline elements. The ion source platforms are not fully shown and are depicted representatively. Only the 300 kV platform was utilized in the present work.

4.3 Overview of experimental capabilities

The CSR is a versatile instrument, designed to house a variety of experimental equipment. A schematic view of the storage ring is shown in figure 4.3, defined by the four straight sections. After an ion beam has been produced and guided through the transfer beamline, it enters the storage ring, where a combination of electrostatic deflectors located at each corner confines the beam to a closed orbit. Each 90–degree bend is achieved by two major (39–degree) and two minor (6–degree) cylindrical deflectors. Beam injection is handled by voltage switching of the first minor deflector on timescales shorter than one single revolution of the circulating ion beam. Focusing is realized by two quadruple doublets situated at each of the straight sections, with an approximately 2.6 m field free section in between reserved for experiments.

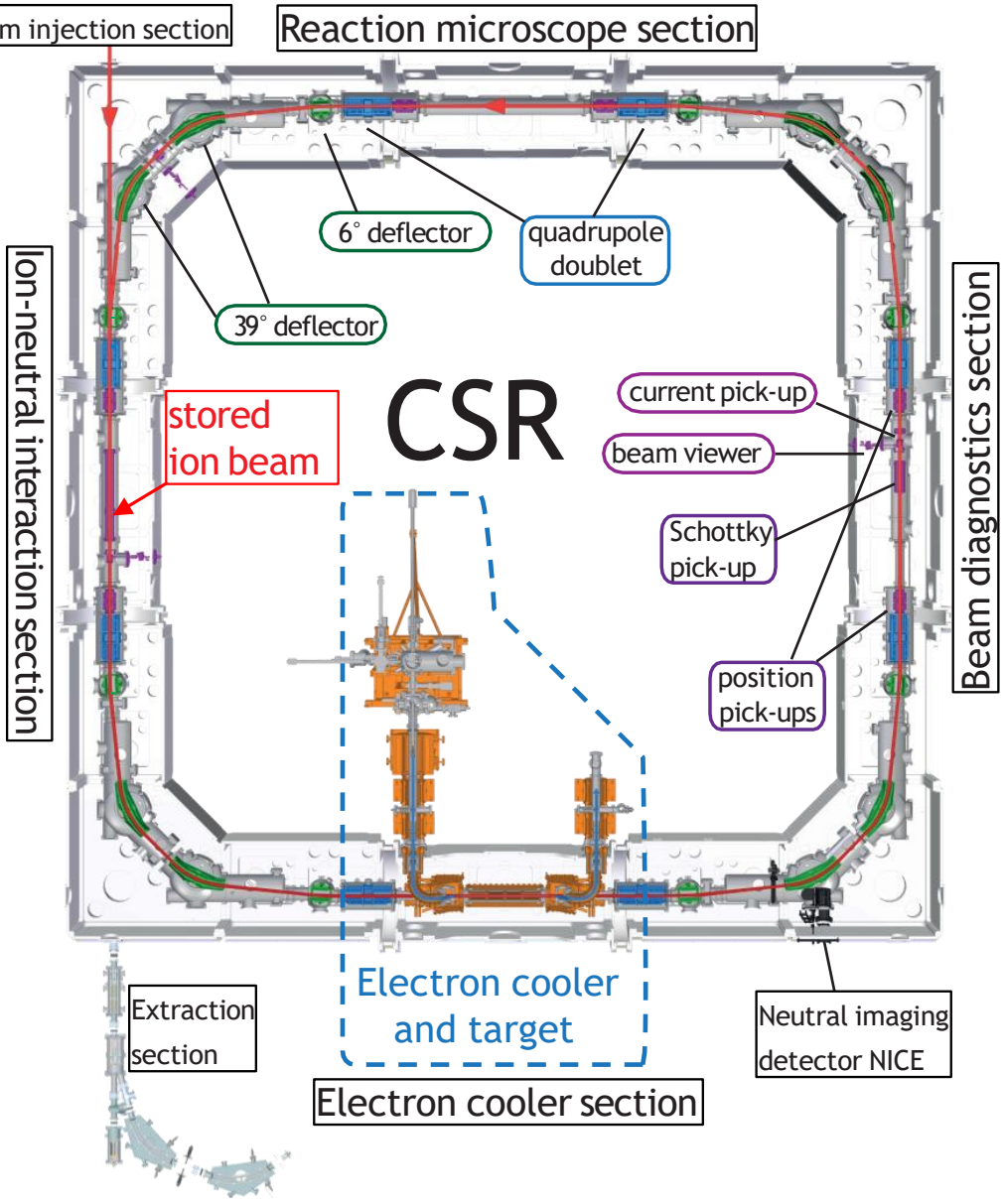

Figure 4.3: Schematic overview of the CSR marked with key beamline elements. The beam injection section is located at the top left corner of the schematic. The injected ions (red) circulate counter clockwise throughout the four main sections of the ring kept on a nominal orbit by a series of electrostatic deflectors (blue and green). The beams of target ions and electrons are overlapped in the electron cooler section (dashed blue), thereafter the neutral reaction fragments exit the nominal orbit and impinge on the NICE detector. Beam diagnostics elements utilized in the present work are marked in purple.

The first section counter–clockwise from the beam injection direction is devoted to measurements of ion–neutral merged beams reactions. Collision product analysis is performed by utilizing movable particle detectors located at the next straight section. Additionally, a dedicated extraction section with its own diagnostics is available for determining the properties of ion and neutral beams. Furthermore, this section features a radiofrequency (RF) system for the purpose of re–bunching the stored ion beam. Beam bunching is achieved by applying an alternating voltage on a drift tube. The necessary RF frequency is determined by a certain harmonic of the circulating ion beam revolution frequency. Although RF bunching results in a reduced beam lifetime, the method offers an enhanced ion detection sensitivity, especially relevant for aiding diagnostics of weak ion beams. More details of the RF system can be found in (von Hahn et al. 2016).

Following the ion–neutral merged beams section, the second straight section contains two experimental setups for investigation of ion–electron and ion–photons reactions. Various types of laser systems covering a broad wavelength range are available at the CSR facility, with the possibility to intersect the stored ion beam at two different overlap geometries. Laser light can be introduced in the experimental vacuum through laser ports via sapphire viewports. Two of the laser pathways offer a crossed beams arrangement, while the third configuration provides a near–colinear ion-laser beam interaction region with a 1.1–degree grazing angle.

In order to study ion–electron reactions, the CSR is equipped with a low energy electron cooler, housed in the same straight section as the laser setup. The electron cooler produces a spatially well–defined beam of electrons with energies as low as $1\,eV$ with a narrow energy distribution. This enables phase space cooling of the stored ions, by decreasing the ion beam size and reducing the velocity spread. Furthermore, the velocity of the electron beam can be finely tuned, which allows the beam to function as a collision target in merged–beams studies. As this part of the CSR setup played a central role in the context of this work, a broader description will be given in paragraph 4.5.

The next straight storage ring section is reserved for beam diagnostics elements, which mainly rely on non–destructive methods to determine properties of the stored beams. A Schottky pickup is available for observation of charge density fluctuations (Laux 2011), which are present even in coasting (debunched) ion beams. Such a signal provides confirmation of particle storage and can serve as a method for determining the lifetime of the ion beam within the CSR. Additionally, the measured energy spread by the Schottky pickup provides an insight into the mass composition of the stored beam, identifying potential contaminants with a different mass, but identical kinetic energy. In order to precisely determine the

absolute ion current and infer the stored ion number, the diagnostic section is also fitted with a capacitive current pickup that detects mirror charge of the circulating particles. Each straight section, apart the one housing the electron cooler, includes a pair of position pickups used to determine the central position of the stored particle beam. A comprehensive explanation of every diagnostic element can be found in (Vogel 2016).

Lastly, the fourth straight section of the CSR is reserved for a reaction microscope setup, which is currently in the last phase of assembly and will be commissioned tentatively in the second half of 2023.

4.4 Particle detectors

As mentioned in prior paragraphs, the CSR is equipped with several microchannel plate (MCP) based particle detector systems. Any collisional experiment will produce either charged or neutral reaction products. The COld Movable PArticle CounTer (COMPACT) detectors are movable single particle counters, suited for detection of charged fragments that diverge from the nominal ion beam orbit. Four iterations of this detector type are located in various places within the CSR, one pair each in the merged beams and electron cooler sections. COMPACT detectors are characterized by a near unity counting efficiency and a low dark count rate ($<0.1\,Hz$), operable in a cryogenic environment. Further technical details of this detector are given in (Spruck et al. 2015).

The electron cooler section is also equipped with an additional detector called NICE (Neutral Imaging in Cold Environment), dedicated for neutral particle detection. Dissociative recombination between electrons and triatomic hydrogen ions produces exclusively neutral fragments, therefore NICE was used for measurements throughout the course of this work. Figure 4.4 depicts a model of the detector, illustrating the working principles. The detector consists of three main components: a MCP stack, phosphor screen and a CMOS camera. Particles that impinge on the detector initiate an electron cascade within the MCP stack. Subsequently, the electrons strike the phosphor screen resulting in photon emission within a time span of few nanoseconds. The phosphor screen needs to be at high voltage in order to effectively collect electrons emitted from the MCP. The impinging electrons generate small electronic pulses on top of the high voltage that is supplied to the phosphorus screen. These pulses are counted by the means of a special signal decoupling circuit described in the work of (Becker 2016).

Photons emitted from the phosphorus screen are reflected by a 90–degree aluminium mirror that directs the light through a viewport towards a fast CMOS camera located outside the experimental vacuum. The purpose of the camera system is to detect light spots that arise from the phosphorus screen providing additional imaging information. The shutter of the camera is triggered by the aforementioned electronic signal.

At cryogenic temperatures of $< 10\,K$, MCPs are characterized by impedance on the order of hundreds of GΩ, inhibiting detection efficiency. To mitigate this effect, active heating of the detector to around $40\,K$ is implemented, reducing the impedance to the 100 MΩ region. In these conditions, a count rate of up to $5\,kHz$ can be realized without adverse saturation effects. Compared to COMPACT detectors, the NICE design has a larger active MCP area, resulting in a dark count rate of $\sim 50\,Hz$. To avoid an excessive particle flux, the NICE detector features a mechanical shutter. Furthermore, a calibration mask – an aluminium plate consisting of a pattern of evenly spaced $10\,mm$ holes – can be utilized to calibrate the distance between the impinging particles.

Further details of the NICE detector ranging from design to commissioning at the CSR are explained in (Becker 2016).

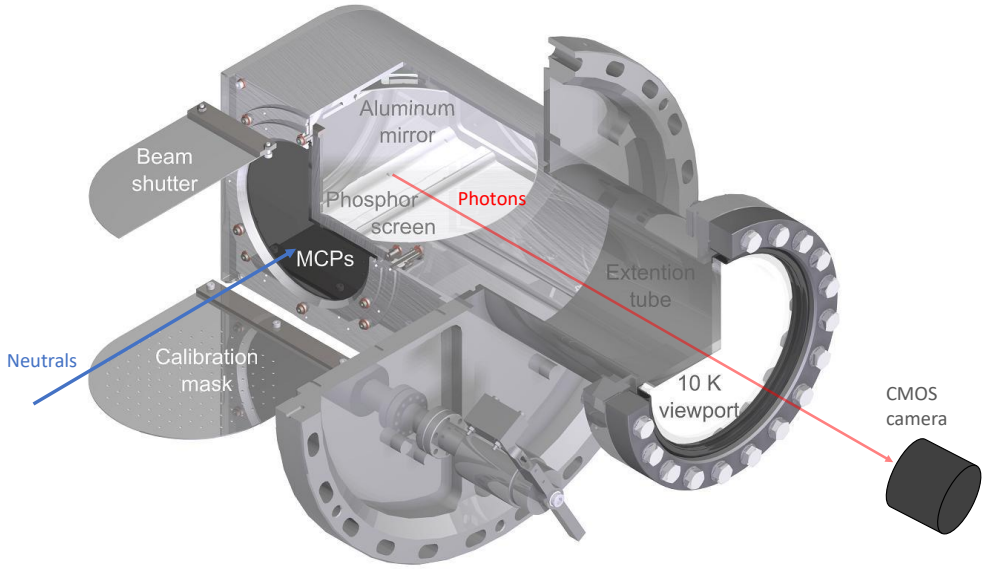

Figure 4.4: Model of the NICE detector illlustrating its key features and working principle (adapted from Paul 2021). Incoming neutral particles induce an electron cascade that impinges on the phosphorus screen. The emitted photons are detected by a CMOS camera.

4.5 The electron cooler

The CSR is the only example in the world that features an electron cooler imbedded in a cryogenic, electrostatic storage ring. For the majority of experiments the electron cooler serves a dual purpose. Firstly, it can be operated as a low–energy phase–space electron cooling device with electron energies as low as $1\,eV$. Secondly, the energy of the electron beam can be finely tuned enabling various ion–electron collisional studies, such as energy resolved dissociative recombination. This paragraph briefly discuses the working principles of the electron cooler and its use as a source of a target of cold–electrons within the merged–beams experimental approach.

A schematic overview of the CSR electron cooler can bee seen in figure 4.5. The electrons are created from a GaAs photocathode. Compared to thermocathodes, photocathodes produce electron beams that are characterized by a narrower energy spread (Orlov et al. 2005; Pastuszka et al. 2000). Located at the so–called photoelectron gun section of the setup, the GaAs photocathode features a monolayer of caesium and oxygen that together with the semiconductor creates a composite surface layer with the property of Negative Electron Affinity (NEA). In essence, NEA is achieved when the conduction band of the doped semiconductor is shifted above the vacuum level due to the properties of the applied monolayers (Spicer 1977). This leads to a significantly increased yield of the electrons generated by the photoelectric effect. Depending on the surface properties of the photocathode, a quantum efficiency of ≈ 8–$12\,\%$ is achieved by utilizing an infrared diode laser at $\lambda = 805\,nm$ and $500\,mW$ of output power. Further information regarding the development of the photocathodes used in TSR and CSR can be found in the work of (Weigel 2003) and (Krantz 2009).

After production, the electrons are extracted and the beam is shaped by a series of electrodes. Additionally, a barrier electrode in the form of a drift tube with a slightly positive potential with respect to ground is employed with the purpose of supressing ions that originate from residual gas ionization. Thereafter, the electrons are guided from the room temperature part towards the cryogenic section and through the ion–electron interaction zone by solenoid and dipole fields as illustrated in figure 4.5. The first guiding solenoid magnet that surrounds the photoelectron gun setup is operated at $3000\,G$, followed by three smaller solenoids producing a magnetic field of $200\,G$. While passing through this area, the electron beam undergoes adiabatic magnetic expansion, which is a common technique that achieves a decreased electron beam transverse temperature at the expense of reduced beam density. At its core, the adiabatic magnetic expansion is governed by the ratio between the initial and final magnetic field values B_i/B_f:

$$\alpha = \frac{B_i}{B_f}, \tag{4.1}$$

where the expansion factor α correlates to the initial and final transverse temperatures $T_{\perp i}$ and $T_{\perp f}$ by :

$$T_{\perp f} = \frac{T_{\perp i}}{\alpha}. \tag{4.2}$$

Additionally, following the invariant $R^2 B = const$, the increase of the beam radius can be expressed as:

$$R_f = \sqrt{\alpha} R_i. \tag{4.3}$$

For a thorough description of the adiabatic magnetic expansion process and its use in electron coolers, the reader is referred to (Pastuszka et al. 1996).

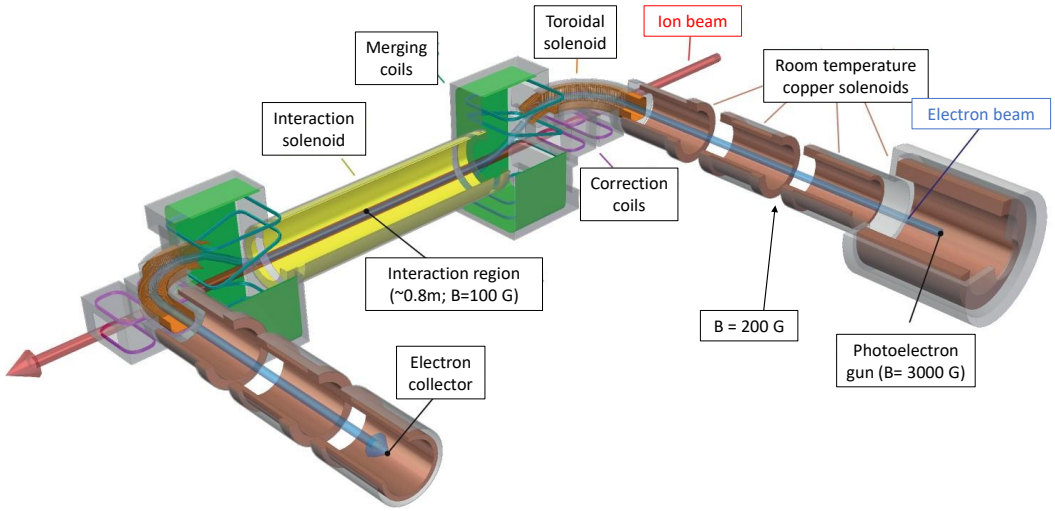

Figure 4.5: Schematic of the CSR electron cooler (adapted from Vogel 2016). The ion beam (red) and electron beam (blue) are merged within the interaction region.

Following the first expansion region, the electron beam enters the CSR with a trajectory slightly above the stored ion beam plane. The toroidal solenoid then performs a 90–degree bend of the electron beam, which in tandem with the merging coils that provide a dipole–like field to account for the 30–degree incline of the electrons, diverts the electron beam towards the merged–beams section. While entering the merged–beams interaction section, the electron beam undergoes a second expansion stage where the guiding magnetic fields change from $B_i = 200\,G$ to $B_f = 100\,G$. At this section the electron beam is characterized by its lowest

temperature – transversely $T_\perp = 2\text{–}3\,meV$ and longitudinally $T_\parallel = 0.3\text{–}0.5\,meV$ at an electron density of $n_e \approx 1 \cdot 10^5\,cm^{-3}$ (for the present experiment). Subsequently, the electron beam is de–merged from the interaction zone and propagates towards the electron collector, guided by a series of solenoids that are layed out in a mirror configuration with respect to the in–coupling part of the setup. In order to account for unwanted drifts and to steer the position of the electron beam, the electron cooler features seven pairs of steering coils located at various positions throughout the setup that enable beam position adjustment in both vertical and horizontal directions.

The CSR electron cooler setup was partly inherited from the TSR after its decommission in 2012. An in–depth description of the design adaptations that resulted in the transfer of an improved electron cooler setup into the CSR can be found in the work of (Shornikov 2012). Details regarding the construction phase and technical aspects are discussed in (Vogel 2016), while the assembly and initial commissioning of the complete system is reported in (Wilhelm 2019).

4.6 DR measurement principles at the CSR merged–beams setup

The following chapter outlines the principles of dissociative recombination measurements and the practical realization at CSR. The relevant definitions and properties of the stored ion beam are introduced followed by the fundamentals of electron cooling at CSR. Lastly, the use of the electron cooler as a collision target in a merged–beams setup for DR measurements is discussed.

4.6.1 Ion beam properties

A stored ion beam within the CSR follows the trajectory of a closed orbit at a certain revolution frequency defined by fields of electrostatic elements. While propagating throughout the CSR, the ions exhibit movement around the closed orbit denoted as betatron oscillations. Furthermore, the circulating ions slightly fluctuate around the central revolution frequency due to a process denoted as synchrotron oscillations. Figure 4.6 portrays a simplified representation of the movement of a particle along a closed ideal orbit influenced by betatron oscillations $\beta(s)$. Such motion $u(s)$ is governed by the solutions of the Hill's equations (Wiedemann 2015):

$$x(s) = A_x\sqrt{\beta_x(s)}cos(\Psi_x(s) + \Psi_{x_0}) \tag{4.4}$$

$$y(s) = A_y\sqrt{\beta_y(s)}cos(\Psi_y(s) + \Psi_{y_0}), \tag{4.5}$$

or simplified:

$$u(s) = A\sqrt{\beta(s)}cos(\Psi(s) + \Psi_0), \tag{4.6}$$

where $A_{x,y}$ is the oscillation amplitude, $\beta_{x,y}$ correspond to betatron functions and Ψ_{x_0,y_0} represents the starting phase of a particle.

In order to characterize the size of an ion beam propagating around a closed orbit, the accelerator community uses the concept of beam emittance ϵ, which can be visualized by the help of an ellipse in phase space (u, u') (see figure 4.6) defined by equation:

$$\gamma(s)u(s)^2 + 2\alpha(s)u(s)u'(s) + \beta(s)u'(s)^2 = a^2 = \epsilon, \tag{4.7}$$

where functions $\alpha(s)$ and $\gamma(s)$ are defined as:

$$\alpha(s) = -\frac{1}{2}\beta'(s) \tag{4.8}$$

$$\gamma(s) = -\frac{1 + \alpha^2(2)}{\beta(s)} \tag{4.9}$$

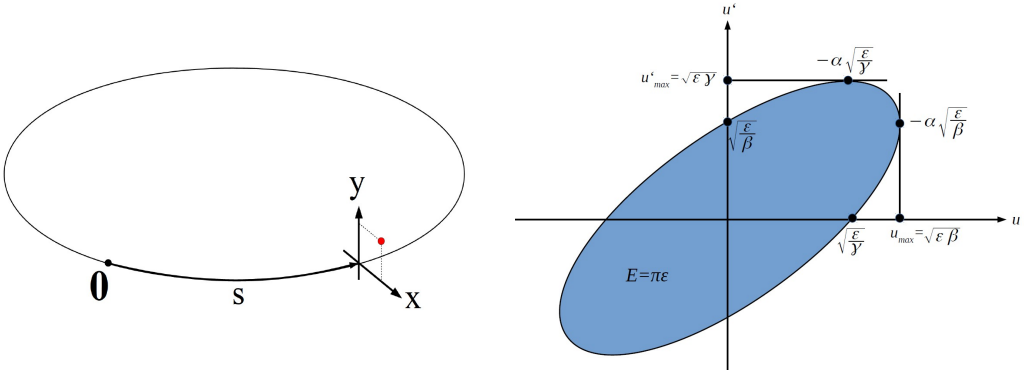

Figure 4.6: Representation of a particle that follows an ideal closed orbit trajectory (left). The ion beam emittance depicted as a phase space ellipse (right). Figures adapted from (Wiedemann 2015).

More specifically, ϵ defines the single–particle emittance, that is correlated to the area of the ellipse and the beam emittance $\pi\epsilon$ via the invariant:

$$E = \pi a^2 = \pi\epsilon = const \tag{4.10}$$

There are various nomenclatures and conventions pertaining to the characterization of beam emittance $\pi\epsilon$. In present work, the phase space area occupied by the stored ion beam shall be defined as:

$$1\sigma = \sqrt{\epsilon^{1\sigma}\beta(s)}; \quad 2\sigma = \sqrt{\epsilon^{2\sigma}\beta(s)}; \quad 3\sigma = \sqrt{\epsilon^{3\sigma}\beta(s)}, \tag{4.11}$$

otherwise denoted as $\epsilon_{1\sigma}$ ($\approx$68 %), $\epsilon_{2\sigma}$ ($\approx$95 %), $\epsilon_{3\sigma}$ ($\approx$99 %) with an additional, often used value of ϵ_{90} ($\approx$90 %). The maximal accommodated emittance of a particular storage device is defined as the acceptance:

$$A = \pi\epsilon_{max} \tag{4.12}$$

Equations and terminology discussed in this paragraph were adapted from (Wiedemann 2015), further information and references cited therein.

4.6.2 Electron cooling

The idea of superimposing a velocity matched beam of electrons with a beam of charged particles in order to supress betatron and synchrotron oscillations in a storage ring environment is credited to (Budker 1967). Thus, the field of electron cooling was born with the first practical implementation realized for a beam of protons (Budker et al. 1976).

The basic idea of electron cooling is portrayed in figure 4.7, which illustrates a velocity matched electron beam interacting with a stored ion beam. At matched averaged velocities in a co–moving frame of reference (common centre of mass), the relevant difference between the ion and electron energy spreads is governed by thermal energy distribution of the ion and electron beams. As ions are typically characterized by a significantly higher temperature compared to the electrons due to the manner in which they are created within an ion source, the interactions driven by Coulomb collisions tend to decrease the momentum spread of the ion beam. The underlying principle of electron cooling relies on the removal of excess energy that gets transferred in the collisional process from the "hot" ions to the constantly replenished "cold" electrons at every revolution cycle. To apply electron cooling within the CSR, the matched beam velocities condition must be met, requiring electrons to be at a certain energy E_{cool} in the laboratory frame of reference:

$$E_{cool} = \frac{m_e}{m_{ion}} E_{ion} = \frac{m_e f_{rev}^2 C_0^2}{2}, \tag{4.13}$$

where m_e and m_{ion} are the mass of electron and ion, f_{rev} is the revolution frequency of the stored ion beam and C_0 is the circumference of CSR. At small

velocity deviations among the two beams, the ion beam experiences a friction force that leads to deceleration or acceleration, until ultimately both beams end up with matching average velocities, in a process called dragging. When implemented successfully, electron cooling dampens synchrotron and betatron oscillations of the stored ion beam resulting in a compressed ion beam with a reduced emittance and momentum spread that enables high resolution experiments in a merged–beams configuration. Furthermore, in most cases within the CSR, an electron cooled beam is characterized by an extended beam life time compared to an uncooled beam, while electron cooling counteracts detrimental heating effects that tend to limit beam storage.

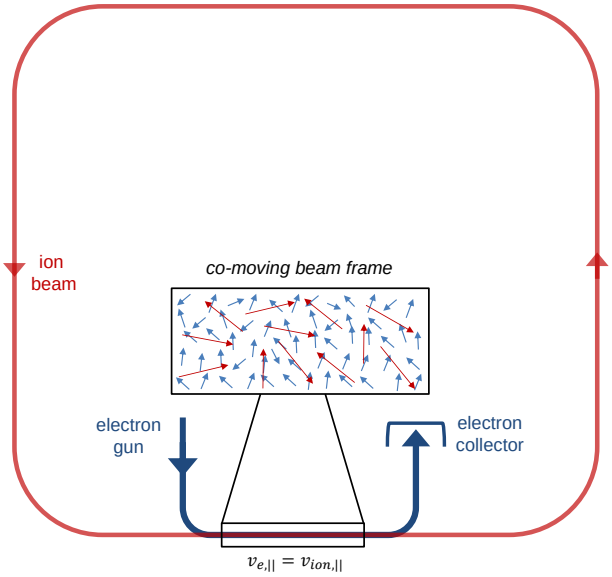

Figure 4.7: Concept of electron cooling. The circulating ion beam (red) is merged with a velocity matched beam of electrons (blue). Collisional interactions within the co–moving frame of reference result in an ion beam of reduced internal energy distribution. Figure from (Wilhelm 2019).

4.6.3 DR measurement principle

To investigate the dissociative recombination reaction between electrons and H_2D^+ and D_2H^+ molecular ions, the electron cooler is operated in the collision target mode. In this regime the energy of the interacting electrons is varied from the energy value E_{cool} defined by the matched beams velocities condition (equation 4.13) to non–zero collision energy values denoted as E_{lab}.

During present measurements, prior to measuring the reaction of interest, the

electron cooler is operated in the cooling mode for a period of 200 – 1000 s to achieve the best possible internal state definition in accordance to the simulations described in the previous chapter. In an ideal scenario this results in an ion beam with the average velocity and energy defined by:

$$\langle v_{ion} \rangle = \sqrt{\frac{2E_{cool}}{m_e}} = \sqrt{\frac{2E_{ion}}{m_{ion}}} \tag{4.14}$$

A collision between an ion with energy E_{cool} and an electron from a perfectly aligned ion–electron merged beam setup with energy E_{lab}, from the perspective of the ion center of mass, is described by the collisional energy E_{CM} (Larsson 2005):

$$E_{\mathrm{CM}} = m_{\mathrm{e}} \left[\sqrt{\frac{E_{\mathrm{lab}}}{m_{\mathrm{e}}}} - \sqrt{\frac{E_{\mathrm{cool}}}{m_{\mathrm{e}}}} \right]^2 = \left(\sqrt{E_{\mathrm{lab}}} - \sqrt{E_{\mathrm{cool}}} \right)^2 = E_{\mathrm{d}}, \tag{4.15}$$

where E_d denotes the so called detuning energy or relative collision energy.

Figure 4.8 depicts the main principle of the dissociative recombination measurements in a merged–beams setup at CSR. The stored ions are overlapped by the electron beam within one of the straight sections defined by an overlap length of $\approx 80\,cm$. After the DR process takes place, the reaction fragments exit the closed storage ring orbit and are counted by the NICE detector. In this manner, high resolution DR spectra are obtained by adjusting the detuning energy E_d. Further details regarding the experimental process follows in the subsequent chapter.

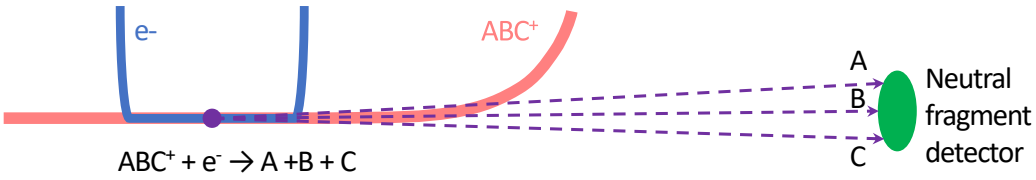

Figure 4.8: Schematic of a merged–beams experimental setup. A triatomic cation fragments into three neutral particles after a DR reaction with an electron. The figure depicts only one of several fragmentation channels.

4.7 Ion beam characterization

A thorough characterization of the ion beam properties is essential to achieve a well–defined ion-electron merged beams configuration within the CSR. The following paragraph lays out the main definitions, concepts and measurement procedures associated with ion production and storage within the ring.

4.7.1 Storage of H_2D^+ and D_2H^+ at the CSR

As mentioned in previous chapters, the H_2D^+ and D_2H^+ molecular ions employed in the present experimental work were produced in a duoplasmatron ion source located at the $300\,kV$ high voltage ion source platform (figure 4.2). The mass variety and intensity of ion beams that can be generated by a duoplasmatron ion source is mainly determined by the input gas and the sampling region of the plasma jet. In order to produce H_2D^+ and D_2H^+ ions the source was operated with a mixture of HD and H_2 gasses. To separate and select the molecular ion with the desired mass, the CSR injection beamline is equipped with an analyser magnet. The ions are accelerated to a kinetic energy of $250\,keV$ and guided towards the CSR after filtering of the relevant mass, namely $4\,u$ or $5\,u$ in current experiments. Before entering the CSR, the continuous ion beam propagating through the injection beamline is pulsed by one of the electrostatic deflectors (chopper). Thereafter, the voltage of the first 6–degree deflector is lowered, permitting the ions to enter the ring. The injection cycle of the ions is defined by the timing of the voltage switching of the chopper and the first 6–degree deflector. Around $4\,\mu A$ of current was measured at a Faraday cup located directly before the entrance of the CSR. Such an ion current is sufficient to fill the storage rings acceptance and corresponds to a stored particle count of roughly few times 10^8 per each injection.

Whence parameters of the ion source and injection beamline that correspond to satisfactory beam currents have been established, suitable settings of the CSR guiding fields must be implemented to achieve optimal beam storage. The optical lattice that determines the closed orbit at the CSR is realized by electrostatic fields that originate from 4 cylindrical deflectors per corner and several quadrupole doublets throughout the ring (see figure 4.3). As discussed in the previous chapter the stored ion beam undergoes oscillations around the closed orbit. The betatron movement of the ions introduces constrictions on the applied guiding field values, which can be explained by the concept of tune values $Q_{x,y}$ defined as the number of betatron oscillations of the stored ion in one revolution of the CSR:

$$Q_{x,y} = \frac{1}{2\pi} \int_s^{s+C_0} \beta_{x,y}^{-1} ds \tag{4.16}$$

If the solution of this equation results in an integer value i then it leads to a lattice condition where the stored ion returns to the same position after i number of revolutions. As a consequence of this condition, the ions experience a guiding field value that amplifies the betatron movement, eventually resulting in a situation where the particle leaves the storage rings acceptance. To avoid incompatible ion beam storage settings, the use of the tune diagram is employed as seen in figure 4.9. The straight lines of the tune diagram mark the respective tune values Q_x, Q_y at which undesirable resonance conditions are met:

$$n = i \cdot Q_x; \quad n = i \cdot Q_y; \quad n = j \cdot Q_x + k \cdot Q_y, \quad m = |j| + |k|\,, \tag{4.17}$$

where j, k, and n represent integer numbers.

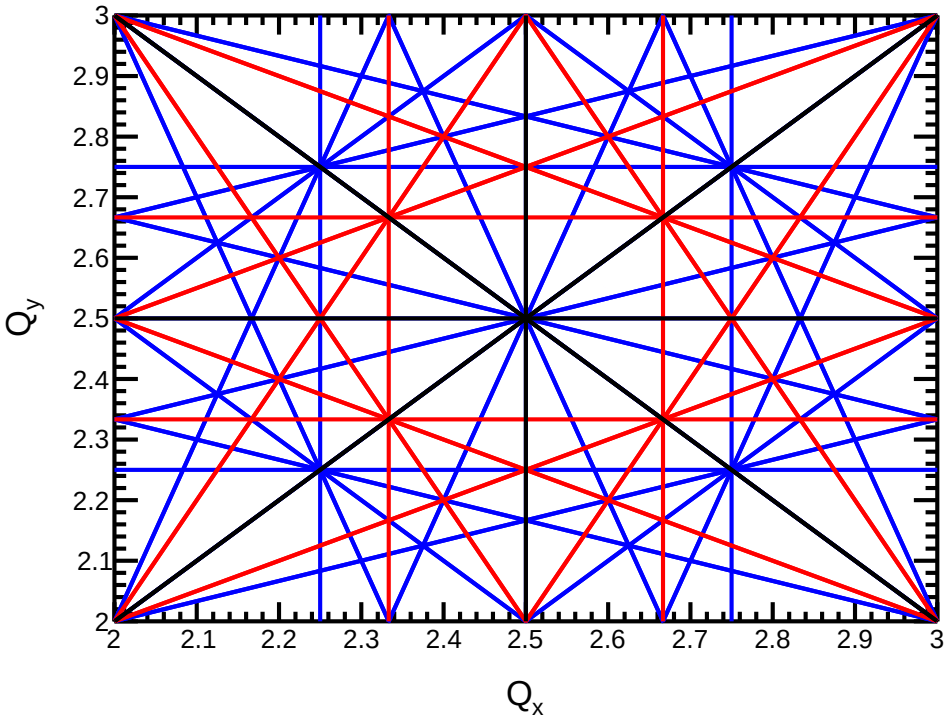

Figure 4.9: Tune diagram example of the CSR. The first order resonances coincide with the x–axis and y–axis, respectively, while the second order resonance lines are marked in black. The red lines correspond to third order resonances, whereas the blue lines depict the fourth order resonances. A typical working point value is $Q_{x,y} \approx 2.5$–2.7 (avoiding resonances), which depends on the molecular system and storage mode.

A favourable, resonance free spot of the tune diagram for stable ion storage

called the working point is selected by adjusting the settings of the quadrupole doublets. For the present case of storing H_2D^+ and D_2H^+ ions, the quadrupole field values were set up to be symmetrical throughout all straight sections of the ring in a configuration referred to as standard mode. An extended discussion regarding the appropriate choice of the working point and its influence on ion beam storage can be found in (Wilhelm 2019).

4.7.2 Radio frequency ion beam bunching

Once the beamline settings of the CSR have been optimized, the characteristics of the ions beam can be further investigated and adjusted. Typically, the initial adjustments of the ion beam are performed with a bunched beam in order to alleviate difficulties associated with the detection of a weaker coasting beam. A coasting beam is transformed to a bunched beam via the process of radio frequency bunching, where the circulating ion beam experiences a time dependant acceleration voltage while passing through a drift tube within the CSR. The basic principle of RF bunching is illustrated in figure 4.10, where the energy gain of a particle that passes a region with a certain RF voltage frequency and amplitude is depicted. The necessary RF frequency required to achieve a bunched beam is governed by:

$$\omega_{rf} = n\omega_0, \tag{4.18}$$

where n is an integer and

$$\omega_0 = 2\pi f_0 \tag{4.19}$$

is the revolution frequency of the stored ion, which for the case of H_2D^+ was determined to be $f_0 = 98.5121\,kHz$ and for D_2H^+ $f_0 = 88.0260\,kHz$.

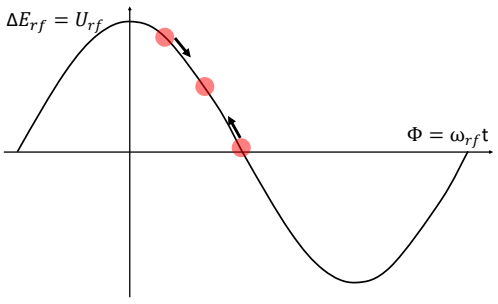

Figure 4.10: Radio frequency ion beam bunching. The energy gain or decrease ΔE_{rf} per revolution of a particle that passes through a drift tube with an applied rf voltage as a function of the radio frequency phase Φ.

At resonance conditions the particle experiences an energy gain or decrease ΔE_{rf}, while propagating through a drift tube of length L:

$$\Delta E_{rf} = Ze\hat{U}_{rf}[cos(\Phi - \omega_{rf}t_f) - cos(\Phi + \omega_{rf}t_f)], \tag{4.20}$$

where Z corresponds to the atomic number of the ion, e is the charge of the electron, Φ denotes the phase of the rf voltage and $t_f = L/v_0$ refers to the time that the particle spends within the drift tube. The necessary RF voltage is determined by:

$$U_{rf}(t) = -\hat{U}_{rf}cos(\Phi); \quad \Phi = \omega_{rf}t \tag{4.21}$$

The formulas and concepts depicted in this paragraph are adapted from (Tecker 2020), where an extended description of RF bunching derived from basic principles can be found.

4.7.3 Ion beam diagnostics systems

The monitoring of the stored ion beam properties at CSR relies on the use of three capacitive pick–up systems: the Schottky pick–up, beam current pick–up and six position pick–ups located at various spots at the storage ring, see figure 4.3. The fundamental working principle of these pickups are in essence the same and are based on capacitive detection of the mirror charge induced by the circulating ion beam. The design and characteristics of these systems are described at great length in the work of (Vogel 2016) and (Wilhelm 2019). Therefore, only the core working principles of these systems and their use in the context of the present work shall be outlined briefly.

A schematic that depicts the detection of induced mirror charge of an ion beam passing a pickup electrode is shown in figure 4.11. As the ion beam advances across the hollow tube pickup electrode, the in and outgoing currents $I_{in}(t)$, I_{out} and the currents $I_C(t)$, $I_R(t)$ toward the grounded experimental chamber that are generated by the mirror charge follow Kirchhoff's junction rule:

$$I_{in}(t) - I_{out}(t) = I_R(t) + I_C(t) = I(t_0) - I(t_0 - \Delta t)) \approx I(t)\Delta t. \tag{4.22}$$

By using the relations $\Delta t = L_0/v$, $I_R(t) = U_R(t)/R$ and $I_C(t) = CU_C(t)$ equation 4.22 can be re–written as:

$$I(t)\frac{L_0}{v} = \frac{U_R(t)}{R} + CU_C(t). \tag{4.23}$$

Due to a combination of high resistance of amplifiers used within the setup ($R \approx 5\,M\,\Omega$) and the pick-up capacity of $C \approx 100\,pF$, it can be assumed that $C \gg 1/R$ and therefore:

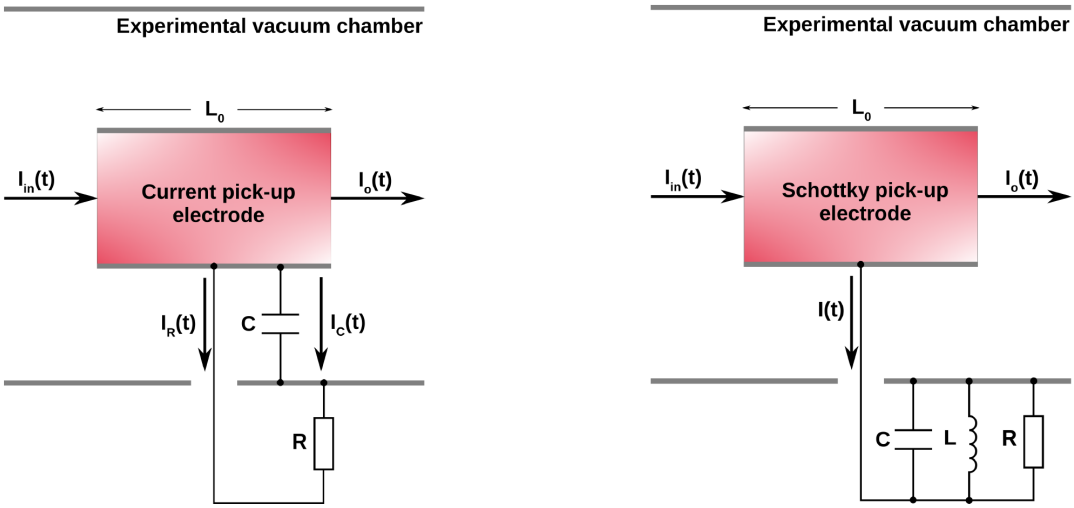

Figure 4.11: The working principle of current pick–up and Schottky pick–up electrodes. The circulating ion beam induces a mirror charge in the capacitive circuit that is used to determine properties of the ion beam. Figure from (Wilhelm 2019).

$$I(t)\frac{L_0}{v} = CU_C(t). \tag{4.24}$$

As the measurement chain includes an amplifier with an amplification factor G the relation between the measured voltage $U(t)$ and the stored ion current $I(t)$ becomes:

$$I(t)\frac{L_0}{v} = \frac{1}{G}CU(t). \tag{4.25}$$

The absolute number of ions within a bunched pulse can be determined by integrating the measured signal $U(t)$, the procedure is explained in section 4.10.4.

The other pickups function in a similar manner with the specifics described in detail in (Vogel 2016). In summary, the present work employs the various pickup beam diagnostics systems available at CSR in several ways:

- the current pickup was utilized to determine the absolute number of ions within the CSR,
- the Schottky pickup was used to investigate the evolution of the momentum spread of the stored beam and infer the effects of electron cooling,
- the beam position monitors, as the name suggests, served to assist beam alignment and optimize storage settings accordingly.

4.7.4 Isochronous mode

As the duoplasmatron ion source was operated with a mixture of H_2 and HD gas, mass $4\,u$ output can in principle consist of 2 isobars, namely H_2D^+ and D_2^+ with molecular weights of $m_{H_2D^+} = 4.02943\,u$ and $m_{D_2^+} = 4.02766\,u$ (Linstrom and Mallard 2023). The potential contamination of D_2^+ within the H_2D^+ beam may contribute to the observed DR rate. Therefore, to eliminate the ambiguity of the ion beam composition, the contribution of the isobaric constituents need to be established. For this purpose the CSR is operated in the isochronous mode, in which the storage ring fulfils the functions of a time-of-Flight (ToF) mass spectrometer. The basic principle of ToF mass spectroscopy relies on the differences in flight time T, T_0 among dissimilar mass particles m, m_0 propagating through a storage medium:

$$\frac{T}{T_0} = \sqrt{\frac{m}{m_0}}. \tag{4.26}$$

Increasing the distance travelled enhances the mass resolution $\Delta m/m$ that can be achieved, which ultimately is limited by the stored particle energy spread. In isochronous operation mode the ring lattice is setup in a configuration that results in ion beam paths separating into different orbits, due to the non–identical kinetic energies of the different mass ions. As a consequence, the flight time difference of the circulating ions become dependant exclusively on the masses of the ions. A comprehensive overview of the necessary ring conditions and practical implication is described in a recent publication (Grieser et al. 2022), where the general relationship between flight time and mass-to-charge ratio difference at CSR is derived as:

$$\frac{\Delta T_n}{T_n} = \frac{1}{2}\frac{\Delta m/q}{m/q}, \tag{4.27}$$

after n revolution cycles, $\Delta T_n = n\Delta T$. Therefore, the revolution time ratio between H_2D^+ and D_2^+ ions that have near identical mass-to-charge can be expressed as:

$$\frac{T_{H_2D^+}}{T_{D_2^+}} = \sqrt{\frac{m_{H_2D^+}}{m_{D_2^+}}}. \tag{4.28}$$

By replacing the revolution time with the more practically relevant revolution frequency $f = 1/T$, the ratio becomes

$$\frac{f_{H_2D^+}}{f_{D_2^+}} = \sqrt{\frac{m_{D_2^+}}{m_{H_2D^+}}}. \tag{4.29}$$

In practice, one way to distinguish between similar mass contributions within the stored beam is to use the isochronous mode in tandem with the current pick–up

to obtain the induced current signal as a function of the revolution frequency. In the present case, such an measurement was used to determine the degree of contamination of D_2^+ within the H_2D^+ beam and adjust the source settings to suppress said unwanted contaminant. The isochronous mode offers a mass resolution of up to $\Delta m/m \approx 1 \cdot 10^{-5}$, which is sufficient to confidently identify the relative fraction of D_2^+ within the H_2D^+ ion beam. Two measurement results with various duoplasmatron ion source settings are shown in figure 4.13. Production of H_2D^+ using only HD gas results in a beam dominated by D_2^+ ions. However, when the source is operated with a 4:1 mixture of H_2 and HD gas, the output is characterized by a very small fraction ($\sim 0.03\%$) of D_2^+ contamination. Consequently, the latter settings were used throughout the DR measurement beamtime.

The production of an D_2H^+ ion beam was significantly simpler in comparison due to the lack of isotopologues with similar molecular weight at $5\,u$ that would influence the observed DR signal. The analyser magnets are sufficient to isolate the desired ion and divert any impurities of different mass origin.

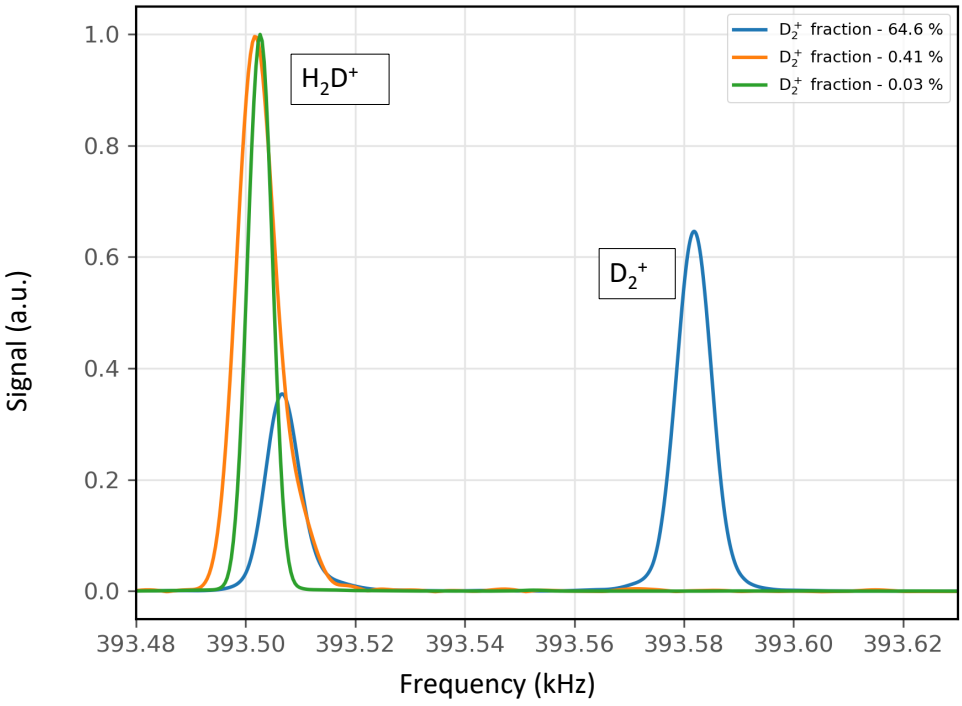

Figure 4.12: D_2^+ contamination measurements at various ions source settings using the isochronous mode. By adjusting the mixture of H_2 and HD gas various ion source output regimes can be achieved.

4.7.5 Ion beam lifetime measurements

An important metric that describes the quality of the storage conditions is the ion beam lifetime. As mentioned before in previous sections, the CSR is a cryogenic storage ring characterized by a residual gas density on the order of $\approx$ 1000 particles per cm^3 when in cryogenic operation mode. Under optimized beam storage conditions, the main limiting factor of ion beam storage are losses attributed to the beam guiding elements, namely the focusing quadrupoles and electrostatic deflectors. A much smaller, but not insignificant contribution to the decay of the stored beam is collisions with residual gas, which can serve as a means to determine the stored ion beam lifetime.

Due to the low temperature environment of the CSR experimental chambers, the predominant residual gas component is expected to be H_2, which in collisions with the stored ion beams can produce either two or three neutral reaction fragments. The rate of the reaction fragments are proportional to the stored number of ions, which are counted by the NICE detector throughout the ion beam storage time. Therefore, the ion beam lifetime can be determined by measuring the signal induced by collisions with residual gas. More specifically, a beam lifetime can be extracted by fitting the measured decay with an exponent, the parameters of which provide a $\tau = 1/e$ beam lifetime estimate. While a single exponent decay fit almost never fully represents the observed ion beam storage dependence, it is a sufficiently adequate metric to set a reasonable estimate on the ion beam lifetime.

Figure 4.13 depicts the lifetime of a stored H_2D^+ ion beam under two drastically different storage conditions, one of which shows the ion beam storage evolution without electrons (figure 4.13 left). The lifetime indicated by the exponential fit is on the order of $\tau \approx 400\,s$.

However, during the experimental measurements, the ion beam is overlapped with the electron beam at various electron beam densities and interaction times, which typically leads to a reduced beam in terms of the stored number of ions. Therefore, to estimate the most intense reduction in beam lifetime due to recombination with electrons, a measurement was performed by overlapping the ion and electron beams continuously throughout the storage time (figure 4.13 right). At an electron density of $n_e = 2 \cdot 10^5\,cm^{-3}$, this leads to a $1/e$ beam lifetime of $\tau \approx 85\,s$. It is important to note that a lifetime measurement example with such settings is dominated by the DR loss process, which does not represent the experimental parameters (and ion beam lifetimes) employed during the actual DR measurement procedure.

During the present experiment, an electron beam was used in the cooling phase for up to $\approx 1000\,s$, prior to the DR measurements (see section 4.10.3), with a

beam on–time duty cycle of 50 % and a typical electron density of $n_e = 1{\cdot}10^5\, cm^{-3}$. This resulted in an measured ion number of $\approx\ 2 \cdot 10^6$ after $\approx 1000\, s$ of storage time (see section 4.10.4). If one assumes that initially the storage ring acceptance is fully filled by the ion beam injection, which corresponds to $\approx 1 \cdot 10^8$ particles, this leads to an estimated $1/e$ beam lifetime of $\approx$250–300 s, during a typical measurement scheme. In principle, such conditions permit beam storage up to several thousands of seconds, whereafter a DR rate measurement can still be performed.

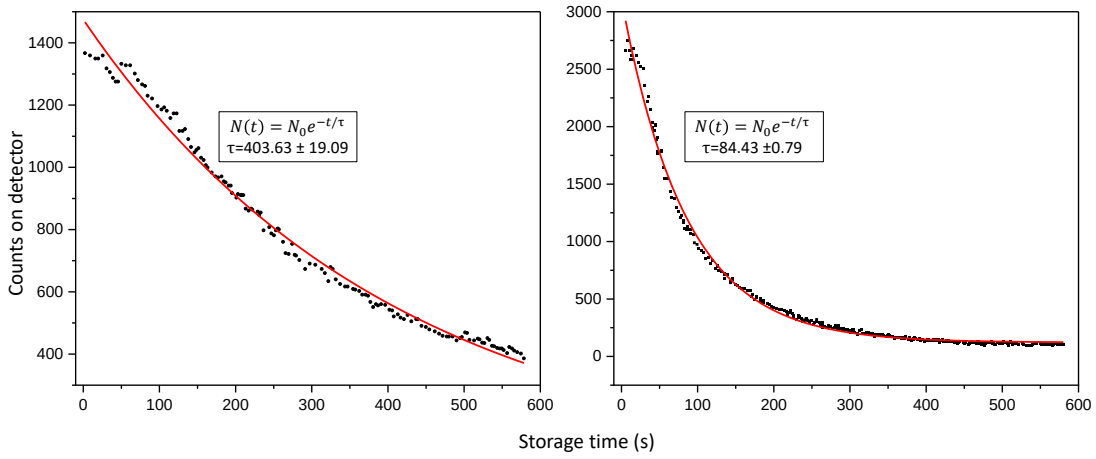

Figure 4.13: H_2D^+ ion beam lifetime measurements at two different storage conditions. Red curve represents a single exponent decay fit made for the first 580 s of ion beam storage at two storage conditions: unperturbed ion beam (left), ion beam that is depleted due to electron recombination by a constantly applied electron beam (right).

4.8 Electron beam characterization

To facilitate a precise dissociative recombination experiment, the characteristics of the merging electron beam must be well known. Therefore, considerable preparation time is devoted towards the investigation of the electron beam properties, especially in aspects regarding the velocity distribution of the electron beam and the quality of the beam profile. Settings that deliver a stable electron density must be found and an optimal merged beams alignment among the ion and elec-

tron beams needs to be established. The following section outlines measurements and procedures associated with fulfilling the stated requirements.

4.8.1 Electron beam profile

As described in previous sections, electrons employed in the present experiment are created in a dedicated electron cooler setup located at one of the straight sections of the CSR. The basic parameter of interest when characterizing the photocathodes output lies within the effective electron density, which can be inferred by measuring the current and the effective radius of the electron beam. The electron beam profile is recorded by scanning the beam across a pinhole located at the end of the electron collector section with the help of steering coils imbedded in the room temperature part solenoid, see figure 4.5. The current is detected by a Faraday cup after the pinhole that measures the electron intensity as a function of the applied steering current. Calibration and measurement procedures that correlates the steering current to a change in beam position were developed in prior work (Wilhelm 2019). Figure 4.14 illustrates an example of a photocathode radius measurement that depicts the electron beam intensity as a function of its radius in a three dimensional contour plot. The goal of these measurements is to obtain the effective radius of the electron beam, which is further used in calculating the electron density. Additionally, settings that produce homogeneous beam profiles exhibiting as little as possible deviations with changing current are established.

The radius of an electron beam that undergoes adiabatic magnetic expansion is related to the photocathode radius by the expansion factor α:

$$r_{beam} = \sqrt{\alpha} r_{cath}, \tag{4.30}$$

where electron beam currents corresponding to r_{cath} values of 1.2113–1.2735 mm were employed in the present work. The present experiment utilized electron beam currents of 7.5 μA, 15 μA, 50 μA, 100 μA and 150 μA. The aforementioned key variables define the electron beam density and are crucial for further data analysis of the obtained DR rates.

4.8.2 Energy and velocity distributions of the electron beam

As the electron beam fulfils the role of a target in the merged–beams experimental configuration, precise knowledge of the energy and velocity distribution are key variables necessary to derive accurate merged–beams rate coefficients.

A comprehensive summary that outlines definitions and conventions used to describe parameters of an adiabatically expanded electron beam in the context of

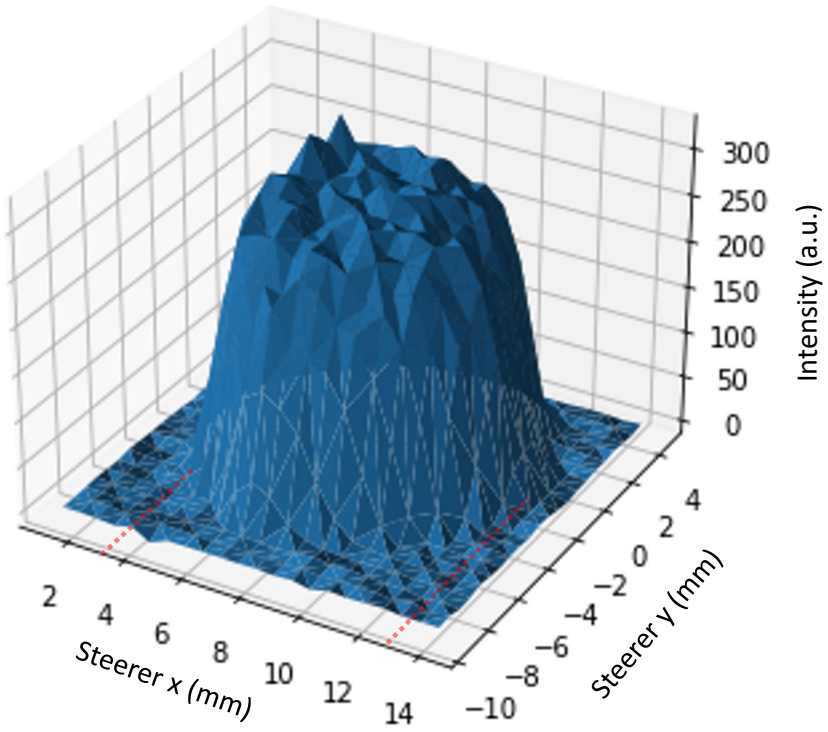

Figure 4.14: An example of a contour plot depicting the electron beam profile. The dashed lines mark the approximate diameter of the beam ($\approx$8.6 mm) corresponding to an effective cathode radius of $r_{cath} = 1.2\,mm$.

merged–beams experiments performed in the now decommissioned TSR can be in found in (Pastuszka et al. 1996). Many aspects of the CSR and TSR electron coolers are analogous, therefore, it is also convenient to follow the established formalism when defining the velocity and energy distribution of the electron beam. The longitudinal and transverse electron beam temperature of a cylindrical beam is expressed as:

$$k_b T_{||} = m_e \left(\left\langle v_{||}^2 \right\rangle - \left\langle v_{||} \right\rangle^2 \right) \tag{4.31}$$

$$k_b T_{\perp} = \frac{1}{2} m_e \left(\left\langle v_{\perp}^2 \right\rangle - \left| \langle v_{\perp} \rangle \right|^2 \right) \tag{4.32}$$

where $v_{||}$ and $v_{\perp}$ refers to the longitudinal and transverse electron velocity, respectively. The electron velocity distribution $f(v)$ in the laboratory frame of

reference follows the so called flattened Maxwellian distribution:

$$f(v) = \left(\frac{m_\mathrm{e}}{2\pi k_\mathrm{B}}\right)^{3/2} \frac{1}{T_\perp \sqrt{T_\parallel}} \exp\left(-\frac{m_\mathrm{e} v_\perp^2}{2k_\mathrm{B}T_\perp} - \frac{m_\mathrm{e}(v_\parallel - \langle v_\parallel \rangle)^2}{2k_B T_\parallel}\right). \tag{4.33}$$

Additionally, it is assumed that due to the strong guiding magnetic fields the transverse and longitudinal velocity distribution can be viewed as decoupled:

$$f(v) = f(v_{||}) f(v_\perp) \tag{4.34}$$

The longitudinal temperature of the adiabatically expanded electron beam directly before the merged beams interaction region is described by the following formula:

$$k_b T_{||} = \left(1 + \left(\frac{\alpha - 1}{\alpha}\right)^2\right) \cdot \frac{k_b T_c^2}{2E_e} + C\frac{e^2 n_e^{1/3}}{4\pi\epsilon_0}, \tag{4.35}$$

where the first term that encompasses the expansion factor α accounts for energy transfer from transverse to the longitudinal movement of the electrons known as the transverse–longitudinal relaxation (TLR) effect, as well as the longitudinal–longitudinal relaxation effect (LLR) that both arise from the change in density of an electron beam undergoing the expansion process. The second term represents the electron beam kinematic compression factor that results as consequence from accelerating the electron cloud away from the vicinity of the photocathode, where T_c denotes the cathode temperature and E_e refers to the energy of the electrons accelerated by an applied potential of U_0. The third term serves the purpose of describing the adiabaticity of the expansion process by expressing the change in electron density n_e via an adiabaticity factor C. For U_0 acceleration voltages on the order of tens of volts the adiabaticity factor has the value of $C \approx 1.9$ as described in (Sprenger et al. 2004). By applying variable values that correspond to typical electron cooler operational conditions into equation 4.35 (e.g. $k_b T_c = 25\,meV$, $E_e = eU_0 = 20\ eV$, $n_e = 1 \cdot 10^5\ cm^{-3}$), the longitudinal electron temperature becomes:

$$k_b T_{||} = 0.27\,meV \tag{4.36}$$

An extended derivation of this formula from basic principles and a step-by-step implementation of the LLR and TLR effects can be found in (Paul 2021).

The initial transverse electron temperature $T_{\perp i}$ is determined by the room temperature photocathode as $k_b T_{\perp i} = 25\ meV$. The acceleration of the electron beam occurs only in the longitudinal direction, therefore, it can be assumed that the transverse velocity $f(v\perp)$ distribution remains unchanged throughout the entirety

of the electron cooler, hence $f(v_\perp)$ adheres to a Maxwell distribution all through the electron cooler:

$$f(v_\perp) = \frac{m_\mathrm{e}}{2\pi k_\mathrm{B} T_\perp} \exp\left(-\frac{m_\mathrm{e} v_\perp^2}{2 k_\mathrm{B} T_\perp}\right) \tag{4.37}$$

As mentioned in chapter 4.5, the transverse electron temperature is further reduced by adiabatic magnetic expansion according to equations 4.1, 4.2. Plugging in the magnetic field values from their respective locations at the electron cooler (see figure 4.5: $B_{gun} = 3000\,G$, $B_{acc} = 200\,G$, $B_f = 100\,G$) into the aforementioned equations, results in an estimate of the lowest transverse temperature limit under ideal conditions of adiabatic expansion:

$$T_{\perp min} = 1.25\,meV \tag{4.38}$$

However, a more tangible lower limit of $T_\perp = 2 - -3\,meV$ has been assumed in present work, as prior experiments (Kálosi et al. 2021, 2022; Novotný et al. 2013) have established that even an actively cooled photocathode with a temperature of $T_c \approx 100\,K$ does not achieve the theoretical limit of $T_{\perp min}$. To summarize, the applied $T_\perp$ value in the analysis of present experiment exceeds $T_{||}$ roughly by an order of magnitude and is the dominant contribution that defines the maximal collisional resolution of the merged–beams interaction process from the point of view of the electron beam.

4.9 Rate coefficients, cross sections and plasma rates

To reiterate: the basic experimental premise of the present work is based on a circulating ion beam stored within the CSR that interacts with the electron beam target in a controlled merged–beams configuration, initiating a dissociative recombination reaction that leads to collisionally induced neutral reaction fragments, which are counted by the NICE detector. The experimentally observed count rate R is dependant on the cross section of the DR process, electron density n_e and the geometry of the overlapped beams:

$$R = \eta_\perp (l_0/C_0) N_{ion} n_e \alpha^{mb}, \tag{4.39}$$

where $\eta_\perp$ represents the transverse overlap fraction, while the factor l_0/C_0 denotes the longitudinal overlap fraction, governed by the length of the merged–

beams section $l_0 \approx 0.721\,m$ and the circumference of the CSR, $C_0 = 35.12\,m$. Note that in this context, the merged–beams rate coefficient (MBRC) α^{mb} is not synonymous with a rate coefficient in its conventional sense, but rather it represents a convolution between the energy dependent cross section $\sigma(E)$ and the collisional energy distribution $f(E)$ that is specific to the experimental setup employed in the present work. To provide more clarity, the nomenclature is slightly adapted from equation 3.8 to account for ambiguities:

$$\alpha(E_d)^{mb} = \int_0^\infty v f(E, E_d)\sigma(E)dE, \tag{4.40}$$

where $v = \sqrt{\frac{2E}{m_e}}$ denotes the velocity of the electrons in the reference frame of the ions and E_d refers to the detuning energy (otherwise called the collisional energy) of the electron beam with respect to matched ion–electron beam velocities.

The term $f(E, E_d)$ describes the probability of an collision event to occur with a certain collision energy. Although the relative velocity of the collisional partners is minimized, the electron beam is characterized by a finite temperature that mainly determines the likelihood of the relative energy of the ion–electron collision process. The full derivation of the function $f(E, E_d)$ is available in (Novotný et al. 2013). In essence, $f(E, E_d)$ encompasses all effects relevant to the center-of-mass energy spread of the electron beam along with the experimental geometry:

$$f(E, E_d) = f(E, E_d, T_{||}, T\perp, X), \tag{4.41}$$

where X represents the overlap geometry. Although there exist analytical approximations of $f(E, E_d)$ (Schippers et al. 2004), here we employ a collisional energy distribution produced by Monte Carlo simulations, a method that was developed by Dr. Oldřich Novotný. The outcome of the simulation for a parameter set relevant for present experiments at a detuning energy of $E_d = 0$ can be seen in figure 4.15. The first of two peaks at around 1 meV arises from the transverse and longitudinal temperatures of the electron beam, while the high–energy tail at $\approx 1\,eV$ is introduced by the electron cooler geometry. To elaborate: in practice the ion and electron beam velocities are matched and detuned within the merged beams section by a drift tube. However, a part of the collisional distribution can still be sampled from regions before and after the drift–tube (edges of the merging beam section) that corresponds to electrons with a higher relative velocity with respect to the ions. This manifests as the secondary peak in the $f(E, E_d)$ plot. It will be later shown that the high–energy peak is inconsequential to the measured DR rate due to the low sampling probability of the $f(E, E_d)$ distribution in tandem with the low rate coefficient associated at that particular detuning energy range.

When discussing the relevance of ion–electron interaction processes in the con-

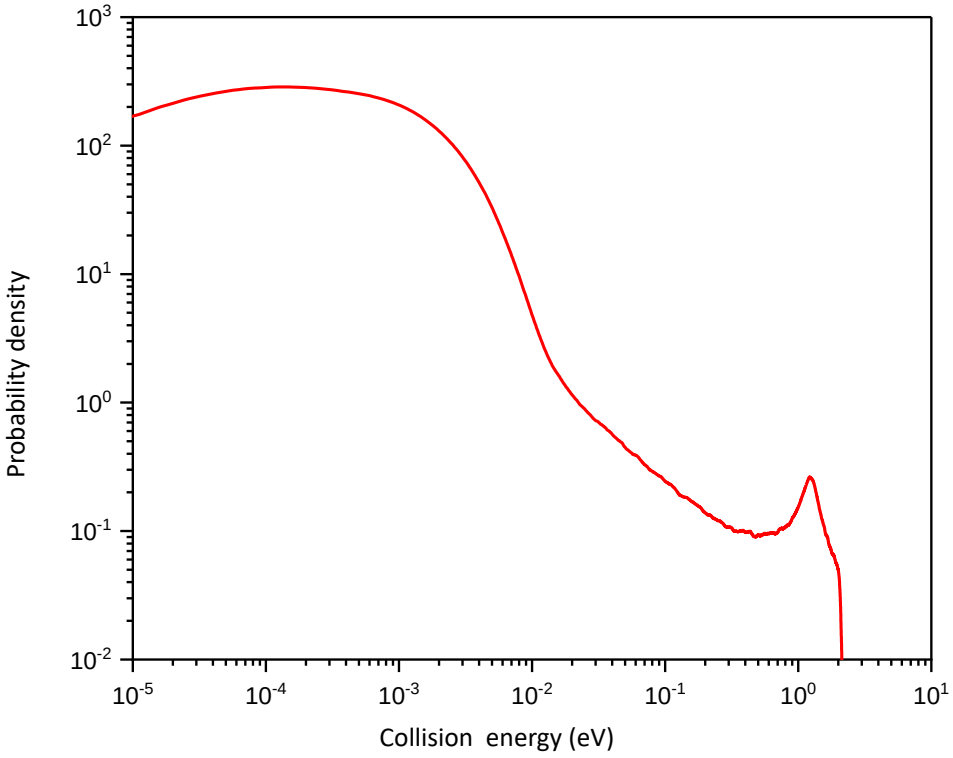

Figure 4.15: Simulated collisional energy distribution at $E_\mathrm{d} = 0\,eV$. The simulation assumes an electron beam with a transverse temperature of $T_\perp = 2\,meV$ and a longitudinal temperature of $T_\perp = 0.3\,meV$. An electron density of $n_\mathrm{e} = 1.1 \cdot 10^5\,cm^{-3}$ and a cathode of temperature $T_\mathrm{c} = 25\,\mathrm{meV}$ is assumed.

text of astrophysical environments, it is customary to model said environments as a plasma with a certain temperature T_{pl} in which the collisional energies of a reaction follow a thermal Maxwell–Boltzmann distribution $f_{pl}(E)$. Convolving the energy dependant cross section $\sigma(E)$ with the thermal distribution $f_{pl}(E)$ results in a plasma rate coefficient:

$$\alpha_\mathrm{pl}(T_\mathrm{pl}) = \int_0^\infty \sigma(E) v f_\mathrm{pl}(E) dE = \int_0^\infty v\sigma(E) \sqrt{\frac{4E}{\pi (k_\mathrm{B} T_\mathrm{pl})^3}} \exp\left(-\frac{E}{k_\mathrm{B} T_\mathrm{pl}}\right) dE \tag{4.42}$$

The analytical expression of $f_{pl}(E)$ distribution is well described and the numerical computation of the integral is unambiguous if $\sigma(E)$ is sufficiently well known. However, as previously stated, the experimentally observed reaction rate and by extent the cross section is convolved with the collisional energy distribution function $f(E, E_d)$ that is specific for the current merged–beams configuration. Therefore, before the plasma rate coefficient can be calculated the cross sections

need to be deconvolved.

Details regarding the deconvolution procedure can be found in (Novotný et al. 2013). At its core, the deconvolution method is based on an iterative approach, where an initial model cross section $\sigma'(E)$ is convolved with the collisional energy distribution function $f(E, E_d)$ according to equation 4.40. Thereafter the generated model rate coefficient $\alpha'^{mb}(E_d)$ is compared to the experimentally obtained rate coefficient $\alpha^{mb}(E_d)$. During the deconvolution process the energy dependant cross section $\sigma(E)$ is split into narrow energy bins of $\sigma_i(E)$ with the assumption that $\sigma_i(E) = const$ throughout the chosen energy interval. By minimizing the χ^2 value of each energy bin, a model $\alpha'^{mb}(E_d)$ that agrees with the experimental $\alpha^{mb}(E_d)$ is obtained. Ultimately, the deconvolved cross section is employed in equation 4.42 to calculate the temperature dependant plasma rate coefficient $\alpha_{pl}(T_{pl})$.

In summary, it is important to note that nomenclature as established in equations 4.39, 4.40, 4.42 shall be followed throughout the rest of the work.

4.10 Data acquisition and analysis procedures

4.10.1 Data acquisition system

When optimal experimental conditions in terms of ion and electron beam control and characterization have been achieved, the measurements of the DR reaction are initiated. The main components of the data acquisition system consists of the NICE detector and the camera–DAQ interface that accompanies it. After the DR reaction takes place in the merged–beams region the neutral fragments exit the nominal ring orbit and impinge on the detector. The events are counted by a CMOS camera that is triggered by the electronic pulses generated by particles hitting the phosphorus screen. Following detection of the electronic pulses the signal is digitized into waveforms that contain information regarding the pulse properties, namely arrival time, amplitude and number of pulses, which are extracted by online analysis (on CPU).

Complementary to the signal generated by digitizing the pulses generated on the phosphor screen, the camera records and evaluates data on the basis of individual frames. The camera continuously integrates the signal that arises from ambient light. After a trigger signal has been received, the camera will acquire photons for 2 more μs before closing the shutter, which is a sufficient time window to identify and correlate signals that corresponds to neutral fragments belonging to

a concurrent collision event. Thereafter, the acquired data are transmitted to a frame grabber within a timescale of 1 ms and the camera shutter opens again. A simplified schematic that outlines the data acquisition process is shown in figure 4.16. As the imaging data are not part of the present analysis, further details will be omitted.

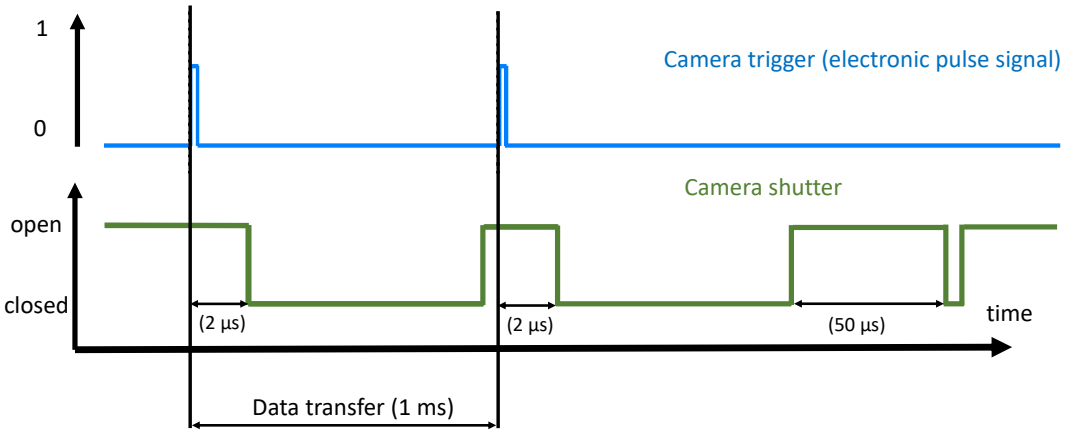

Figure 4.16: Schematic of the NICE detector data acquisition timing scheme (figure not to scale). The dashed lines mark the beginning of measurement events. To discriminate against events that occur due to stray light, the camera periodically does not integrate and transfer data for 50 μs intervals if there are no trigger signals.

4.10.2 Detection efficiency

As any MCP detector, NICE is characterized by an intrinsic detection efficiency that is determined by the surface area of the detector and limited by the inactive area between the MCP channels. An extended investigation of the NICE detector detection efficiency (Novotný et al. 2019) resulted in a value of

$$p = 0.593(15), \tag{4.43}$$

that is further employed in the present work.

However, due to the nature of the DR process, the KER release can result in neutral fragments that feature distances at which some of the dissociated products no longer hit the detector. Therefore, a more important variable that contains the

intrinsic detection efficiency p of the MCP and additionally includes probabilities associated with detecting an incomplete amount of fragments of a DR event is the effective detection efficiency η.

As the dissociative recombination reaction of triatomic hydrogen cations can result in either a two body or three body fragmentation, the following probabilities must be considered.

For a three body dissociation event, the detection efficiency can be calculated by the following formula:

$$\eta_{tripples} = p^3 + 3p^2(1-p) + 3p(1-p)^2, \tag{4.44}$$

where:

- p^3 – probability to detect all three neutral fragments simultaneously,
- $3p^2(1-p)$ – probability to detect two out of three neutral fragments,
- $3p(1-p)^2$ – probability to detect one out of three neutral fragments.

The detection efficiency for a two body dissociation event can be obtained similarly:

$$\eta_{doubles} = p^2 + p(1-p) + p(1-p), \tag{4.45}$$

where:

- p^2 – probability to detect both neutral fragments simultaneously,
- $p(1-p)$ – probability to detect the atomic fragment, but not the molecular fragment,
- $p(1-p)$ – probability to detect the molecular fragment, but not the atomic fragment.

By substituting the MCP intrinsic detection efficiency into equations 4.44 and 4.45 one arrives at values of $\eta_{tripples} \approx 0.93$ $\eta_{doubles} \approx 0.83$. The detection efficiency is further utilized when implementing the absolute scaling of the DR rate measurements where an η=0.88 $\pm$0.05 value is assumed in the analysis. It should be noted that the detection efficiency is actually a function of the detuning energy due to the changes in the two-to-three fragment ratio with detuning energy. Present analysis assumes $\eta(E_d)$ to be constant throughout the detuning energy range and estimates that the influence of such an effect is small enough to be encompassed within the uncertainty of η=0.88 $\pm$0.05.

4.10.3 DR measurement structure

A typical DR measurement run consists of various phases that feature different application purposes of the overlapped electron beam. Key properties of the electron beam that are varied are electron beam density and relative collision energy. Adjustments in electron beam energy during a measurement run is referred to as *wobbling*. The entire measurement run is split into parts that are called schemes that differ from one another by interaction parameters (timings and detuning energies) meant to fulfil various purposes. Schemes are further subdivided into cycles and steps, as illustrated in figure 4.17 which shows the structure of a single measurement run. The following paragraph is dedicated to provide details regarding the significance and purpose of each measurement phase.

In the initial part of the measurement run a cooling scheme is utilized to achieve an ion beam that is stable, reduced in size and characterized by a minimal energy spread. With the information provided by simulations that describe evolution of the molecular ion ensemble internal energy distribution, a decision was made to designate an electron cooling period of up to $1000\,s$ prior the DR measurement scheme. These time scales ensure a compromise of a well–defined internal state definition while retaining practicality in terms of measurement time and count rate. During the cooling scheme the electron beam is operated at a detuning energy of $E_d = 0$ with a reduced intensity of $7.5\,\mu A$ compared to the maximal current used in the measurement steps of $150\,\mu A$, in order to avoid excessive loss of the stored ion beam. Furthermore, a $50\,\%$ duty cycle is used, characterized by switching between a $50\,ms$ "beam on" time followed by $50\,ms$ of "beam off" time.

Subsequently, it is assumed that the ion beam energy spread is defined by that of the electron beam and the measurement scheme is initiated. The measurement scheme consists of a series of wobbling cycles, each corresponding to a certain detuning energy that is varied throughout the scheme. Each wobbling cycle consists of a certain quantity of steps (smallest unit in this nomenclature) depending on the purpose of the measurement scheme. When switching between a detuning energy of $E_d = 0$ that corresponds to the cooling step condition, to a detuning energy of $E_d \neq 0$ of a measurement step, the electron beam can induce dragging effects that manifest as a change in the ion beam velocity. To minimize this influence, the electron beam remains at a detuning energy of $E_d = 0$ for the majority of the measurement cycle, while switching to the desired detuning energy occurs only for a fraction of time, typically following the ratio of 4:1 with respect to the cooling step.

A roughly equivalent amount of time within the measurement cycle is spent on a reference detuning energy, that is used as a normalization signal for further analysis. The reference detuning energy is chosen such, that the measured rate

exhibits no changes with respect to storage time and has no resonant features, such as coupling to Rydberg state. In the context of DR measurements of small molecular ions, these conditions are typically satisfied at relatively high detuning energies of $> 10\,eV$ and in present work a detuning energy of $12.42\,eV$ was chosen.

Every measurement cycle incorporates an "off" step at which the residual gas background rate is sampled with no electrons present within the storage ring. The background rate is later subtracted from both the reference and measurement steps. A $5\,ms$ waiting period is inserted between every measurement step within the scheme to account for stabilization of the electron beam at which times no rate is sampled. An example of the timings employed in a typical measurement run consists of:

- $\approx 1000\,s$ of electron cooling with a $50\,\%$ duty cycle that corresponds to consecutive iteration between $50\,ms$ of electron beam "on" and "off" time,
- $\approx 300\,s$ of measurement scheme defined by varying between $100\,ms$ of electron cooling, $25\,ms$ of measurement and reference steps each, followed by $25\,ms$ of an "off" step,
- each measurement scheme is completed by a $100\,ms$ cycle sequence of ion free measurement that corresponds to the detector dark count rate.

Every measurement run is characterized by $\approx$50–100 detuning energy values repeated hundreds to thousands of times in order to record statistically sufficient data sets.

The NICE detector is capable of acquiring imaging data, that allows for association of induvial collisional events to the number of reaction fragments. Although such data has been recorded for each measurement, it will not be analysed and discussed in the present work. Therefore, the current analysis treats all detector events equally as a single count towards the detection rate, independent of the branching ratios between the two–body and three–body dissociation channels. This results in a detected rate of:

$$R_i = \frac{\Delta N_i}{\Delta t_i}, \tag{4.46}$$

where ΔN_i represents number of events within a given time Δt_i that can correspond to any of the cycle steps. The typical count rates in the present experiment were on the order $\approx\ 1000\,s^{-1}$. The total detected rate pertaining to a specific measurement step as illustrated in the measurement scheme (figure 4.17) is given by:

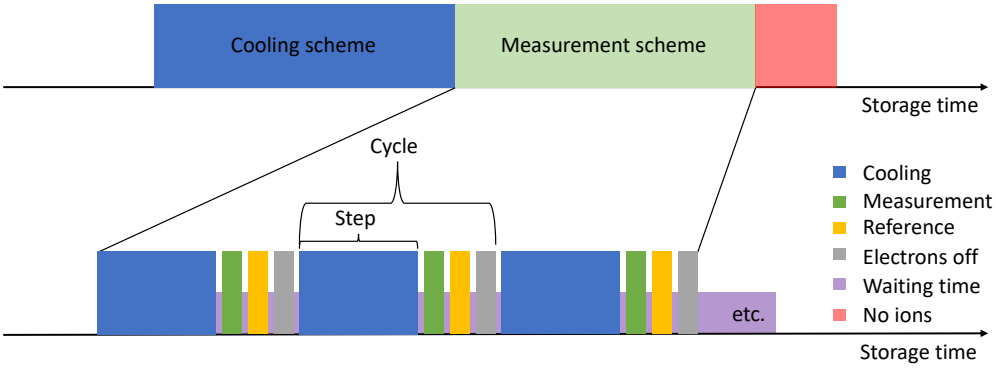

Figure 4.17: Data acquisition scheme for a DR measurement run. A single measurement run consists of several phases denoted as schemes, cycles and steps corresponding to different detuning energy E_d values. A waiting time accompanies the change between every measurement step type in order to account for voltage stabilization. Every measurement run includes steps for background measurement.

$$R_{meas.tot} = R_{dark} + R_{off} + R_{meas}, \tag{4.47}$$

$$R_{ref.tot} = R_{dark} + R_{off} + R_{ref}, \tag{4.48}$$

$$R_{off.tot} = R_{off} + R_{dark}, \tag{4.49}$$

where R_{ref} and R_{meas} are electron induced rates at a certain detuning energy E_d.

The residual gas induced rate $R_{off.tot}$ can be further expanded upon as:

$$R_{off.tot} = \alpha_{r.g.} n_{gas} N_{ion} + R_{dark} \tag{4.50}$$

and is dependant on the remaining residual gas particle number n_{gas}, number of ions stored N_{ion} and an effective residual gas rate coefficient $\alpha_{r.g.}$. The count rate recorded from the residual gas induced events R_{off}, as well as the detector dark count rate R_{dark}, need to be subtracted from the overall signal R_{mb} to separate the rate R_{meas} that originates solely from electron induced collisions at a certain detuning energy. R_{mb} is defined identically to equation 4.39 and is obtained by normalizing the count rate recorded in a measurement step $R_{meas.tot}$ by a reference count rate $R_{ref.tot}$:

$$R_{mb} = \frac{R_{meas.tot} - R_{off.tot}}{R_{ref.tot} - R_{off.tot}} = \frac{R_{meas}}{R_{ref}}, \tag{4.51}$$

where the reference count rate is always measured at a single, constant detuning energy value throughout all of the measurement runs.

The reference count rate R_{ref} and the normalization factor S that represents the signal per number of ions is obtained as:

$$\frac{R_{ref.tot} - R_{off.tot}}{N_{ion}} = \frac{R_{ref}}{N_{ion}} = S \tag{4.52}$$

By using equation 4.39 the electron induced rate R_{meas} can be expressed as:

$$\frac{R_{meas}}{N_{ion}} = \eta_{\perp}(l_0/C_0)n_e\alpha^{mb}_{meas} = R_{mb}S, \tag{4.53}$$

which leads to:

$$R_{mb}S = \frac{R_{meas}}{R_{ref}}\frac{R_{ref}}{N_{ion}} = \eta_{\perp}(l_0/C_0)n_e\alpha^{mb}_{meas}, \tag{4.54}$$

or:

$$\alpha^{mb}_{meas} = \frac{R_{mb}S}{\eta_{\perp}(l_0/C_0)n_e} = \frac{R_{meas}}{N_{ion}}\frac{1}{\eta_{\perp}(l_0/C_0)n_e} \tag{4.55}$$

As the individual steps (R_{meas}, R_{ref}, R_{off}) of the wobbling scheme occur within a few tens of mili–seconds from one another, the average residual gas induced rate in one injection cycle remains almost constant and is removed from the electron induced rate together with the detector dark count rate. Measurement runs characterized by abnormally high rates within the R_{off} step typically indicate a problem and are generally discarded from the analysis. It is important to emphasize that equation 4.55 is central for obtaining the main results of the present work.

4.10.4 Ion number determination

To acquire an absolute MBRC each measurement run includes a time window at which the ion current and by extent the ion number in CSR is determined. The number of ions is inferred by measuring the mirror charge that arises from a bunched ion beam propagating through the capacitive current pick–up. The working principles of the pick–up systems were discussed in paragraph 4.7.3 (see figure 4.11). Each revolution of the ion beam generates a voltage signal $U_p(t)$ within the pick–up circuit that is characterized by a certain waveform, an example measurement can be seen in figure 4.18.

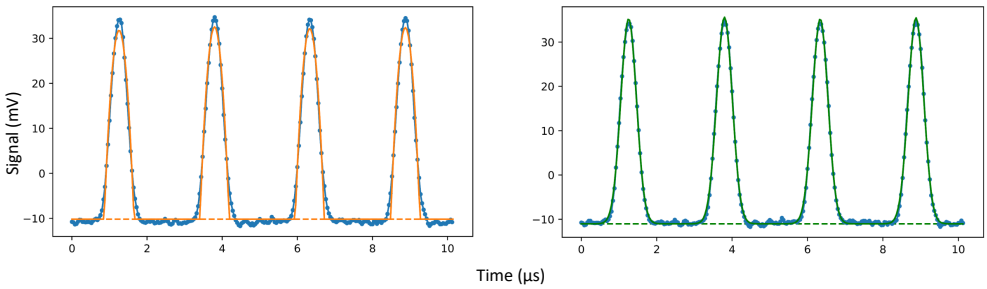

Figure 4.18: Ion number determination. Voltage induced in the current pick–up by a RF–bunched ion beam is correlated to the number of ions in a bunch as described in equation 4.56. The average signal (blue) is fitted by either a parabolic (orange) or Gaussian (green) model in order to calculate the integral in equation 4.56. An average value of both fits is used in the analysis. The dashed lines denote the fitted offset value.

Whence a statistically sufficient multitude of the waveforms have been acquired ($\approx$ 10000) the average voltage signal can be fitted by a Gaussian or a parabola to correlate the measured signal on the current pick–up with the number of ions within the ring:

$$N_{ion} = \frac{C_p C_0}{z e L_0 T_0 G} \int_0^t U_p(t) dt, \tag{4.56}$$

where C_p – capacity of the current pick–up, C_0 – circumference of CSR, z – charge state of the ion, L_0 current pick–up length, t – ion beam revolution time, G – amplifier gain. As an example, by substituting in the relevant numbers within formula 4.56: $C_p = 96.0(48)\,pF$, $L_0 = 30\,mm$, $T_0 = 10.0162\,\mu s$, $G \approx$ 3000, and evaluating the fitted integral, the number of ions within the CSR is determined to be $2.44 \cdot 10^6$ after $\approx 1000\,s$ of beam storage.

4.10.5 Summary of the measurement procedure and uncertainty estimates

The following section will provide a summary of the measurement procedure and a breakdown of the statistical and systematic uncertainties of the experimental measurements.

To reiterate, the initially measured quantity in the present DR experiment is detected counts on the NICE detector associated with various experimental steps in a measurement scheme at a given relative collision energy (paragraph 4.10.3). The measurement steps within one scheme are structured in such a manner (equation 4.51) that, when combined with key parameters of the experimental setup,

produces a relative merged–beams rate coefficient at a given detuning energy E_d and ion beam storage time t:

$$\alpha^{mb,rel}(E_d, t) = \frac{R_{mb}}{\eta_\perp (l_0/C_0) n_e}, \tag{4.57}$$

where all the variables have been discussed in previous sections. Thereafter, by varying the relative collisional energy E_d, a DR spectrum is recorded at different ion beam storage times.

To convert $\alpha^{mb,rel}(E_d, t)$ to an absolute rate coefficient requires the input of the detection efficiency $\eta(E_d)$ (paragraph 4.10.2) and number of stored ions N_{ion} (paragraph 4.10.4):

$$\alpha^{mb,abs}(E_d, t) = \frac{R_{meas}}{\eta_\perp (l_0/C_0) n_e \eta(E_d) N_{ion}}, \tag{4.58}$$

that scales the entire measurement curve.

The statistical error of the measured DR rate R at given detuning energy is calculated by:

$$\Delta R = \sqrt{\left(\Delta m \cdot \frac{\partial R}{\partial m}\right)^2 + \left(\Delta o \cdot \frac{\partial R}{\partial o}\right)^2 + \left(\Delta r \cdot \frac{\partial R}{\partial r}\right)^2}, \tag{4.59}$$

where m, o, r correspond to countrates in the measurement, off and reference steps, respectively. The value of ΔR significantly varies throughout the experimental DR curve from $< 1\,\%$ to several hundreds of precent in the low rate coefficient region. The statistical and systematic uncertainties are always displayed separately in the present work.

A determination of the transverse overlap value $\eta_\perp$ is described in the supplementary material of (Kálosi et al. 2022). Present analysis assumes that $\eta_\perp$ is predominantly governed by the electron beam. After $1000\,s$ of ion storage, it is reasonable to assume that the remaining stored ion beam and the electron beam are described by a near unity transverse overlap in the merged–beam section, therefore $\eta_\perp$=1. Previous estimates (Kálosi et al. 2022), suggest a 4% uncertainty of $\eta_\perp$ under similar experimental conditions.

An ideal electron target would provide a perfectly defined interaction region at a certain overlap length among the electron–ion beams, without any collisional events outside the interaction zone. Furthermore, collisions would occur at a strictly fixed relative collision energy. In practice, any merged–beams setup is characterized by an effective overlap length l_{eff} that includes geometry effects and is characterized by a certain collision energy distribution at a given relative collision energy. The associated uncertainty for the CSR electron cooler was determined in the work of (Saurabh 2019), and for ion beam parameters employed

in the present work, is calculated to be:

$$\frac{\Delta l_{eff}/C_0}{l_{eff}/C_0} = 1.5\% \tag{4.60}$$

The electron density at the merged–beam interaction zone is given by:

$$n_e = \frac{I_e}{e\pi r_{beam}^2 v_e}, \tag{4.61}$$

with equation 4.30 correlating the electron beam (r_{beam}) and effective cathode (r_{cath}) radii. The principle uncertainty of the electron density originates from the cathode radius (r_{cath}). As the present experiment employed r_{cath} values of 1.2113–1.2735 mm, the uncertainty is assumed as Δr_{cath}=0.0311 mm. This leads to an electron density uncertainty of:

$$\frac{\Delta n_e}{n_e} = 10.0\,\%, \tag{4.62}$$

which is a reasonable estimate compared to previous DR measurements (e.g., Paul 2021).

The derivation of the detection efficiency of the NICE detector was given in section 4.10.2. Here, the value is noted again as $\eta(E_d)$=0.88±0.05. Thus, the uncertainty of the detection efficiency is given by:

$$\frac{\Delta\eta(E_d)}{\eta(E_d)} = 5.7\,\%, \tag{4.63}$$

The uncertainty of the stored ion number measurement depends on the evaluation of the integral in equation 4.56, the determination of which is described in the previous paragraph 4.10.4. Every measurement run is accompanied by an ion number measurement and a fitted waveform. The uncertainty ΔI when determining the integral:

$$I = \int_0^t U_p(t)dt \tag{4.64}$$

arises from the parabolic and Gaussian fits and their associated fitting parameters, that change on a per measurement run basis. The uncertainty of the integral in 4.64 throughout the measurements of present experimental campaign is characterized by:

$$\frac{\Delta I}{I} = 12.7\,\%, \tag{4.65}$$

which together with a 5 % uncertainty of the amplifier gain G (Paul 2021) leads to a total uncertainty in the determined ion number:

$$\frac{\Delta N_{ion}}{N_{ion}} = 13.7\,\%, \tag{4.66}$$

Therefore, the total systematic uncertainty of the absolute energy dependant merged–beams rates coefficient determined in the present work is:

$$\frac{\Delta\alpha^{mb,abs}(E_d,t)}{\alpha^{mb,abs}(E_d,t)} = 22.4\,\%, \tag{4.67}$$

derived by addition of the individual uncertainties in quadrature.

Chapter 5

Experimental Results

5.1 Recombination rate coefficient results

The following paragraph details results acquired in the measurement campaign of February 2022. The two main experimental objectives that were set for the beamtime can be summarized as follows:

- Investigate the DR process by recording the MBRC spectra of rotationally cold H_2D^+ and D_2H^+ molecular ions at the CSR experimental setup,
- Obtain MBRC rates at various ion beam storage times to probe the time evolution of the ion ensembles and establish evidence of rotational cooling.

In an ideal experiment, MBRC would be acquired continuously throughout the ion beam storage time. However, this is not feasible due to practical limitations, therefore the present measurement campaign has focused on obtaining the DR rates at select ion beam storage time windows. The measurement runs can be split into two distinct categories that are characterized by the ion beam storage times prior the DR measurement scheme. The corresponding timescales are referred to as *short* and *long* ion beam storage times throughout the following chapter. The intention of such an approach is to identify and illustrate the changes in the measured MBRC that arise due to sampling the DR reaction with a hotter and colder molecular ion ensemble.

5.1.1 MBRC energy dependence

To understand the DR process, it is fundamental to study the cross sections dependence as a function of the collisional energy. The experimentally obtained MBRC and the deconvolved cross sections that arise from it serve as a benchmark for the state-of-the art theory calculations and are further employed to determine plasma rate coefficients that are typically used to approximate reaction probabilities when modelling astrophysically relevant environments as a plasma in thermal equilibrium. The derivation of the plasma rate coefficients and the astrophysical implications will be discussed in paragraph 5.1.5.

Figure 5.1 depicts the recorded MBRC spectra for H_2D^+ (upper panel) and D_2H^+ (lower panel) as a function of detuning (collision) energy. To fully display the measured results the rates are plotted on a doubly logarithmic scale, where the changes in relative collisional energy span more than seven orders of magnitude throughout which the measured MBRC also changes drastically. The graphs consists of two comparative plots with MBRC rates acquired at short and long storage times to demonstrate the largest observed contrast between features of both curves that arise from the change in internal population distribution of the stored ions. The following paragraphs explains the general shape of the curves and elaborates on the origins of specific features.

As described in section 2.4.1, the DR process occurs via the direct and indirect dissociation pathways. The rise of the measured DR rate in the high energy part starting at $\approx$3–4 eV originates from the direct DR process, while the low energy part and the corresponding emerging structures manifest due to the indirect process. It is to be noted, that although the electron beam longitudinal temperature $T_{||}$ is on the order of $\approx 200\,\mu eV$, the transverse beam temperature is $T_{\perp}$ $\approx 2\,meV$ (section 4.8). Therefore, $T_{\perp}$ is the main limiting factor of the collisional energy resolution, meaning that any resonances located below the aforementioned relative detuning energy threshold will most likely not be visible in the MBRC spectra. However, the measured energy dependence of the rate coefficient below $E_d = 2\,meV$ holds valuable insights on the DR process, as will be shown in the following paragraphs.

The plots in figure 5.1 are shown with purely statistical error bars and do not encompass the overall uncertainty of 22 % that arises mainly from the absolute scaling procedure, which together with other uncertainties is discussed in paragraph 4.10.5. The majority of the data are characterized by a low statistical error, except the region between $\approx$0.6–4 eV, where the reaction rate decreases by more than three orders of magnitude compared to the maximal signal.

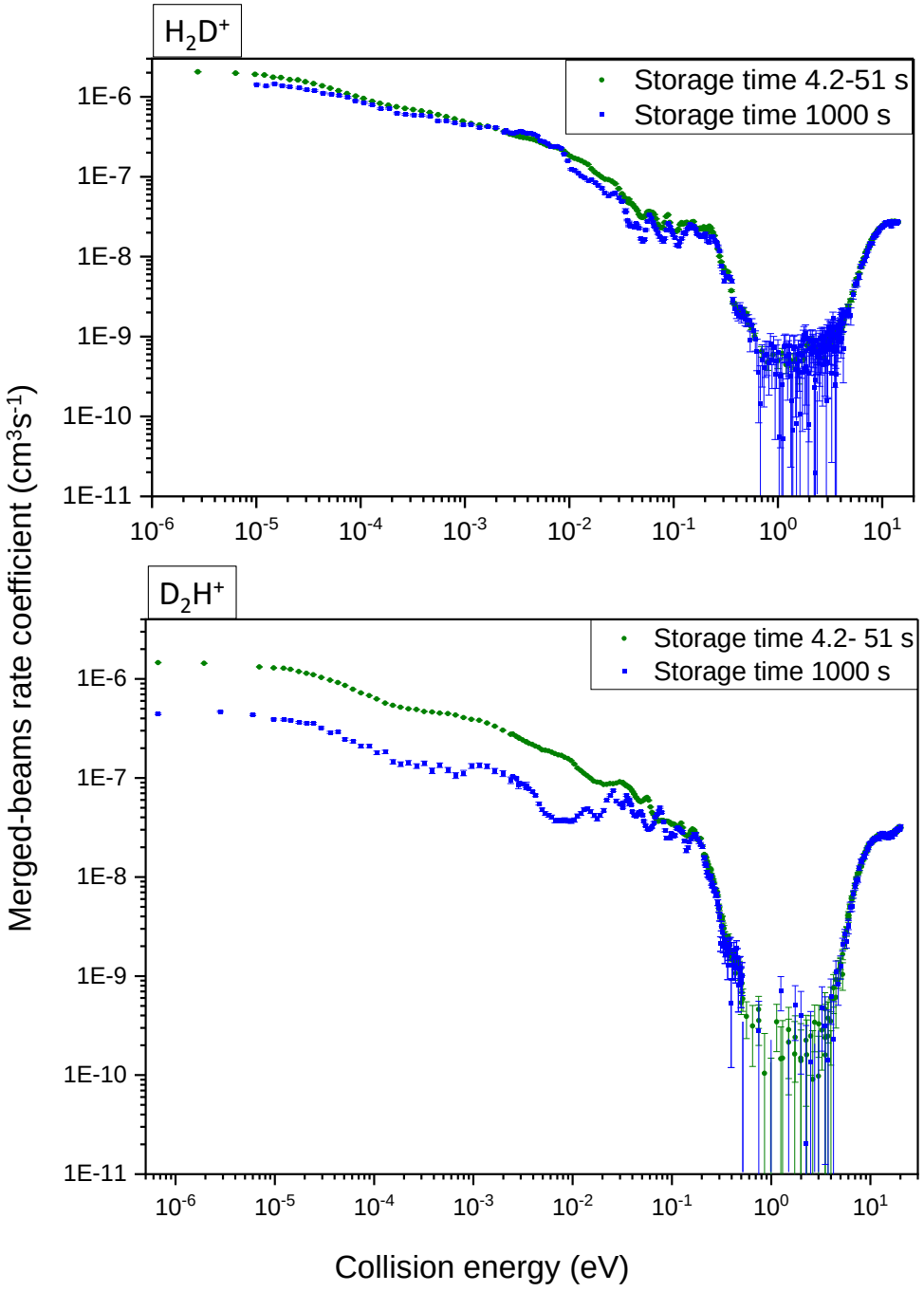

Figure 5.1: Experimental merged–beams rate coefficient measured at short (green) and long (blue) storage times. The graphs are shown with statistical error bars, while in addition the enitre data set features an absolute uncertainty of 22 % associated with the absolute scaling.

As the expected behaviour of the direct DR process follows an $\approx 1/\sqrt{E_d}$ dependence, it is convenient to display the low collisional energy part that exhibits features attributed to the indirect process by multiplying the entire MBRC curve by a factor of $\sqrt{E_d}$, as seen in figure 5.2. Such a scale emphasizes the structure emerging in the detuning energy range from 1–300 meV. According to state-of-the-art theoretical calculations, rovibrational Rydberg resonances play a significant role in the DR probability. Features in the detuning energy range of 0.1–0.3 eV are attributed to Rydberg resonances attached to the lowest vibrationally excited states, which become energetically accessible at 0.274 eV for H_2D^+ and at 0.244 eV for D_2H^+ respectively, followed by a sharp drop in the observed MBRC. The decrease in rate after the vibrational threshold signifies that the energy of collisional interactions gets transferred into excitation of the molecule, rather than dissociation, until the direct process takes over at roughly 4 eV, indicated by the rise in measured MBRC. In a similar manner, the broadened structure at few mili–electronvolts is explained by DR that occurs via the indirect channel by coupling to a series of rotational Rydberg resonances, which cannot be separated with present experimental resolution.

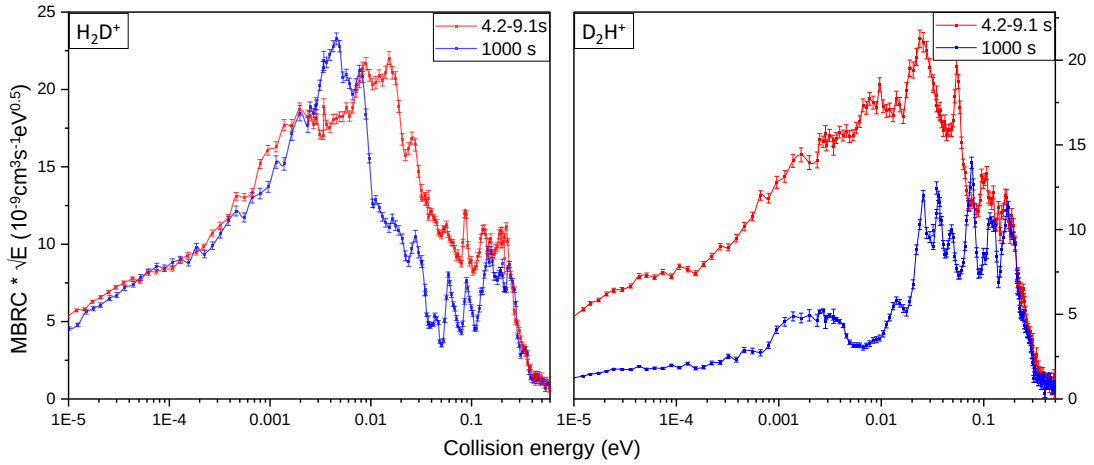

Figure 5.2: Experimental MBRC data sets of short (red) and long (blue) storage times plotted by removing the $1/\sqrt{E_d}$ dependence. The resulting scale emphasizes changes in observed MBRC that arise form the indirect DR process at low detuning energies. The graphs are shown with statistical error bars, while in addition the enitre data set features an absolute uncertainty of 22 % associated with the absolute scaling.

5.1.2 Storage time evolution

The influence of the rotational excitation on the DR reaction can be evaluated by examining the MBRC time evolution. As the vibrational lifetimes are on the order milliseconds, any vibrational excitation is believed to be absent even for the short storage time measurements, which is corroborated by the results of the model calculations (section 3.3). Therefore, any observable characteristics of the MBRC spectra and their changes with storage time are attributed to changes in the population of individual rotational states.

Both systems exhibit an overall decrease in the measured MBRC with ion beam storage time, with the change in rate being much more prominent in the case of D_2H^+ compared to H_2D^+ (see figure 5.1). The general trend of decreasing MBRC is associated with the reduction in average energy left in the system (as seen in figure 3.7) that occurs due to rotational relaxation of the molecules. Figures 5.3 and 5.4 show that the majority of the change in MBRC is observed within the first $\approx 150\,s$ of storage time for the case of H_2D^+, where the measured rate at $100\,s$ mostly adheres to that of the MBRC at $1000\,s$.

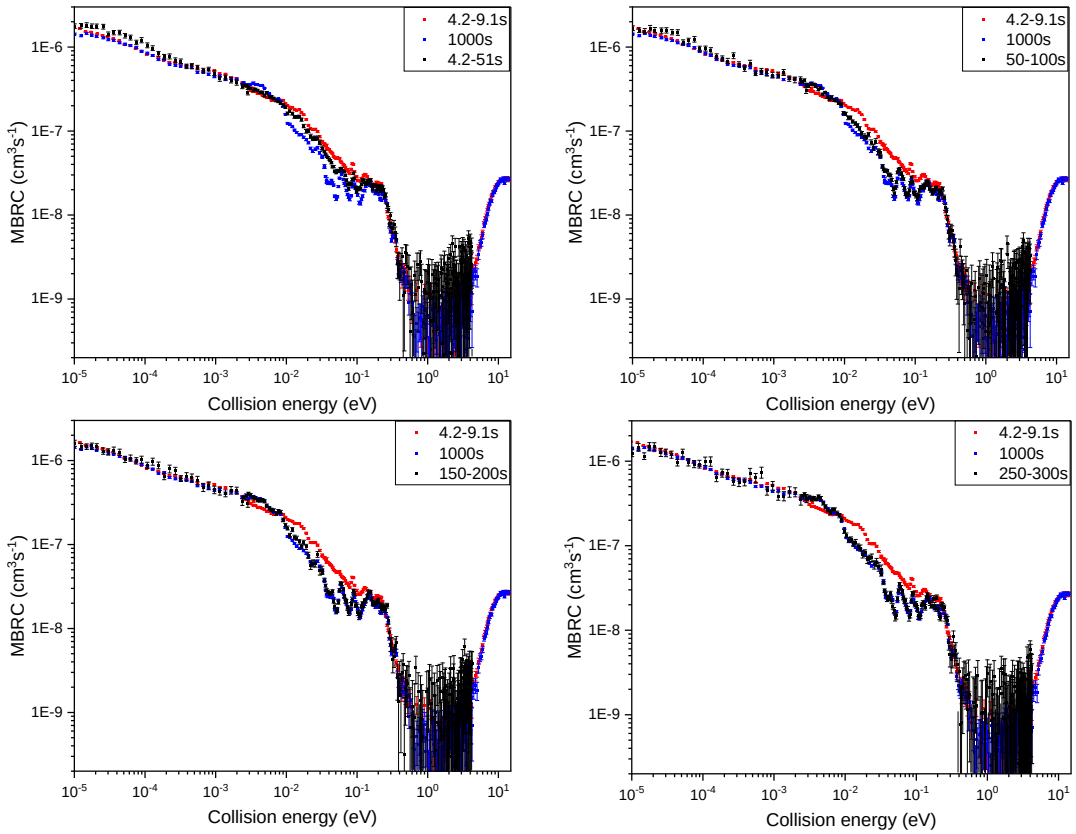

Figure 5.3: Measured H_2D^+ MBRC at various storage time intervals.

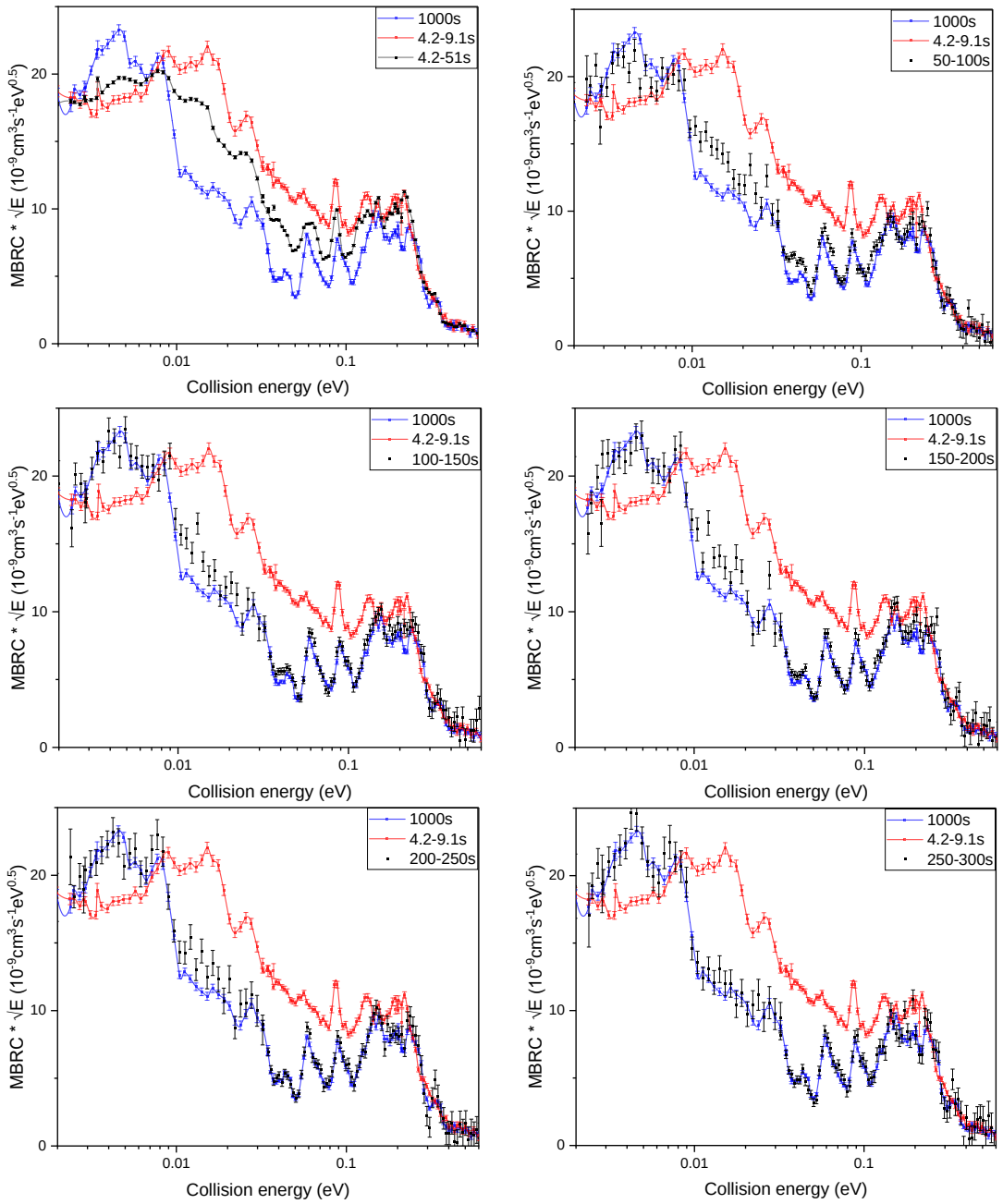

Figure 5.4: Measured H_2D^+ MBRC at various storage time plotted by removing the $1/\sqrt{E_d}$ dependence.

In essence, the most prominent shifts in internal population distribution for the case of H_2D^+ occur within the first 100 s of ion beam storage time, whereafter no drastic changes in the measured rate can be observed. This implies that most of the rotational cooling takes place within 100 s and any further changes in the population distribution develop on significantly longer timescales. Similar

conclusions can be drawn from the results of the model calculations (figure 3.6).

Although, the D_2H^+ data exhibits similar tendencies, the rotational cooling appears to be slower (figure 5.5), evident by ongoing changes in measured MBRC at time scales exceeding $300\,s$, which are particularly apparent in the structured part of the curve (see figure 5.6). The discrepancies of the cooling behaviour among the two systems can be understood by examining the simulated population evolution (figure 3.6) and the theory DR rate predictions of the lowest rotational states (figure 3.5).

If one evaluates the DR theoretical predictions of the remaining populated rotational states (figure 3.5), it is evident that the MBRC for D_2H^+ spans a significantly larger range than the H_2D^+ rates. The corresponding rotational states are populated longer for the case of D_2H^+, which leads to the observed changes in the measured MBRC on timescales of several hundred's of seconds (figures 5.5, 5.6).

The combination of slower rotational cooling, in tandem with the comparatively increased population in the higher excited rotational states for D_2H^+ at long storage times is most probably responsible for the increased amount of Rydberg resonance associated features.

It is to be noted that the acquired data of the measurement runs that span ion beam storage times from $50 - 300\,s$ and $50 - 400\,s$ for H_2D^+ and D_2H^+ respectively are binned with $50\,s$ time intervals. Smaller time slices were deemed to be detrimental to the statistics of the data. A missing aspect in current analysis relates to correlating the change in the MBRC to changes in population of individual quantum states, as performed for HeH^+ (Novotný et al. 2019) and CH^+ (Paul 2021). Despite the relatively distinguished structured part of the MBRC spectra and the small amount of populated rotational states, there were no obvious features that could correlate a specific rotational state to the MBRC time evolution.

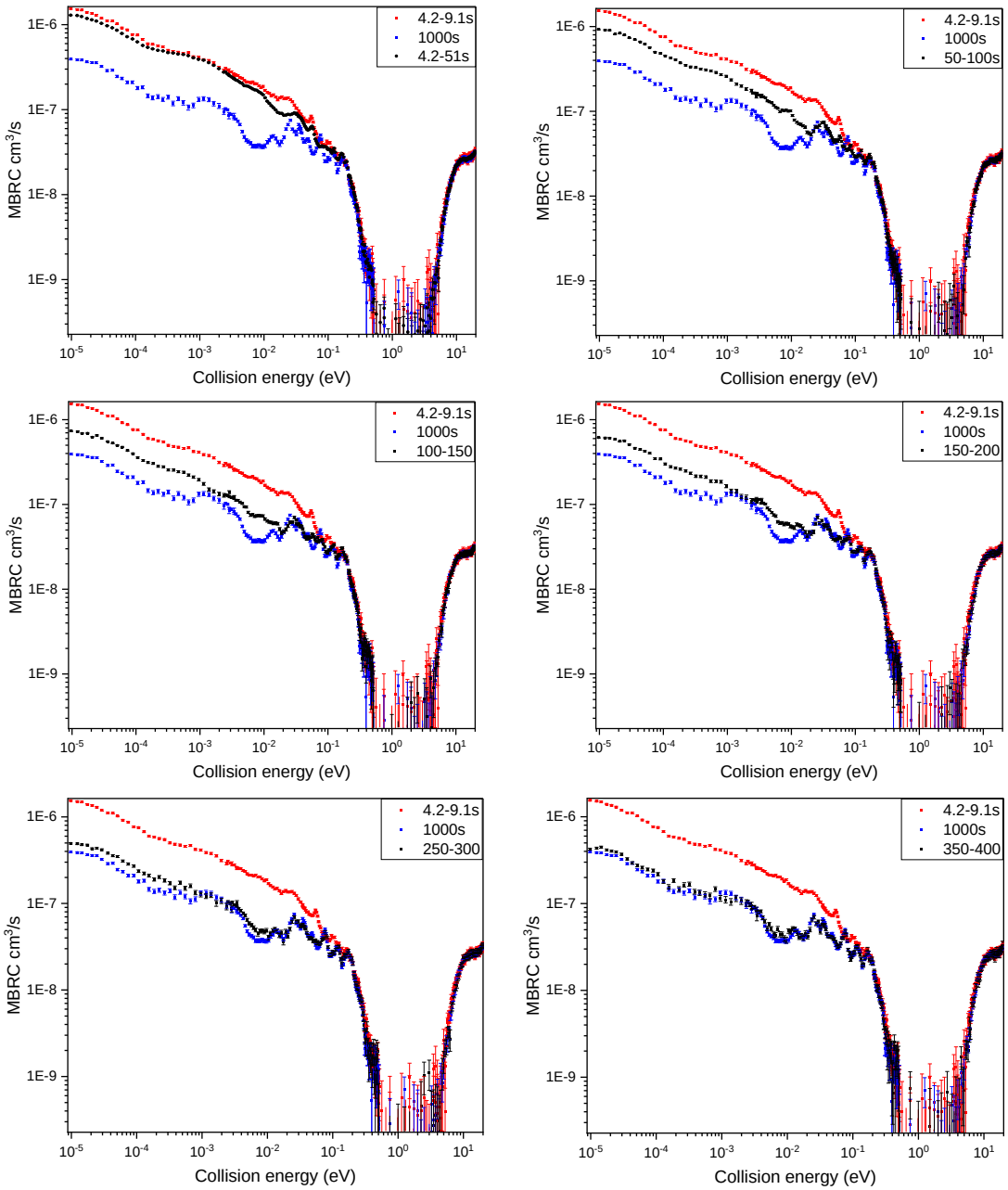

Figure 5.5: Measured D_2H^+ MBRC at various storage time intervals.

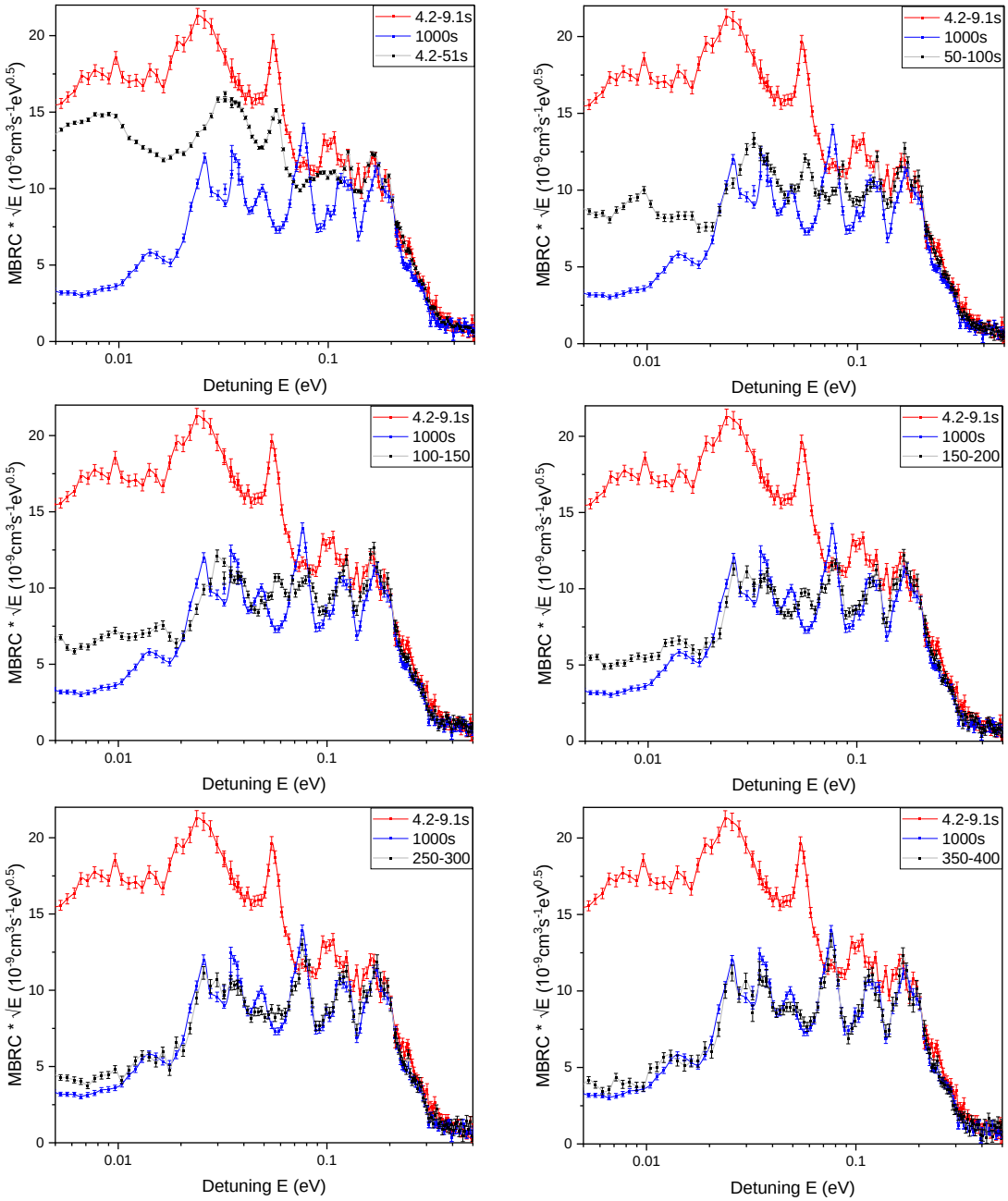

Figure 5.6: Measured D_2H^+ MBRC at various storage time plotted by removing the $1/\sqrt{E_d}$ dependence.

5.1.3 Comparison to previous experiments

To further evaluate the experimental results, it is useful to compare the present results with previous measurements.

Prior data of H_2D^+ dissociative recombination measurements in a storage ring environment are sparsely available, with one of the few attempts being realized at the room temperature ion storage device CRYRING, located at Stockholm (Datz et al. 1995). The aforementioned experiment was among the first DR measurements performed at the CRYRING facility, the results of which are overlaid with present experiment in figure 5.7 (top panel). Both present and prior data are absolute rate measurements, therefore can be directly compared.

The extracted cross sections from Datz et al. 1995 were transformed into rate coefficients by multiplication with the electron velocity ($v_e = \sqrt{2E_d/m_e}$). The CRYRING results do not agree with present experiment throughout most of the collisional energy range, although there is an agreement region for some of the structured energy range. It is important to emphasize that the CRYRING data represent room temperature measurements with a maximal resolution of $10\,meV$, limited by the transverse temperature of the employed electron beam. This alone could explain the discrepancies when comparing to present data, while an undefined amount of rovibrational excitation is present when performing the measurements. Furthermore, CRYRING measurements featured H_2D^+ beam lifetimes on the order of few tens of seconds, which are non–sufficient timescales for rotational cooling to equilibrate the internal population distribution.

Additionally, the ion source utilized in CRYRING measurements produces both H_2D^+ and D_2^+ ions. Although the source parameters were optimized for production of H_2D^+ and the measurement technique incorporated discrimination against events that occur due to DR of D_2^+ , the recorded DR rate might inevitably be influenced by the contaminant. Overall, the results achieved from measurements at the CSR represent a large step forwards in understanding the DR reaction on the basis of individually populated rotational states from both experimental and theoretical point of view.

Comparisons with more recent experimental data can be drawn in the case of D_2H^+, while again adhering to ion storage ring measurements. Figures 5.7 (bottom panel) and 5.8 illustrate two notable data sets measured at the TSR (Lammich et al. 2003) and CRYRING (Zhaunerchyk et al. 2008). Both previous measurements are obtained at room temperature conditions, therefore, despite the prospects of electron cooling, the recorded rates originate from DR reactions with considerably hotter molecular ensembles in terms of rotational excitations than the CSR rates of the present work.

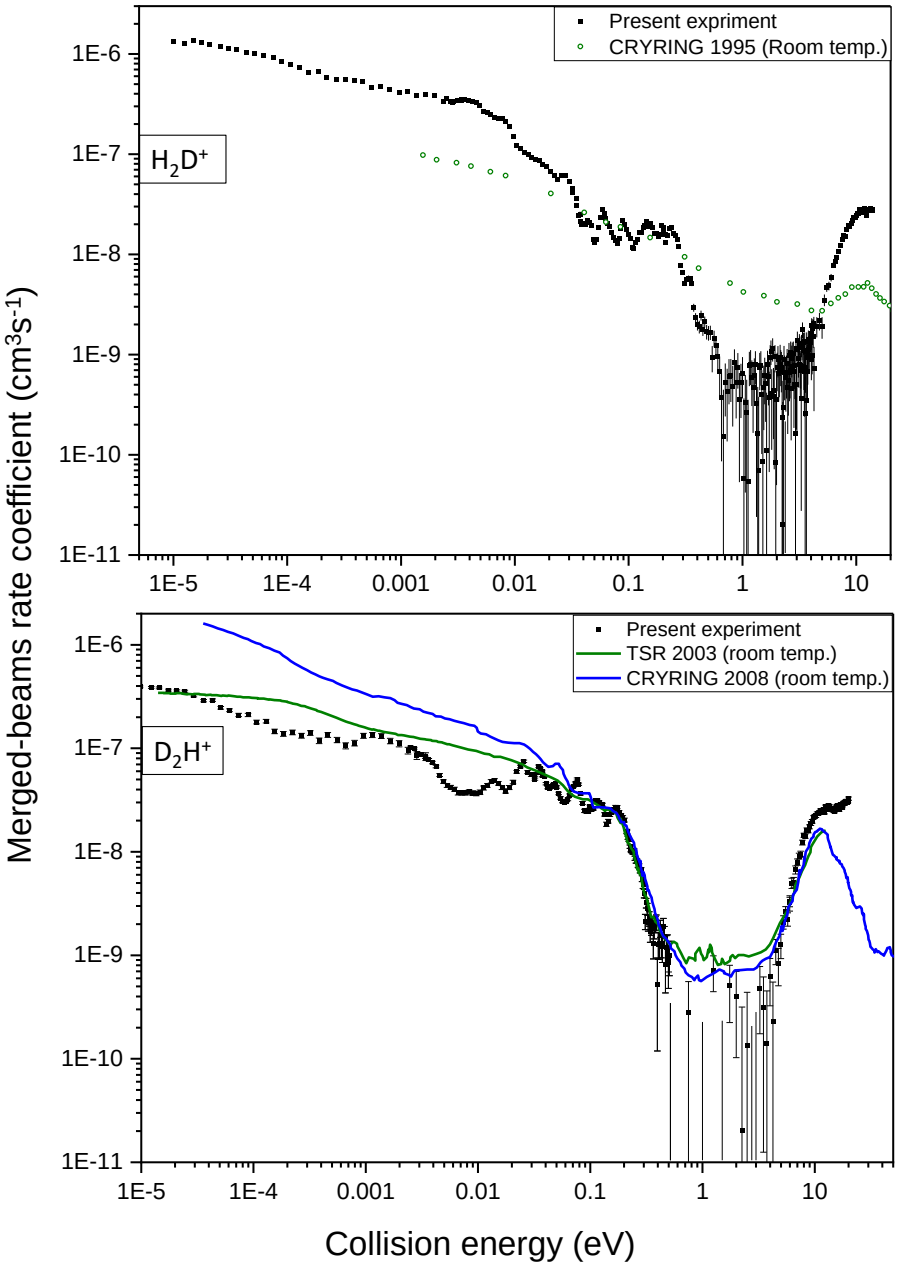

Figure 5.7: Comparison to previous experimental results. The present experimental data correspond to MBRC measured after long storage times (1000 s). Data for H_2D^+ comparison (top panel) was extracted from (Datz et al. 1995), while the D_2H^+ results originate from (Lammich et al. 2003) and (Zhaunerchyk et al. 2008), respectively (bottom panel). If the publications did not feature a rate coefficient, it was obtained by multiplying the energy averaged cross sections by the electron velocity $v = \sqrt{\frac{2E_\mathrm{d}}{m_\mathrm{e}}}$.

Both comparison curves represent absolute measurements, with the TSR data characterized by a resolution of $12\,meV$ and a total uncertainty of $\approx 30\,\%$, while the CRYRING results feature a resolution of $2\,meV$ and a total uncertainty of $\approx 20\,\%$. All three experimental data sets of figure 5.7 are in good agreement above $\approx 70\,meV$, disregarding the absence of the structures present in the CSR data.

The disagreement in the high energy part, which is associated with the direct DR process, might be explained by the inability to distinguish between DR and DE processes in the CSR measurements. However, the observed discrepancy might simply be associated with the overall uncertainty as well.

Below $\approx 70\,meV$ the three experimental data sets separate from one another, especially the results from CRYRING. The reason for the variation between experimental results lies within the remaining rotational excitation of the molecules, as well as the differences in the resolution of collision energy among the experimental data sets. The TSR results claim a sub–thermal rotational temperature

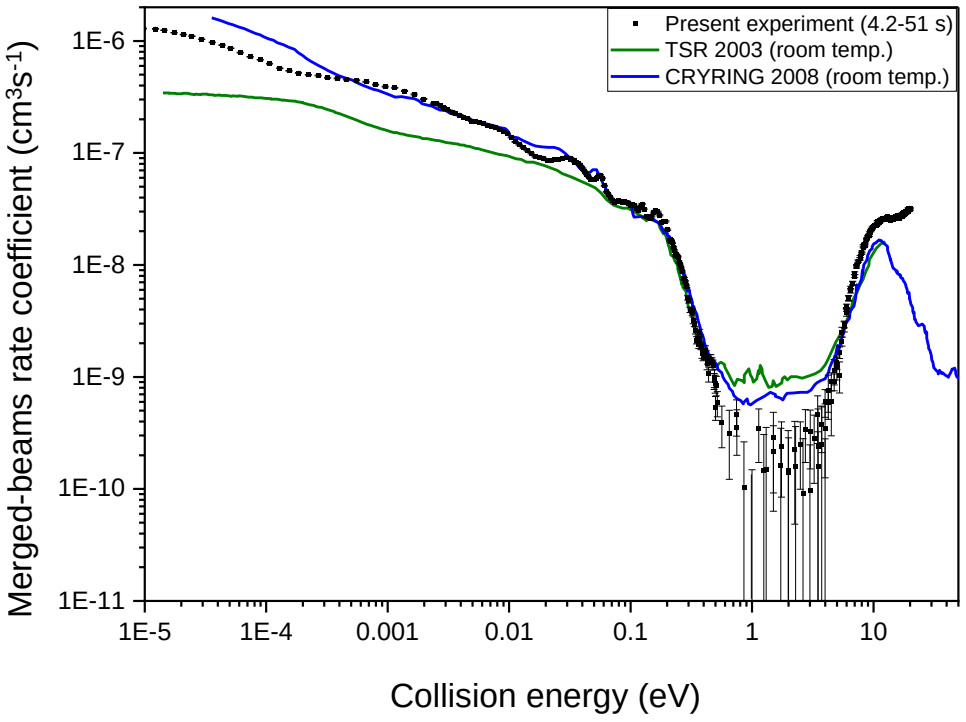

Figure 5.8: Comparison to previous experimental results for the case of D_2H^+ The displayed present experimental data correspond to MBRC measured at short storage times (4.2–51 s), while the TSR and CRYRING data sets are the same as described in figure 5.7.

(Lammich et al. 2003), while the CRYRING data are characterized by a rotational temperature of $<70\,meV$ (Zhaunerchyk et al. 2008), which accounts for the smoothed and increased rate coefficient at low energies compared to the CSR results. This statement is further corroborated if one compares the short storage time data (4.2–50 s) acquired at the CSR to the CRYRING results that are obtained at similar ions storage times (figure 5.8). It is apparent that both of the results are in excellent agreement, even exhibiting similar features along the MBRC curve, which instils confidence, that the CSR data are obtained with rotationally colder ions.

In summary, the comparison of present CSR results with previously available data for DR measurements of H_2D^+ and D_2H^+ signify the achieved experimental advancements that allow for the investigation of the DR reaction with rotationally cold ions with previously unprecedented state definition.

5.1.4 Comparison to theory

Sections 2.5.1 and 3.3.4 discussed the theoretical basis employed to calculate the DR process, while also outlining the state-of-the-art calculation approaches that are applied for present molecular systems. The energy dependant cross sections of the individual rotational states presented in current work were provided by Kokoouline and Greene 2023.

To make use of the theoretical cross sections they need to be convolved with the CSR electron cooler collisional energy distribution function, as described in chapter 4.9. Thereafter, the resulting convolved rate coefficients (figure 3.5) can be compared to the experimental MBRC of the present work. The comparisons between experiment and theory provided in the following paragraphs will be made against experimental data sets that represent the best attainable state definition in the present work. Such conditions corresponds to the longest ion beam storage time MBRC, the internal state population distribution of which can be seen in figure 3.6.

Figure 5.9 shows the comparison between the experimental data of H_2D^+ and the four individual rotational states that are significantly populated at ion storage times of 1000 s according to the model calculations. The absolute ground state (0_{00}) of the para manifold exhibits a significantly lower rate coefficient throughout the calculated detuning energy range, especially at the low energy part below $10\,meV$. Additionally, the peaks of the structured part are lower in amplitude and are located at slightly different positions compared to the other three rotational states. The remaining other rotational states broadly exhibit the same features with some variance in peak position and amplitude. It is evident that none of the four individual rotational rate data can reproduce the peak positions and

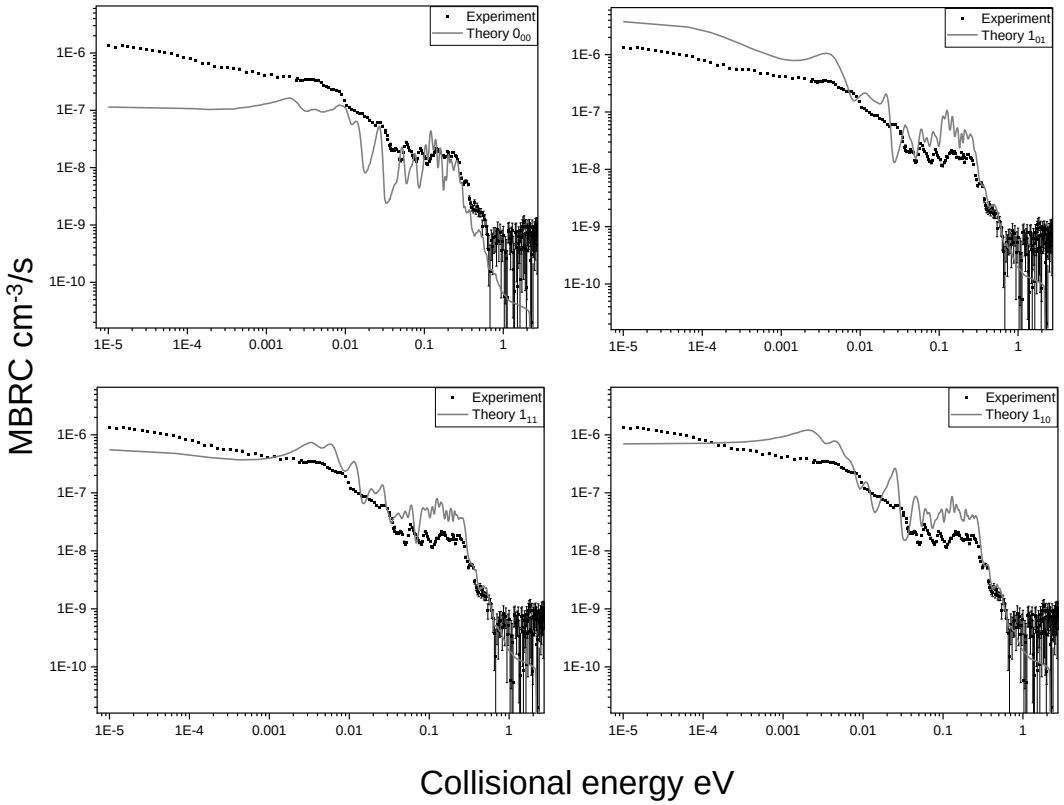

Figure 5.9: Comparison between experimental and theoretical MBRC curves of the four lowest rotational states of H_2D^+. The displayed experimental data correspond to MBRC measured after long storage times (1000 s).

amplitudes of the experimental independently, rather a mixture of all four is necessary.

To that end the individual theory curves were weighed and normalized by the predicted population distribution according to the simulations. This is achieved by extracting the normalized population values of the individual rotational states after a simulated storage time of 1000 s (figure 3.6) and multiplying them with their respective theoretical DR rate curves. For the case of H_2D^+ the lowest four rotational state populations correspond to: $0_{00} = 0.186$, $1_{01} = 0.015$, $1_{11} = 0.546$, $1_{10} = 0.252$. Thereafter, the contributions of the individual curve data are summed to obtained the final MBRC. This approach produces the red curve in figure 5.10, that corresponds to the current best comparison among experimental and theoretical data. The experiment and theory curves agree within a factor of 2–5 throughout the entire displayed detuning energy interval, with even better agreement for the detuning energy range of 0.3–2 eV.

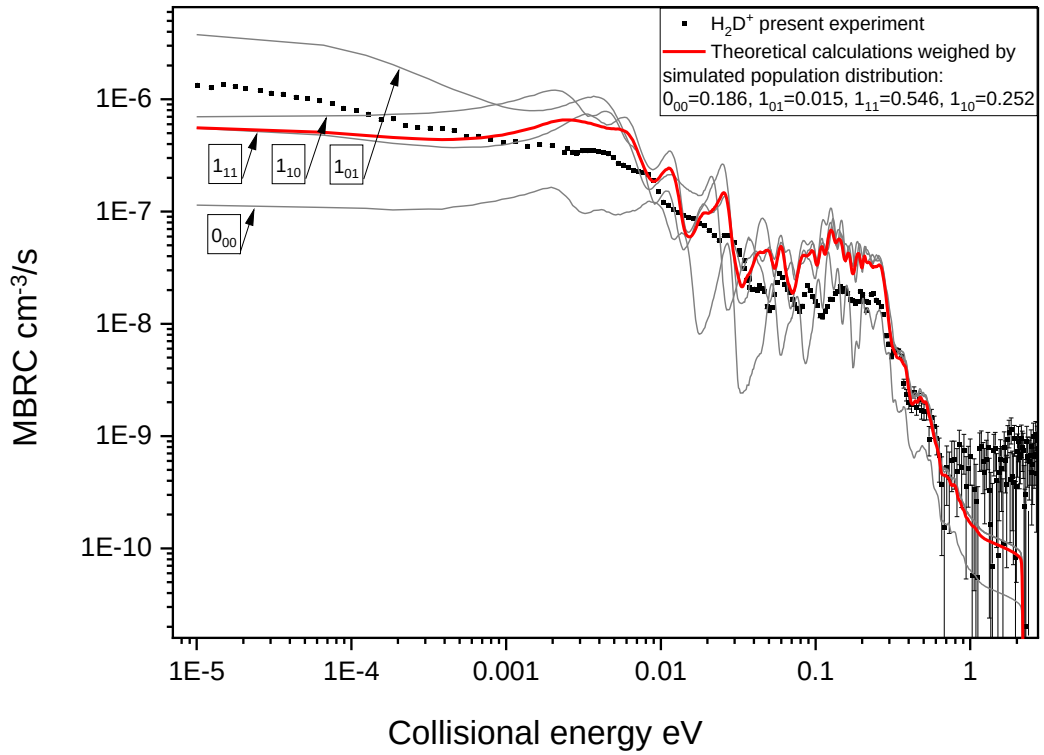

Figure 5.10: Comparison between experimental and theoretical MBRC values for the case of H_2D^+. The graph entails four lowest rotational states calculated by theory (grey) compared to experimental MBRC measured after long storage times (black). The red curve represents the current best estimate of the internal state composition of the measured molecular ensemble obtained by weighing the theory curves by the population distribution acquired from simulation calculations.

The same comparisons where also produced for the case of D_2H^+, where the simulation results predict the influence of more rotational states on the observed MBRC after storage time of 1000 s (see figure 3.6). The populations of nine rotational states where incorporated to obtain the weighed curve as seen in figure 5.11 (a detailed comparison among theory and experiment can be seen in figure 5.12). Similar conclusions can be drawn regarding the absolute ground state of D_2H^+, which features a significantly lower rate coefficient among other rotational states.

The resulting weighed theory curve mostly reproduces the experimental results in terms of peak positions and amplitudes within a factor of two for the structured detuning energy range part within 3–200 meV and with an even better

agreement in the 0.2–2 eV range. However, the low energy tail exhibits a worse agreement than that of the H_2D^+ case. Although, it is important to note that this discrepancy is overemphasized by the logarithmic scale. It may very well be the case, that the disagreement in the low energy part below the experimental resolution of 2 meV stems from only one rotational state resonance.

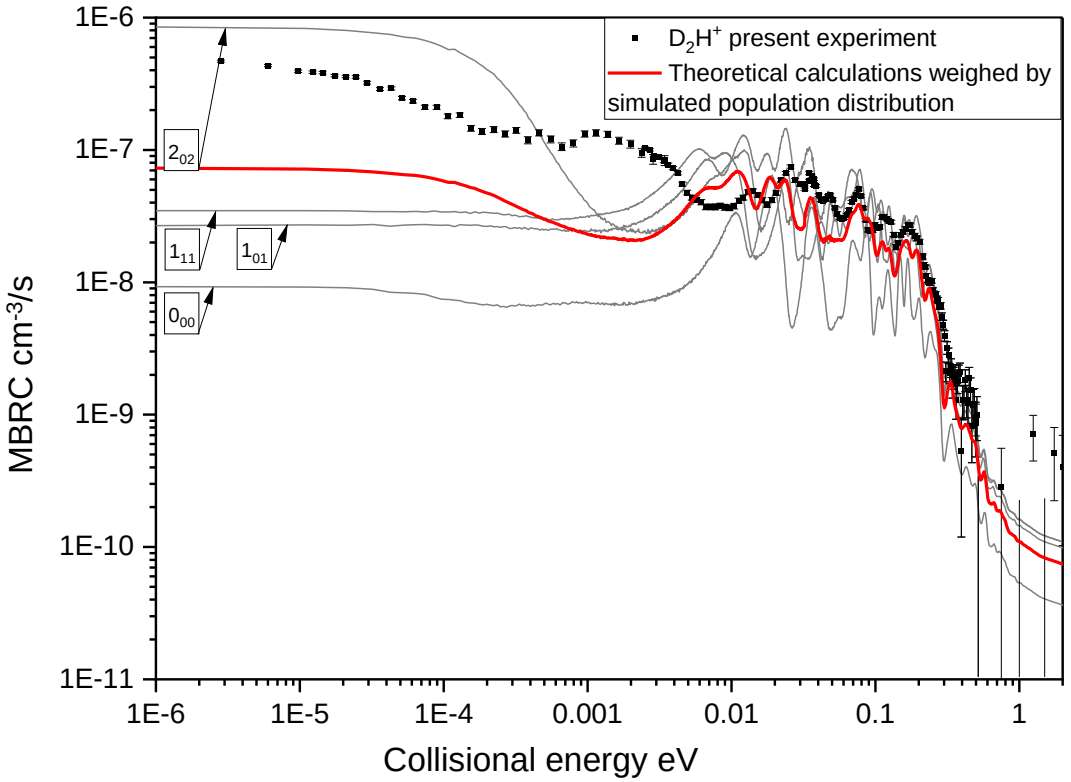

Figure 5.11: Comparison between experimental and theoretical MBRC values for the case of D_2H^+. The graph entails the four most populated rotational states calculated by theory (grey) compared to experimental MBRC measured after long storage times (black). The red curve represents the current best estimate of the internal state composition of the measured molecular ensemble obtained by weighing the theory curves by the population distribution acquired from simulation calculations.

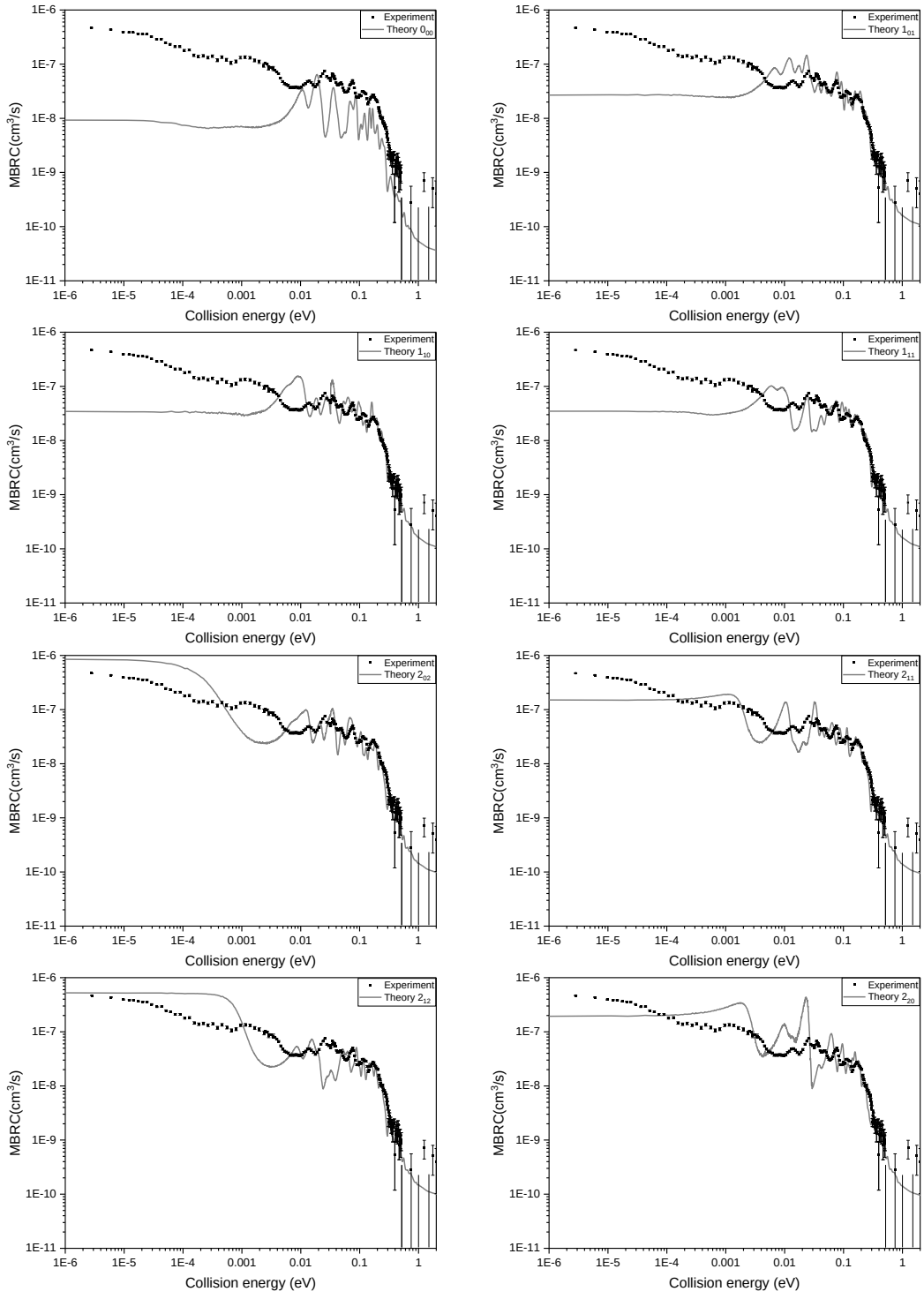

Figure 5.12: Comparison between experimental and theoretical MBRC curves of the lowest rotational states of D_2H^+. The displayed experimental data correspond to MBRC measured after long storage times (1000 s).

It must be once more emphasized that calculations of the DR theoretical cross sections are an extremely difficult task. To illustrate this point figure 5.13 shows the state of the MQDT theory calculations of the DR process of H_3^+ in the early 2000's (Orel, Schneider, and Suzor-Weiner 2000) against the best experimentally available data at that time (Larsson et al. 1993). While, the cross–sections corresponding to the collisional energies of the direct DR process seem to converge on the same order of magnitude, the theoretical calculations of the indirect DR part disagree with the experimental results by several orders of magnitude. This discrepancy mainly arises due to incomplete or incorrect incorporation of the indirect DR process within the cross–section calculations. Therefore, the agreement between theory and experiment in the present work represents tremendous progress from both, experimental and theoretical point of view.

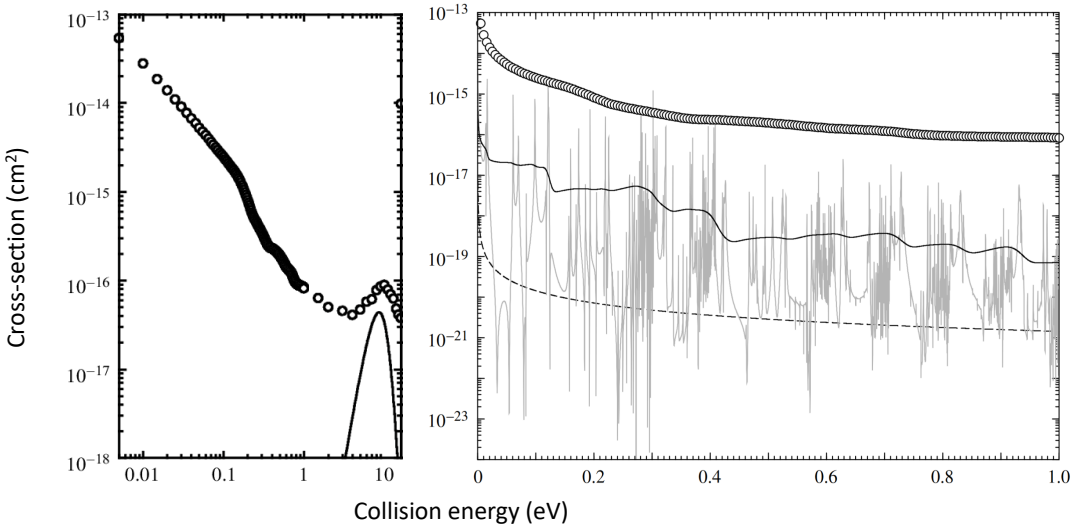

Figure 5.13: Comparison between theory and experiment in the early 2000's. Theoretical cross–sections from (Orel, Schneider, and Suzor-Weiner 2000), experimental data (black circles) from (Larsson et al. 1993)(left panel). The dashed black line denotes the computed direct cross–section (right panel). The grey line denotes the total (direct and indirect) cross–section. The solid blackline denotes total cross–section convolved with the experimental resolution of CRYRING.

In summary, the data presented in current work is characterized by the best agreement between theory and experiment attained for a dissociative recombination reaction of a triatomic system. Present results represent a significant improvement over prior work, as it was not uncommon for experiment and theory to differ by several orders of magnitude. The remaining discrepancies in the collisional energy range of 2–300 meV are most likely associated to the exact choice

of Rydberg resonances in terms of level energies and coupling strengths, which can considerably shift the position of the peaks and their amplitudes. As for the experimental side – there are only small remnants of higher excited rotational states. The elimination of such excitation could benefit the exclusion of additional contributions to the overall observed rate, but the impact would not be drastic. It is difficult to comment about the potential disagreement causes of the low energy tail below $2\,meV$ as the transverse temperature limits the experimental resolution. Furthermore, as mentioned previously, the absolute ground state is characterized by a notably smaller rate coefficient than the other rotational states at low energies, therefore small changes in the ground state population can enact considerable shifts of the theory curve.

5.1.5 Plasma rate coefficient

Dense and diffuse interstellar environments that represent most of the vast ISM can be approximated as a plasma, where the movement of particles that make up the gas follow a Maxwell–Boltzmann distribution, governed by a certain kinetic (plasma) temperature T_{pl}. The reaction rates are characterized by a corresponding kinetic temperature (plasma) rate. However, the diffuse interstellar medium facilitates conditions where molecular ions can radiatively cool down to their absolute ground rotational states in equilibrium with microwave background radiation of $\approx 2.7\,K$, which in principle can sometimes result in lower average ion ensemble temperatures T_{ion} than that of the average plasma temperature T_{pl}. Therefore, the conditions where $T_{ion} = T_{pl}$ are only valid at a local thermodynamic equilibrium, where collisional excitation events occur more often than the timescales required for radiative relaxation. Such a condition is satisfied in environments characterized by a sufficient critical density of $n_{critical} \approx 10^4\,cm^{-3}$. As many astrophysically relevant regions populated by triatomic hydrogen are associated by a lower particle density than $n_{critical}$, precise modelling of the reaction networks necessitates reliable reaction rates at a variety of plasma temperatures. The following paragraph outlines the derived plasma rates that were obtained from the long ion storage time MBRC data, where only a few rotational states are populated. Additionally, a comparison to previous results is provided.

The transformation from MBRC to plasma rate coefficients α_{pl} is governed by equation 4.42 and is calculated for the temperature range 10–4000 K. The choice of the kinetic temperature range is determined by its relevance in the context of astrophysical conditions, while also constricted in the low temperature part by the measured MBRC rates in terms of experimental resolution. The present results for both investigated molecular systems are compared with the most recent theoretical plasma rate coefficients used in chemical modelling from (Pagani, L.

et al. 2009).

Figure 5.14 depicts said comparison, with the ortho and para species of theory curves displayed separately. The experimental plasma rates obtained from the present work are characterized by a combined uncertainty (grey bar), which is dominated by the systematic uncertainty of $\approx 22\,\%$ on average, while the statistical uncertainty is not visible on a double logarithmic plot. As mentioned before, both experimentally investigated systems still retain some rotational excitation even after $1000\,s$ of storage time, the influence of which is encompassed in the presented convolved plasma rates. The remaining rotational excitation is not relevant for the plasma rate coefficient at high temperatures, but might result in a slightly increased rate below $100\,K$. However, this contribution is expected to be minor, as the majority of population is already located in the ground states of their respective ortho-para manifolds at storage times exceeding $1000\,s$.

The plasma rate coefficient of both ions is in fair agreement with respect to previous theory results throughout most of the plasma temperature range, while only meaningfully deviating below $\approx 90\,K$ and $60\,K$ for H_2D^+ and D_2H^+, respectively, with the largest observable discrepancy reaching up to a factor of ≈ 5. This disagreement is of particular importance, because the enhanced reaction rate suggests changes in abundances of H_2D^+ and D_2H^+ ions when modelling certain interstellar conditions, such as molecular clouds. The degree of significance on the astrophysical implications is yet to be explored and requires further investigation employing large astrochemical models.

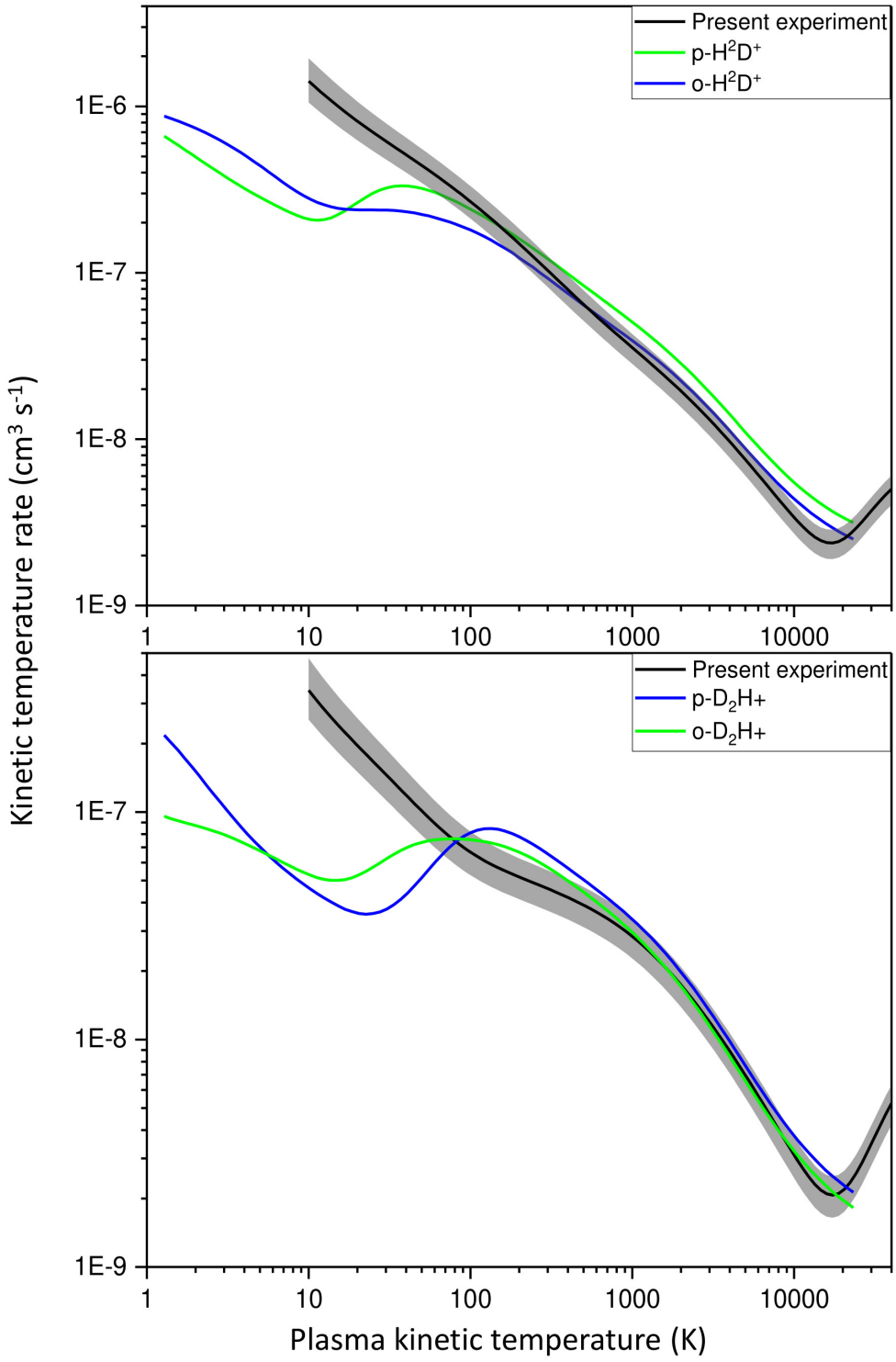

Figure 5.14: Dissociative recombination kinetic temperature rate (plasma rate) comparison to previous theoretical results. The present experimental data correspond to MBRC measured after long storage times (1000 s) for two electron beam settings. The theory data were extracted from (Pagani, L. et al. 2009).

Chapter 6

Outlook

6.1 Summary of results and future prospects

The experimental results described in the previous chapter signify the progress achieved in understanding the DR process of triatomic hydrogen ions. High-resolution, absolute merged–beams rate coefficients of DR were presented, accompanied by plasma rate coefficients. Comparisons to previous experimental efforts and to state-of-the-of-the-art theoretical calculations were discussed. It is evident that the present experimental results represent a large step forwards to the ultimate goal of DR measurements of triatomic hydrogen cations on the basis of individually populated quantum states.

The H_2D^+ ions employed in present measurements at long ion beam storage times represent a molecular ensemble that consists of only three significantly populated rotational states. Such state definition has been unprecedented in previous DR measurement attempts. Additionally, in terms of pure radiative relaxation, there is little to no room left for improvement from the experimental point of view, as the only excited rotational state features a lifetime that exceeds 8000 seconds. Any further relevant change of the population distribution must come from external manipulation. This may be achieved by utilizing a para hydrogen enriched gas sample for the production of the ions. As production of H_2D^+ ions in an ion source is a collisionally driven process, the imprint of the para–enriched hydrogen should be transferred to the produced para H_2D^+. This in turn, would change the fraction of the stored ions towards an increased population in para states and should lead to potentially observable changes in the measured merged–beams

rate, unravelling the question of the ortho–para nuclear spin state contribution to the measured DR rate.

Another approach for manipulation of the internal state composition lies within depletion by electron recombination. In principle, states that feature higher DR cross sections are depleted from the population distribution at an increased rate. As theoretical calculations predict significant discrepancy among the lowest rotational state DR cross–sections, state–selective depletion by electron recombination might be a viable option to further refine the quality of internal state definition under certain conditions. The problem with this approach is that it also depletes the entire ion beam, leading to shorter beam lifetimes and reduced statistics of the observed DR events of interest. Additionally, it is only advantageous to explore such a strategy if the DR rate differences are sufficiently large among individual rotational states. This method was briefly investigated throughout the beamtime, but as cardinal changes in the DR spectra were not observed and the experimental time was limited, further investigations were not prioritized.

The same aforementioned approaches could be valid for improving the internal state definition of the D_2H^+ molecular ensemble, where further reduction of the populated states seems more feasible. As demonstrated by the long storage time ($10000\,s$) simulation results in figure 3.8, an additional $1000\,s$ of beam storage time would reduce the number of significantly populated states from $\approx$ seven to three. This in turn would be beneficial to the analysis of the individual state contributions towards the observed DR rate.

As alluded to before in previous chapters, there remain unanswered questions regarding the obtained data. In principle, the NICE detector has recorded imaging data that allows for identification among the two and three body dissociation events. Therefore, the two–to–three body ratio as a function of detuning energy can be extracted from the measured data. As this information was not considered novel and does not retract from the presented results, it was left for future analysis.

Furthermore, there are no obvious dominant features of the measured merged–beams rate spectra that would correlate to one particular rotational state. Therefore, the current analysis has omitted the ongoing efforts to correlate the change in the observed merged–beams rate to changes in population distribution. However, given the internal state definition in the present experiment this is seems as a tractable problem for the near future.

The present results include a comparison of the convolved plasma rates with estimates from previous work. The impact of the acquired results in the context of interstellar cloud chemistry calculations is currently under evaluation. Initial discussion suggests that the results of the present work will slightly influence the

fractional abundances of molecules originating from ion–neutral reactions.

In order to expand the current experiment to the non–deuterated species of triatomic hydron cations and address the DR process on a state–specific basis requires further developments. The principle issue being meta stable rotational excitations that do not decay on practical time scales. This problem can be circumvented by already starting the DR experiment with a cold molecular ensemble. To that end the design, commissioning and characterization of a new expansion–type ion source was initiated. The first implementation of this ion source in a CSR experiment is occurring in the present Autumn/Spring measurement campaign of 2023/2024. Additionally, developments of a laser diagnostics scheme, that would address the individually populated rotational states is underway, with the theoretical concept laid out in (Znotins et al. 2021).

Bibliography

Bates, D. R. (1950). 'Dissociative Recombination.' In: *Physical Review* 78 (4), pp. 492–493. DOI: 10.1103/PhysRev.78.492.

Baumann, P. et al. (1988). 'The Heidelberg Heavy Ion Test Storage Ring TSR.' In: *Nuclear Instruments and Methods in Physics Research A* 268 (2-3), pp. 531–537. DOI: 10.1016/0168-9002(88)90573-6.

Becker, A. (2016). 'Imaging of Neutral Fragmentation Products from Fast Molecular Ion Beams: Paving the Way for Reaction Studies in Cryogenic Environment.' PhD thesis. Ruprecht-Karls-Universität Heidelberg. DOI: 10.11588/heidok.00020213.

Biondi, M. A. and S. C. Brown (1949). 'Measurements of Ambipolar Diffusion in Helium.' In: *Phys. Rev.* 75 (11), pp. 1700–1705. DOI: 10.1103/PhysRev.75.1700.

Black, J. H. (2000). 'The abundance and excitation of interstellar H_3^+.' In: *Philosophical Transactions of the Royal Society of London. Series A: Mathematical, Physical and Engineering Sciences* 358 (1774), pp. 2515–2521. DOI: https://doi.org/10.1098/rsta.2000.0664.

Bohr, N. (1919). 'On the model of a triatomic hydrogen molecule.' In: *Meddelanden fran K. Vetenskapsakademiens Nobelinstitut* 5 (28), p. 16.

Boikova, R. F. and V. D. Ob'edkov (1968). 'Rotational and vibrational excitation of molecular ions by electrons.' In: *Soviet Physics Journal of Experimental and Theoretical Physics* 27 (5), pp. 772–774.

Bowesman, C. A., I. I. Mizus, N. F. Zobov, O. L. Polyansky, J. Sarka, B. Poirier, M. Pezzella, S. N. Yurchenko, and J. Tennyson (2023). 'ExoMol line lists – L: high-resolution line lists of H_3^+, H_2D^+, D_2H^+, and D_3^+.' In: *Monthly Notices of the Royal Astronomical Society* 519 (4), pp. 6333–6348. DOI: 10.1093/mnras/stad050. eprint: https://academic.oup.com/mnras/article-pdf/519/4/6333/48946739/stad050.pdf.

Brünken, S., O. Sipilä, E. T. Chambers, J. Harju, P. Caselli, O. Asvany, C. E. Honingh, T. Kamiński, K. M. Menten, J. Stutzki, et al. (2014). 'H2D+ observations give an age of at least one million years for a cloud core forming Sun-like stars.' In: *Nature* 516 (7530), pp. 219–221.

Budker, G. I. (1967). 'An effective method of damping particle oscillations in proton and antiproton storage rings.' In: *Soviet Atomic Energy* 22, pp. 438–440. DOI: 10.1007/BF01175204.

Budker, G. I., N. S. Dikanskij, D. V. Pestrikov, I. N. Meshkov, V. I. Kudelainen, B. N. Sukhina, V. V. Parkhomchuk, and A. N. Skrinsky (1976). 'Experimental studies of electron cooling.' In: *Particle Accelerators* 7, pp. 197–211.

Carney, G. D. and R. N. Porter (1974). 'H_3^+: Geometry dependence of electronic properties.' In: *The Journal of Chemical Physics* 60 (11), pp. 4251–4264. DOI: 10.1063/1.1680896. eprint: https://pubs.aip.org/aip/jcp/article-pdf/60/11/4251/13871635/4251_1_online.pdf.

Carney, G. D. and R. N. Porter (1976). 'H_3^+: Ab initio calculation of the vibration spectrum.' In: *The Journal of Chemical Physics* 65 (9), pp. 3547–3565. DOI: 10.1063/1.433585. eprint: https://pubs.aip.org/aip/jcp/article-pdf/65/9/3547/13787896/3547_1_online.pdf.

Carney, G. D. and R. N. Porter (1980). 'Ab Initio Prediction of the Rotation-Vibration Spectrum of H_3^+ and D_3^+.' In: *Phys. Rev. Lett.* 45 (7), pp. 537–541. DOI: 10.1103/PhysRevLett.45.537.

Chang, E. S. and U. Fano (1972). 'Theory of Electron-Molecule Collisions by Frame Transformations.' In: *Phys. Rev. A* 6 (1), pp. 173–185. DOI: 10.1103/PhysRevA.6.173.

Christoffersen, R. E., S. Hagstrom, and F. Prosser (1964). 'H_3^+ Molecule Ion. Its Structure and Energy.' In: *The Journal of Chemical Physics* 40 (1), pp. 236–237. DOI: 10.1063/1.1724870. eprint: https://pubs.aip.org/aip/jcp/article-pdf/40/1/236/11034726/236_1_online.pdf.

Chu, S.-I. (1975). 'Rotational excitation of symmetric-top molecular ions by electron impact.' In: *Phys. Rev. A* 12 (2), pp. 396–405. DOI: 10.1103/PhysRevA.12.396.

Corney, A. (2006). *Atomic and Laser Spectroscopy*. Oxford University Press. DOI: 10.1093/acprof:oso/9780199211456.003.0005.

Coulson, C. A. (1935). 'The Electronic Structure of H_3^+.' In: *Mathematical Proceedings of the Cambridge Philosophical Society* 31 (2), pp. 244–259. DOI: 10.1017/S0305004100013347.

Dalgarno, A., E. Herbst, S. Novick, and W. Klemperer (1973). 'Radio Spectrum of H_2D^+.' In: *Astrophysical Journal* 183, p. L131. DOI: 10.1086/181270.

Datz, S., M. Larsson, C. Stromholm, G. Sundström, V. Zengin, H. Danared, A. Källberg, and M. a. Ugglas (1995). 'Dissociative recombination of H_2D^+: Cross sections, branching fractions, and isotope effects.' In: *Phys. Rev. A* 52 (4), pp. 2901–2909. DOI: 10.1103/PhysRevA.52.2901.

Drossart, P. et al. (1989). 'Detection of H_3^+ on Jupiter.' In: *Nature* 340, pp. 539–541. DOI: 10.1038/340539a0..

Faure, A. and J. Tennyson (2002). 'Electron-impact rotational excitation of symmetric-top molecular ions.' In: *Journal of Physics B: Atomic, Molecular and Optical Physics* 35 (18), p. 3945. DOI: 10.1088/0953-4075/35/18/312.

Faure, A. and J. Tennyson (2001). 'Electron-impact rotational excitation of linear molecular ions.' In: *Monthly Notices of the Royal Astronomical Society* 325 (1), pp. 443–448. DOI: 10.1046/j.1365-8711.2001.04480.x.

Faure, A. and J. Tennyson (2003). 'Rate coefficients for electron-impact rotational excitation of H_3^+ and H_3O^+.' In: *Monthly Notices of the Royal Astronomical Society* 340 (2), pp. 468–472. DOI: 10.1046/j.1365-8711.2003.06306.x.

Faure, A. and J. Tennyson (2023). *Private communication.*

Florescu-Mitchell, A. I. and J. B. A. Mitchell (2006). 'Dissociative recombination.' In: *Physics Reports* 430 (5), pp. 277–374. DOI: 10.1016/j.physrep.2006.04.002.

Forck, P., M. Grieser, D. Habs, A. Lampert, R. Repnow, D. Schwalm, A. Wolf, and D. Zajfman (1993). 'Dissociative recombination of cold HD^+ at the Test Storage Ring.' In: *Phys. Rev. Lett.* 70 (4), pp. 426–429. DOI: 10.1103/PhysRevLett.70.426.

Furtenbacher, T. and A. G. Császár (2012). 'MARVEL: Measured active rotational–vibrational energy levels. II. Algorithmic improvements.' In: *Journal of Quantitative Spectroscopy and Radiative Transfer* 113 (11), pp. 929–935. DOI: https://doi.org/10.1016/j.jqsrt.2012.01.005.

Furtenbacher, T., A. G. Császár, and J. Tennyson (2007). 'MARVEL: measured active rotational–vibrational energy levels.' In: *Journal of Molecular Spectroscopy* 245 (2), pp. 115–125. DOI: https://doi.org/10.1016/j.jms.2007.07.005.

Furtenbacher, T., T. Szidarovszky, E. Mátyus, C. Fábri, and A. G. Császár (2013). 'Analysis of the Rotational–Vibrational States of the Molecular Ion H_3^+.' In: *Journal of Chemical Theory and Computation* 9 (12), pp. 5471–5478. DOI: 10.1021/ct4004355.

Gaillard, M. J., D. S. Gemmell, G. Goldring, I. Levine, W. J. Pietsch, J. C. Poizat, A. J. Ratkowski, J. Remillieux, Z. Vager, and B. J. Zabransky (1978). 'Experimental determination of the structure of H_3^+.' In: *Phys. Rev. A* 17 (6), pp. 1797–1803. DOI: 10.1103/PhysRevA.17.1797.

Geballe, T. R., M. .-F. Jagod, and T. Oka (1993). 'Detection of H_3^+ Infrared Emission Lines in Saturn.' In: *Astrophysical Journal* 408, p. L109. DOI: 10.1086/186843.

Geballe, T. R. and T. Oka (1996). 'Detection of H_3^+ in interstellar space.' In: *Nature* 384 (6607), pp. 334–335. DOI: 10.1038/384334a0.

Gerlich, D., E. Herbst, and E. Roueff (2002). '$H_3^+ + HD \leftrightarrow H_2D^+ + H_2$: low-temperature laboratory measurements and interstellar implications.' In: *Planetary and Space Science* 50 (12), pp. 1275–1285. DOI: https://doi.org/10.1016/S0032-0633(02)00094-6.

Giusti, A. (1980). 'A multichannel quantum defect approach to dissociative recombination.' In: *Journal of Physics B: Atomic and Molecular Physics* 13 (19), p. 3867. DOI: 10.1088/0022-3700/13/19/025.

Giusti-Suzor, A., J. N. Bardsley, and C. Derkits (1983). 'Dissociative recombination in low-energy e-H_2^+ collisions.' In: *Physical Review A* 28 (2), pp. 682–691. DOI: 10.1103/PhysRevA.28.682.

Grieser, M. et al. (2022). 'Isochronous mass spectrometry in an electrostatic storage ring.' In: *Review of Scientific Instruments* 93 (6), p. 063302. DOI: 10.1063/5.0090131.

Grussie, F. (2016). 'Experimental studies of ion-neutral reactions under astrophysical conditions.' PhD thesis. Ruprecht-Karls-Universität Heidelberg. DOI: 10.11588/heidok.00021435.

Hamilton, J. R., A. Faure, and J. Tennyson (2015). 'Electron-impact excitation of diatomic hydride cations – I. HeH^+, CH^+, ArH^+.' In: *Monthly Notices of the Royal Astronomical Society* 455 (3), pp. 3281–3287. DOI: 10.1093/mnras/stv2429.

Herbst, E. (2000). 'The astrochemistry of H_3^+.' In: *Philosophical Transactions of the Royal Society of London. Series A: Mathematical, Physical and Engineering Sciences* 358 (1774), pp. 2523–2534. DOI: https://doi.org/10.1098/rsta.2000.0665.

Herbst, E. and W. Klemperer (1973). 'The Formation and Depletion of Molecules in Dense Interstellar Clouds.' In: *Astrophysical Journal* 185, pp. 505–534. DOI: 10.1086/152436.

Hindmarsh, A. C. (1983). 'ODEPACK, A Systematized Collection of ODE Solvers.' In: IMACS Transactions on Scientific Computation.

Hindmarsh, A. C. (2019). *ODEPACK: Ordinary differential equation solver library*. Astrophysics Source Code Library, record ascl:1905.021.

Inui, T., Y. Tanabe, and Y. Onodera (2012). *Group theory and its applications in physics*. Springer Science & Business Media.

Kálosi, Á. et al. (2021). 'Dissociative Recombination of Internally OH^+ Molecules with Electrons.' In: American Astronomical Society Meeting Abstracts 53, p. 112.03.

Kálosi, Á. et al. (2022). 'Laser Probing of the Rotational Cooling of Molecular Ions by Electron Collisions.' In: *Phys. Rev. Lett.* 128 (18), p. 183402. DOI: 10.1103/PhysRevLett.128.183402.

Kokoouline, V. and C. H. Greene (2003). 'Unified theoretical treatment of dissociative recombination of D_{3h} triatomic ions: Application to H_3^+ and D_3^+.' In: *Phys. Rev. A* 68 (1), p. 012703. DOI: 10.1103/PhysRevA.68.012703.

Kokoouline, V. and C. H. Greene (2004). 'Triatomic dissociative recombination theory: Jahn–Teller coupling among infinitely many Born–Oppenheimer surfaces.' In: *Faraday Discussions* 127, pp. 413–423. DOI: 10.1039/B314659F.

Kokoouline, V. and C. H. Greene (2005a). 'Theoretical study of dissociative recombination of C_{2v} triatomic ions: Application to H_2D^+ and D_2H^+.' In: *Phys. Rev. A* 72 (2), p. 022712. DOI: 10.1103/PhysRevA.72.022712.

Kokoouline, V. and C. H. Greene (2005b). 'Theoretical study of dissociative recombination of C_{2v} triatomic ions: Application to H_2D^+ and D_2H^+.' In: *Phys. Rev. A* 72 (2), p. 022712. DOI: 10.1103/PhysRevA.72.022712.

Kokoouline, V. and C. H. Greene (2023). *Private communication.*

Kozin, I., R. Roberts, and J. Tennyson (2000). 'Relative equilibria of D_2H^+ and H_2D^+.' In: *Molecular physics* 98 (5), pp. 295–307.

Krantz, C. (2009). 'Intense Electron Beams from GaAs Photocathodes as a Tool for Molecular and Atomic Physics.' PhD thesis. Ruprecht-Karls-Universität Heidelberg. DOI: 10.11588/heidok.00010009.

Kreckel, H., J. Tennyson, D. Schwalm, D. Zajfman, and A. Wolf (2004). 'Rovibrational relaxation model for H_3^+.' In: *New Journal of Physics* 6 (1), p. 151. DOI: 10.1088/1367-2630/6/1/151.

Kreckel, H. et al. (2002). 'Vibrational and rotational cooling of H_3^+.' In: *Phys. Rev. A* 66 (5), p. 052509. DOI: 10.1103/PhysRevA.66.052509.

Kreckel, H. et al. (2005). 'High-Resolution Dissociative Recombination of Cold $H_3{}^+$ and First Evidence for Nuclear Spin Effects.' In: *Phys. Rev. Lett.* 95 (26), p. 263201. DOI: 10.1103/PhysRevLett.95.263201.

Kreckel, H., D. Bing, S. Reinhardt, A. Petrignani, M. Berg, and A. Wolf (2008). 'Chemical probing spectroscopy of H_3^+ above the barrier to linearity.' In: *Journal of Chemical Physics* 129 (16). DOI: 10.1063/1.2994730.

Kreckel, H. et al. (2010). 'High-resolution storage-ring measurements of the dissociative recombination of H_3^+ using a supersonic expansion ion source.' In: *Phys. Rev. A* 82 (4), p. 042715. DOI: 10.1103/PhysRevA.82.042715.

Lammich, L. et al. (2005). 'DR rate coefficient measurements using stored beams of H_3^+ and its isotopomers.' In: *Journal of Physics: Conference Series* 4 (1), p. 98. DOI: 10.1088/1742-6596/4/1/013.

Lammich, L. et al. (2003). 'Evidence for Subthermal Rotational Populations in Stored Molecular Ions through State-Dependent Dissociative Recombination.' In: *Phys. Rev. Lett.* 91 (14), p. 143201. DOI: 10.1103/PhysRevLett.91.143201.

Larsson, M. (2005). 'Molecular ion recombination in merged beams: experimental results on small systems and future perspectives.' In: *Journal of Physics: Conference Series* 4 (007), pp. 50–57.

Larsson, M. et al. (1993). 'Direct high-energy neutral-channel dissociative recombination of cold H_3^+ in an ion storage ring.' In: *Phys. Rev. Lett.* 70 (4), pp. 430–433. DOI: 10.1103/PhysRevLett.70.430.

Laux, F. (2011). 'Entwicklung von kapazitiven Positions-, Strom- und Schottkysignal-Messsystemen für den kryogenen Speicherring CSR.' PhD thesis. University of Heidelberg. DOI: 10.11588/heidok.00012435.

Light, J. C. and T. Carrington Jr. (2000). *Advances in Chemical Physics*. John Wiley & Sons, Ltd.

Linstrom, P. and W. Mallard (2023). *NIST Chemistry WebBook, NIST Standard Reference Database Number 69*. National Institute of Standards and Technology, Gaithersburg MD, 20899. DOI: https://doi.org/10.18434/T4D303.

Lique, F. and A. Faure (2019). *Gas-Phase Chemistry in Space*. IOP Publishing. DOI: 10.1088/2514-3433/aae1b5.

Martin, D. W., E. W. McDaniel, and M. L. Meeks (1961). 'On the Possible Occurence of H_3^+ in Interstellar Space.' In: *Astrophysical Journal* 134, pp. 1012–1013. DOI: 10.1086/147232.

McCall, B. J., T. R. Geballe, K. H. Hinkle, and T. Oka (1998). 'Detection of H_3^+ in the Diffuse Interstellar Medium Toward Cygnus OB2 No. 12.' In: *Science* 279 (5358), pp. 1910–1913. DOI: 10.1126/science.279.5358.1910.

McCall, B. J. et al. (2004). 'Dissociative recombination of rotationally cold H_3^+.' In: *Phys. Rev. A* 70 (5), p. 052716. DOI: 10.1103/PhysRevA.70.052716.

McCall, B. J. (2001). 'Spectroscopy of H_3^+ in Laboratory and Astrophysical Plasmas.' PhD thesis. The University of Chicago.

Meyer, C. et al. (2017). 'Radiative Rotational Lifetimes and State-Resolved Relative Detachment Cross Sections from Photodetachment Thermometry of Molecular Anions in a Cryogenic Storage Ring.' In: *Phys. Rev. Lett.* 119 (2), p. 023202. DOI: 10.1103/PhysRevLett.119.023202.

Meyer, W., P. Botschwina, and P. Burton (1986). '*Abinitio* calculation of near-equilibrium potential and multipole moment surfaces and vibrational frequen-

cies of H_3^+ and its isotopomers.' In: *The Journal of Chemical Physics* 84 (2), pp. 891–900. DOI: 10.1063/1.450534.

Millar, T., A. Bennett, and E. Herbst (1989). 'Deuterium fractionation in dense interstellar clouds.' In: *Astrophysical Journal* 340, pp. 906–920.

Miller, S., J. Tennyson, T. R. Geballe, and T. Stallard (2020). 'Thirty years of H_3^+ astronomy.' In: *Rev. Mod. Phys.* 92 (3), p. 035003. DOI: 10.1103/RevModPhys.92.035003.

Mizus, I. I., A. Alijah, N. F. Zobov, L. Lodi, A. A. Kyuberis, S. N. Yurchenko, J. Tennyson, and O. L. Polyansky (2017). 'ExoMol molecular line lists – XX. A comprehensive line list for H_3^+.' In: *Monthly Notices of the Royal Astronomical Society* 468 (2), pp. 1717–1725. DOI: 10.1093/mnras/stx502.

Nakano, Y., Y. Enomoto, T. Masunaga, S. Menk, P. Bertier, and T. Azuma (2017). 'Design and commissioning of the RIKEN cryogenic electrostatic ring (RICE).' In: *Review of Scientific Instruments* 88 (3). DOI: 10.1063/1.4978454.

Neale, L., S. Miller, and J. Tennyson (1996). 'Spectroscopic Properties of the H_3^+ Molecule: A New Calculated Line List.' In: *Astrophysical Journal* 464, p. 516. DOI: 10.1086/177341.

Neufeld, D. A. and A. Dalgarno (1989). 'Electron-impact excitation of molecular ions.' In: *Phys. Rev. A* 40 (2), pp. 633–637. DOI: 10.1103/PhysRevA.40.633.

Novotný, O. et al. (2013). 'Dissociative Recombination Measurements of HCl^+ using an Ion Storage Ring.' In: *The Astrophysical Journal* 777 (1), p. 54. DOI: 10.1088/0004-637x/777/1/54.

Novotný, O. et al. (2019). 'Quantum-state–selective electron recombination studies suggest enhanced abundance of primordial HeH^+.' In: *Science* 365 (6454), pp. 676–679. DOI: 10.1126/science.aax5921.

Oka, T. (1980). 'Observation of the Infrared Spectrum of H_3^+.' In: *Phys. Rev. Lett.* 45 (7), pp. 531–534. DOI: 10.1103/PhysRevLett.45.531.

Oka, T., T. R. Geballe, M. Goto, T. Usuda, Benjamin, J. McCall, and N. Indriolo (2019). 'The Central 300 pc of the Galaxy Probed by Infrared Spectra of H_3^+ and CO. I. Predominance of Warm and Diffuse Gas and High H_2 Ionization Rate.' In: *Astrophysical Journal* 883 (1), p. 54. DOI: 10.3847/1538-4357/ab3647.

Orel, A., I. Schneider, and A. Suzor-Weiner (2000). 'Dissociative recombination of H_3^+: progress in theory.' In: *Philosophical Transactions of the Royal Society of London. Series A: Mathematical, Physical and Engineering Sciences* 358 (1774), pp. 2445–2456. DOI: https://doi.org/10.1098/rsta.2000.0659.

Orlov, D. A., F. Sprenger, M. Lestinsky, U. Weigel, A. S. Terekhov, D. Schwalm, and A. Wolf (2005). 'Photocathodes as electron sources for high resolution merged beam experiments.' In: *Journal of Physics: Conference Series* 4 (1), p. 290. DOI: 10.1088/1742-6596/4/1/045.

Pagani, L., Vastel, C., Hugo, E., Kokoouline, V., Greene, C. H., Bacmann, A., Bayet, E., Ceccarelli, C., Peng, R., and Schlemmer, S. (2009). 'Chemical modeling of L183 (L134N): an estimate of the ortho/para H${_2}$ ratio*.' In: *A&A* 494 (2), pp. 623–636. DOI: 10.1051/0004-6361:200810587.

Pastuszka, S., M. Hoppe, D. Kratzmann, D. Schwalm, A. Wolf, A. S. Jaroshevich, S. N. Kosolobov, D. A. Orlov, and A. S. Terekhov (2000). 'Preparation and performance of transmission-mode GaAs photocathodes as sources for cold dc electron beams.' In: *Journal of Applied Physics* 88 (11), pp. 6788–6800. DOI: 10.1063/1.1311307.

Pastuszka, S. et al. (1996). 'Electron cooling and recombination experiments with an adiabatically expanded electron beam.' In: *Nuclear Instruments and Methods in Physics Research Section A: Accelerators, Spectrometers, Detectors and Associated Equipment* 369 (1), pp. 11–22. DOI: 10.1016/0168-9002(95)00786-5.

Paul, D. (2021). 'Electron recombination studies of rotationally CH^+ cold ions at the Cryogenic Storage Ring.' PhD thesis. Ruprecht-Karls-Universität Heidelberg. DOI: 10.11588/heidok.00030307.

Petrignani, A. et al. (2011). 'Resonant structure of low-energy H_3^+ dissociative recombination.' In: *Phys. Rev. A* 83 (3), p. 032711. DOI: 10.1103/PhysRevA.83.032711.

Polyansky, O. L., B. M. Dinelli, C. R. Le Sueur, and J. Tennyson (1995). 'Asymmetric adiabatic correction to the rotation-vibration levels of H_2D^+ and D_2H^+.' In: *The Journal of chemical physics* 102 (23), pp. 9322–9326. DOI: https://doi.org/10.1063/1.468799.

Ross, S. (1991). 'An MQDT Primer.' In: *AIP Conference Proceedings* 225 (1), pp. 73–110. DOI: 10.1063/1.40550.

Saurabh, S. (2019). 'Collision studies with internally cold ion beams and merged electron beams in a cryogenic storage ring.' PhD thesis. Ruprecht-Karls-Universität Heidelberg. DOI: 10.11588/heidok.00026791.

Schippers, S., M. Schnell, C. Brandau, S. Kieslich, A. Müller, and A. Wolf (2004). 'Experimental Mg IX photorecombination rate coefficient.' In: *A&A* 421 (3), pp. 1185–1191. DOI: 10.1051/0004-6361:20040380.

Shornikov, A. (2012). 'An electron cooler for ultra-low energy cryogenic operation.' PhD thesis. Ruprecht-Karls-Universität Heidelberg. DOI: 10.11588/heidok.00013459.

Spicer, W. E. (1977). 'Negative affinity 3-5 photocathodes: Their physics and technology.' In: *Applied physics* 12 (2), pp. 115–130. DOI: https://doi.org/10.1007/BF00896137.

Sprecher, D., J. Liu, C. Jungen, W. Ubachs, and F. Merkt (2010). 'Communication: The ionization and dissociation energies of HD.' In: *The Journal of Chemical Physics* 133 (11), p. 111102. DOI: 10.1063/1.3483462.

Sprenger, F., M. Lestinsky, D. Orlov, D. Schwalm, and A. Wolf (2004). 'The high-resolution electron–ion collision facility at TSR.' In: *Nuclear Instruments and Methods in Physics Research Section A: Accelerators, Spectrometers, Detectors and Associated Equipment* 532 (1), pp. 298–302. DOI: https://doi.org/10.1016/j.nima.2004.06.058.

Spruck, K. et al. (2015). 'An efficient, movable single-particle detector for use in cryogenic ultra-high vacuum environments.' In: *Review of Scientific Instruments* 86 (2), p. 023303. DOI: 10.1063/1.4907352.

Strasser, D., L. Lammich, H. Kreckel, M. Lange, S. Krohn, D. Schwalm, A. Wolf, and D. Zajfman (2004). 'Breakup dynamics and isotope effects in D_2H^+ and H_2D^+ dissociative recombination.' In: *Phys. Rev. A* 69 (6), p. 064702. DOI: 10.1103/PhysRevA.69.064702.

Szalay, V. and L. Nemes (1994). 'The discrete variable representation of the rotational-vibrational Hamiltonian of triatomic molecules.' In: *Chemical Physics Letters* 231 (2), pp. 225–234. DOI: https://doi.org/10.1016/0009-2614(94)01229-6.

Tecker, F. (2020). 'Longitudinal Beam Dynamics in Circular Accelerators.' In: *arXiv preprint arXiv:2011.02932*.

Tennyson, J., M. A. Kostin, P. Barletta, G. J. Harris, O. L. Polyansky, J. Ramanlal, and N. F. Zobov (2004). 'DVR3D: a program suite for the calculation of rotation–vibration spectra of triatomic molecules.' In: *Computer Physics Communications* 163 (2), pp. 85–116. DOI: https://doi.org/10.1016/j.cpc.2003.10.003.

Tennyson, J. and S. N. Yurchenko (2012). 'ExoMol: molecular line lists for exoplanet and other atmospheres.' In: *Monthly Notices of the Royal Astronomical Society* 425 (1), pp. 21–33. DOI: 10.1111/j.1365-2966.2012.21440.x. eprint: https://academic.oup.com/mnras/article-pdf/425/1/21/3182616/425-1-21.pdf.

Thomas, R. D. et al. (2011). 'The double electrostatic ion ring experiment: A unique cryogenic electrostatic storage ring for merged ion-beams studies.' In: *Review of Scientific Instruments* 82 (6). DOI: 10.1063/1.3602928.

Thomson, J. J. (1911). 'XXVI. Rays of positive electricity.' In: *The London, Edinburgh, and Dublin Philosophical Magazine and Journal of Science* 21 (122),

pp. 225–249. DOI: 10.1080/14786440208637024. eprint: https://doi.org/10.1080/14786440208637024.

Trafton, L. M., T. R. Geballe, S. Miller, J. Tennyson, and G. E. Ballester (1993). 'Detection of H_3^+ from Uranus.' In: *Astrophysical Journal* 405, p. 761. DOI: 10.1086/172404.

Urbain, X., A. Dochain, R. Marion, T. Launoy, and J. Loreau (2019). 'Photodissociation as a probe of the H_3^+ avoided crossing seam.' In: *Philosophical Transactions of the Royal Society A* 377 (2154), p. 20180399.

Vastel, C., T. G. Phillips, and H. Yoshida (2004). 'Detection of D2H+ in the Dense Interstellar Medium.' In: *The Astrophysical Journal* 606 (2), p. L127. DOI: 10.1086/421265.

Virtanen, P. et al. (2020). 'SciPy 1.0: Fundamental Algorithms for Scientific Computing in Python.' In: *Nature Methods* 17, pp. 261–272. DOI: 10.1038/s41592-019-0686-2.

Vogel, S. (2016). 'Developments at an Electrostatic Cryogenic Storage Ring for Electron-Cooled keV Energy Ion Beams.' PhD thesis. Ruprecht-Karls-Universität Heidelberg. DOI: 10.11588/heidok.00020262.

von Hahn, R. et al. (2016). 'The cryogenic storage ring CSR.' In: *Review of Scientific Instruments* 87 (6), p. 063115. DOI: 10.1063/1.4953888.

Watson, W. D. (1973). 'The rate of formation of interstellar molecules by ion-molecule reactions.' In: *Astrophysical Journal, vol. 183, p. L17* 183, p. L17.

Weigel, U. (2003). 'Cold Intense Electron Beams from Gallium Arsenide Photocathodes.' PhD thesis. Ruprecht-Karls-Universität Heidelberg. DOI: 10.11588/heidok.00004513.

Wiedemann, H. (2015). *Particle Accelerator Physics*. 4th ed. Springer Nature. DOI: 10.1007/978-3-319-18317-6.

Wilhelm, P. U. (2019). 'First Studies of Low-Energy Electron Cooling of keV Energy Ion Beams at the Electrostatic Cryogenic Storage Ring CSR.' PhD thesis. Ruprecht-Karls-Universität Heidelberg. DOI: 10.11588/heidok.00026821.

Zhaunerchyk, V., R. D. Thomas, W. D. Geppert, M. Hamberg, M. Kaminska, E. Vigren, and M. Larsson (2008). 'Dissociative recombination of D_2H^+: Comparison between recent storage-ring results and theoretical calculations.' In: *Phys. Rev. A* 77 (3), p. 034701. DOI: 10.1103/PhysRevA.77.034701.

Znotins, A., F. Grussie, A. Wolf, X. Urbain, and H. Kreckel (2021). 'An approach for multi-color action spectroscopy of highly excited states of H_3^+.' In: *Journal of Molecular Spectroscopy* 378, p. 111476. DOI: https://doi.org/10.1016/j.jms.2021.111476.

Acknowledgments

This work would not have been possible without the involvement of many others, who guided me throughout these past years. I express my gratitude to everyone who supported me scientifically and morally.
I would like to express my appreciation to my PhD supervisor Dr. Holger Kreckel for the immense patience and guidance during the experiment and writing phases of the doctoral thesis. His practical suggestions and helpful advice cannot be overestimated. The thesis reviews, discussions and general advice has been instrumental in the successful completion of this dissertation.
I extend my gratitude to Dr. Ábel Kálosi, Dr. Daniel Paul, Dr. Oldřich Novotný and Leonard Isberner for guiding me through the experimental and analysis part of this work. Without their expertise, this project would not have been possible.
I would like to acknowledge the contributions of Dr. Florian Grussie, Dr. Damian Müll and Felix Nüßlein from whom I have learned valuable experimental skills.
I express my gratitude to my other colleagues (Viviane, Lauren, Lukas, Selina, Jonas, Julia, Chris, Lisa, Bhalchandra) for creating the pleasant atmosphere at the institute and for all of the conversations.
I would like to thank the entire CSR team for the continuous support received throughout the course of the experimental work. I am grateful to Prof. Dr. Klaus Blaum for the possibility given to be a part of this team and for the opportunity to carry out my doctoral thesis work at the MPIK.
Special thanks to Ábel, Leonard, Damian and Daniel for the time spent together outside working hours. Thank you for all of the adventures and shenanigans that we have gone through throughout the years.
This dissertation would not have been possible without the help of my dear wife Marta. I express my sincerest gratitude for the unwavering support during the most difficult moments.